Summer 2009

Surface Dynamics of Silicon Low-Index Surfaces Studied by Reflection High-Energy Electron Diffraction

Ibrahim El-Kholy
Old Dominion University

SURFACE DYNAMICS OF Si LOW-INDEX SURFACES STUDIED BY REFLECTION HIGH-ENERGY ELECTRON DIFFRACTION

By

Ibrahim El-Kholy
M.S. May 1997, Cairo University
B.Sc. May 1990, Cairo University

A Dissertation Submitted to the Faculty of Old Dominion University in Partial Fulfillment of the Requirement for the Degree of

DOCTOR OF PHILOSOPHY

ELECTRICAL ENGINEERING

OLD DOMINION UNIVERSITY

August 2009

Approved by:

Hani E. Elsayed-Ali (Director)

Helmut Baumgart (Member)

Charles Sukenik (Member)

Gon Namkoong (Member)

ABSTRACT

SURFACE DYNAMICS OF Si LOW-INDEX SURFACES STUDIED BY REFLECTION HIGH-ENERGY ELECTRON DIFFRACTION

Ibrahim El-Kholy
Old Dominion University, 2009
Director: Dr. Hani Elsayed-Ali

Surface morphology during the growth of Si on Si(111)-(7x7) by femtosecond pulsed laser deposition (fsPLD) is studied using reflection high-energy electron diffraction (RHEED) at different temperatures. The growth of Si on Si(111) has received considerable attention as a model system of homoepitaxy. PLD is a deposition technique that uses much more energetic species (atoms and ions) compared to other physical vapor deposition (PVD), such as in molecular beam epitaxy. In this work, *in situ* reflection high energy electron diffraction (RHEED) was used to study the dynamics of PLD of Si on Si(111)-(7×7). Epitaxial growth of Si/Si(111)-(7x7) at temperatures as low as 210 °C was observed. For this substrate temperature, no change in RHEED patterns after growth, and only reduction in intensity during deposition was observed.

Surface Debye temperature of the topmost layer of the Si(111)-7x7 is measured by using RHEED. The diffraction intensity is distorted by the thermal vibration amplitude of atoms on the topmost layer of the surface.

Influence of Si deposition on the temperature of Si(111) to (7x7) phase transition is also studied. The phase transition showed that Si deposition lowers the transition temperature. A Ti-sapphire laser (100 fs, 800 nm, 1 kHz) was used to ablate a Si target on Si(111)-(1x1) during quenching from high temperature. The RHEED intensity was

observed as the substrate was exposed to the Si plume and the Si(111) substrate was quenched. The RHEED patterns showed a shift in the transition temperature from 840 °C without the plume to 820 °C with the plume.

With laser fluence below the damage threshold, laser enhanced epitaxial growth shows a great improvement in deposit Si on Si(111)-7x7 at low temperature (room temperature).

ACKNOWLEDGMENTS

I thank all the people who have helped or encouraged me, especially my advisor, Dr. Hani Elsayed-Ali, for his assistance, guidance and direction for this research. Also, I would like to thank Dr. Helmut Baumgart, Dr. Charles Sukenik, and Dr. Gon Namkoong for serving on my committee.

I would like also to thank Mahmoud Abdel-Fatah for helping me with the fs-laser. Thanks also goes to my friends Mohamed Hegazy, Ahmed Ragab and Dr. Ali's group for their help and encouragement.

This thesis is dedicated to

My mother!

الى الحبيبة أمي!

TABLE OF CONTENTS

LIST OF FIGURES

Figure **Page**

LIST OF TABLES

Table **Page**

CHAPTER I

INTRODUCTION

I.1. Introduction

Studying the structure of low index semiconductor materials has resulted in advances in surface science and semiconductor fabrication. Many techniques have been used to examine the surface on a microscopic scale. These techniques may use electrons either as the probe or as the detectable particle or both. Techniques such as the Auger Electron Spectroscopy (AES), Reflection High Energy Electron Diffraction (RHEED), Scanning Electron Microscope (SEM), and Transmission Electron Microscope (TEM) use electrons to form an image.[1-6] Recently, silicon homoepitaxy has received considerable attention both because of possible applications and the presumed simplicity of epitaxy in a monoatomic system.

In the homoepitaxial growth of a Si on Si(111)-7x7 reconstructed surface using the Pulsed Laser Deposition (PLD) technique, in comparison with other techniques such as the Molecular Beam Epitaxy (MBE), shows that PLD has excelled in depositing high quality thin film at low temperatures. Development of the homoepitaxial growth of Si on Si(111) thin-film has received considerable attention.[7-10] Pulsed laser deposition has been developed as a deposition technique that can compete with molecular beam epitaxy (MBE) and chemical vapor deposition (CVD).[11] Because of the directional nature of the plume in PLD, attenuation which is due to collisions with the background gas, is small. The pressure of the reactive gas during the growth process can be a magnitude higher than any of the other physical vapor deposition (PVD) techniques.[11]

In PLD, the deposition process consists of periodic, highly-driven growth bursts followed by periods of uninterrupted surface relaxation. This periodic nature of deposition differs from other PVD methods, and could affect the growth mechanism. Recent work shows that the use of ultrafast lasers minimizes the formation of particulates.[12-14]

Through the pulsed laser deposition combined with RHEED analysis, the high temperature transition phase from a $(1x1)_h$ to 7x7 reconstruction was affected by the PLD. Using the RHEED technique we were able to observe the two phases simultaneously existing on the surface at temperatures above the transition temperature. The reconstructed pattern started to grow on the top of the step edge and across the terraceswWhen the surface temperature was lowered below the transition temperature.

With laser fluence below the damage threshold, laser enhanced epitaxial growth shows epitaxial growth of Si on Si(111)-7x7 at room temperature. Studying the electronic excitation surface thermal expansion at room temperature shows no change in the lattice spacing at different fluencies.

In this dissertation, the main points studied are the homoepitaxial growth of Si on a reconstructed surface form of Si(111) at different temperatures, starting from room temperature to above the surface transition temperature. The experimental work on pulsed laser deposition will be discussed in several sections to clarify the progression of homoepitaxial growth of the Si. These sections can be divided as:

1) Pulsed Laser Deposition

The main purpose of this research project is to study the homoepitaxial growth modes of Si on a reconstructed surface Si(111)-7x7 during low temperatures as well as

high temperatures (above the transition temperature). RHEED was used to investigate surface roughening which allowed *in situ* real-time collection of structural information from the growth surface. The lowest epitaxial growth temperature was investigated.

2) Effect of Si deposition on the phase transition temperature

For understanding the formation of metastable structures of Si(111), it was reported that impurities are probably responsible for a secondary nuclei form of 7x7 on terraces, and this can be observed only on wide terraces with a very rapid quenching to low temperature.[15] Yang *et al.*[16] showed that the high temperature phase $(1x1)_h$ has higher density than the 7x7. These excess atoms, found on large terraces after quenching, are released when the lower density 7x7 is formed. At this case a detectable shift in the transition temperature toward a low temperature is observed.

3) Laser excitation-induced instability on Si(111)-7x7

This instability could be a bond breaking, a surface structure's changes, a top layer separation, and/or atomic mean vibrational amplitude. For growth of Si on Si(111)-7x7, the in-plane lattice constant between (11) and $(1\bar{1})$ RHEED spots has been observed as well as the epitaxial growth at room temperature.

4) Effect of the substrate temperature on the crystallite

Since its invention by Binnig *et al.*[17], atomic force microscopy has been established as a powerful method for the study of topographies at crystal surfaces. In the present work, we use an atomic force microscope, operated in non-contact mode (NC-AFM) to study the effect of temperature on the crystallite (density, shape, and size of the droplets) on the atomic scale.

5) Electron Stimulated Desorption Ion Angular Distribution (ESDIAD) was built and used as a technique to detect the direction of adsorbates on the solid surfaces. In this part, we built an instrument that measures ESDIAD images of desorbing ions in real time. We used this system to monitor the surface reactions of NaCl single crystal in real time.

In this dissertation,* each chapter will be self-contained, having its own introduction, conclusion and list of references.

* This dissertation was written in accordance with Journal of Optical Engineering and SPIE Proceedings.

I.2. References

1. M. van Hove, W. H., Weinberg, and C. M. Chan, *Low Energy Electron Diffraction*, Springer-Verlag, Berlin (1986).
2. J. W. Herman and H. E. Elsayed-Ali, "Superheating of Pb(111)," *Phys. Rev. Lett.* **69**, 1228-1231 (1992).
3. J. A. Stroscio, D. T. Pierce, and R. A. Dragoset, "Homoepitaxial growth of iron and a real space view of reflection-high-energy-electron diffraction," *Phys. Rev. Lett.* **70**, 3615-3618 (1993).
4. A. Ichimiya, T. Hashizume, K. Ishiyama, K. Motai, and T. Sakurai,"Homo-epitaxial growth on the Si(111)-7×7 surface," *Ultramicroscopy* **42-44**, 910-914 (1992).
5. B. S. Swartzentuber, "Direct Measurement of Surface Diffusion Using Atom-Tracking Scanning Tunneling Microscopy," *Phys. Rev. Lett.* **76**, 459-462 (1996).
6. P. W. Deelman, T. Thundat, L. J. Schowalter, "AFM and RHEED study of Ge islanding on Si(111) and Si(100)," *Appl. Surf. Sci.* **104-105**, 510-515 (1996).
7. U. Köhler, J. F. Demuth, and R. J. Hamers, "Scanning tunneling microscopy study of low-temperature epitaxial growth of silicon on Si(111)-(7×7)," *J. Vac. Sci. Technol. A* **7**, 2860-2867 (1989).
8. M. Horn and M. Henzler, "LEED studies of Si molecular beam epitaxy on Si(111)," *J. Cryst. Growth* **81**, 428-433 (1987).
9. H. N. Yang, G. C. Wang, and T. M. Lu, "Instability in Low-Temperature Molecular-Beam Epitaxy Growth of Si/Si(111)," *Phys. Rev. Lett.* **73**, 2348-2351 (1994).

10. T. Hasegawa, M. Kohno, S. Hosaka, and S. Hosoki, "Dynamic observation of Si crystal growth on a Si(111)-7×7 surface by high-temperature scanning tunneling microscopy," *Phys. Rev. B* **48**, 1943-1946 (1993).

11. D. B. Chrisey and G. K. Hubler, "*Pulsed laser deposition of thin films,*"John Wiley & Sons, New York (1994).

12. A. V. Rode, A. V., B. Luther-Davies, and F. G. Gamaly, "Ultrafast ablation with high-pulse-rate lasers. Part II: Experiments on laser deposition of amorphous carbon films," *J. Appl. Phys.* **85**, 4222–4230 (1999).

13. J. Dominguez, L. Fu, and X. Q. Pan, "Epitaxial nanocrystalline tin dioxide thin films grown on (0001) sapphire by femtosecond pulsed laser deposition," *Appl. Phys. Lett.* **79**, 614-616 (2001).

14. M. Hegazy and H. E. Elsayed-Ali, "Observation of step-flow growth in femtosecond pulsed laser deposition of Si on Si(100)-2×1," *J. Vac. Sci. Tech. A* **20**, 2068-2071 (2002).

15. X. H. Wei, Y. R. Li, J. Zhu, Y. Zhang, Z. Liang, and W. Huang, "*In situ* analysis of lattice relaxation by reflection high-energy electron diffraction," *J. Phys. D: Appl. Phys.* **38**, 4222-4226 (2005).

16. Y. -N Yang and E. D. Williams, "High atom density in the ''1×1'' phase and origin of the metastable reconstructions on Si(111)," *Phys. Rev. Lett.* **72**, 1862-1865 (1994).

17. G. Binnig, C. F. Quate, and Ch. Gerber, "Atomic Force Microscope," *Phys. Rev. Lett.* **56**, 930-933 (1986).

CHAPTER II

REFLECTION HIGH-ENERGY ELECTRON DIFFRACTION

II.1. Introduction

Reflection high-energy electron diffraction (RHEED)[1] is an experimentally simple technique for studying surface structures of flat surfaces,[2] for monitoring the surface phase transitions,[3-5] and the crystallographic orientation of thin film during growth.[6,7] The capability to achieve quantitative information about surface transition, surface morphology, surface reconstruction, and the growth process of thin film and its control has put the reflection high-energy electron diffraction (RHEED) technique as a superior and effective *in-situ* analysis technique in surface science.[8,9]

In RHEED, high energy electrons (~ 10-50 keV) with a variable glancing incidence (less than 3°) are back-diffracted on a solid surface. At this energy range, the probability of inelastic scattering is very high, which leaves most of the electrons elastically scattered near the surface. The electrons ability to escape without energy loss makes RHEED sensitive only to the top few atomic layers on the surface. The diffraction RHEED pattern obtained is derived mainly from the streaks' positions and shapes (a schematic illustration is shown in Fig. 2.1).

Meanwhile, compared to other diffraction techniques, the glancing incidence angle of RHEED makes it perfect to combine with other equipment, like PLD and MBE, where it is used to monitor the growth. Some assumptions are taken into account in RHEED experiments: (1) it is assumed that the electron beam is mono-energetic,

infinitesimally thin and collimated, (2) the radius of the Ewald sphere is large compared to dimensions of the surface unit mesh because of the high energy of the electron beam, and (3) flatness of the sample surface is also assumed.[10]

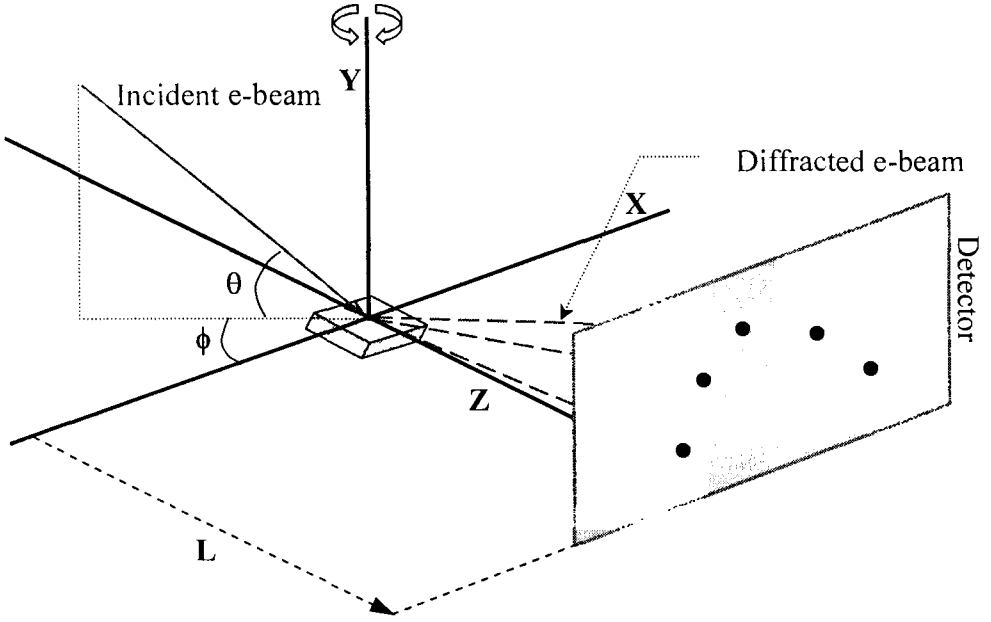

FIG. 2.1. Geometry of reflection high-energy electron diffraction, high-energy electrons (~5-100 keV) are incident on the solid surface with a variable glancing incidence (less than 3°) and are back-diffracted.

Figure 2.2. shows a comparison between RHEED patterns obtained from non-reconstructed and reconstructed surfaces for Si(111). Conceptually, for perfectly flat surfaces the diffraction pattern consists of spots arranged on "Laue" rings, Fig. 2.2(b). However, because of the non-idealities in both the electron beam and the sample's surface, streaks appear instead of spots, Fig. 2.2(a).

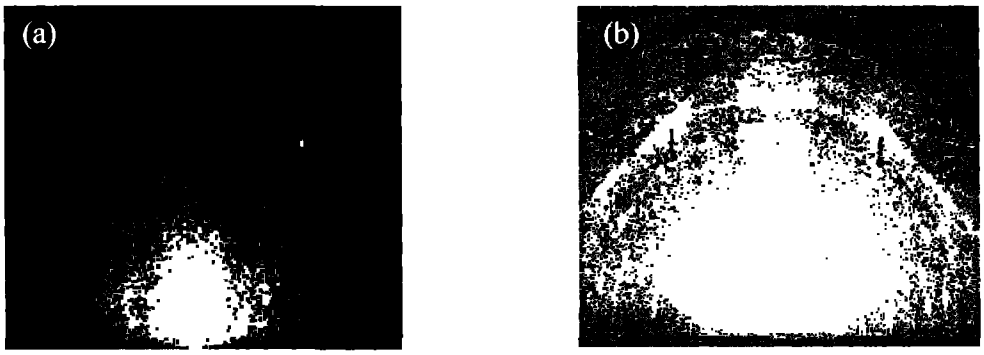

FIG. 2.2. RHEED sensitivity for surface structures and reconstructions, a Si(111), as an example, at room temperature for both (a) Si(111)-1×1, (b) Si(111)-7×7 reconstructed surface.

II.2. Experimental RHEED Setup

The simple RHEED system consists of:

(1) **Electron Gun:** A continuous wave (CW), or photo-activated electron gun that produces a collimated electron beam with energies in the range 5-100 keV. Due to the low work function, tungsten filaments are primarily used as an electron source. Electrons are then accelerated to high energy and focused using either electrostatic or electromagnetic lenses. At the end of the accelerating column, electrostatic or electromagnetic deflectors are used to control the e-beam's movement.

(2) **Sample Surface:** A contaminated sample surface can affect the quality of the RHEED pattern. Two techniques can be used to create clean sample surfaces. The technique depends on the sample size. Small samples can be cleaned in the vacuum chamber prior to RHEED analysis;[11] and large samples can be coated with a passive oxide layer that can be removed by heat treatment under the vacuum.

(3) **Vacuum chamber:** Because the gas molecules diffract the electrons and affect the surface quality of the samples, an ultra-high vacuum is required.

(4) **Phosphor screen**: it is used to transform the diffracted electrons into a visible diffraction pattern.

(5) **Charge-coupled device (CCD) camera:** it is used to capture the diffraction patterns off the phosphor screen.

II.3. Theory of RHEED

The importance of the analysis of the RHEED intensity oscillations comes from the ability to control and understand the mechanism of the thin film growth during deposition using either molecular beam epitaxy (MBE) or pulsed laser deposition (present work). Most of the measurement interpretation is based on Monte Carlo simulations,[12,13] and molecular dynamics calculations.[14] Both methods take into account the atomistic processes, such as deposition and surface diffusion. A complete idea of the surface morphology can be achieved through the analysis of RHEED spots as a function of time and temperature.

II.3.A. Geometry of RHEED

For simplicity, assume an idealized RHEED where (1) the incident electron beam is mono-energetic, infinitesimal, and collimated; (2) a high energy electron beam is used such that the radius of the Ewald sphere is very large compared to the dimensions of the unit mesh; (3) zero incidence angle; and (4) flat sample surface.

A geometric model [1] is used to describe RHEED, in which diffraction of a plane wave (of wave vector $\vec{k}$) by a single crystal is assumed. This theory is widely used for experimental calculations. In this theory, diffraction results when the Laue condition is satisfied, i.e.,

$$\vec{k}' - \vec{k}_0 = \vec{G}, \tag{2.1}$$

where $\vec{k}'$ and $\vec{k}_0$ are the wave vectors for the diffracted and the incident beams, respectively, and $\vec{G}$ is the reciprocal-lattice vector. In the special case of elastic scattering; $|\vec{k}| = |\vec{k}_o|$, this condition is satisfied by an infinite number of $\vec{k}'$ vectors pointing in all directions, which is the origin of the so-called Ewald sphere. A Ewald sphere is a sphere that has the origin as the origin of the $\vec{k}_0$, and a radius $\vec{k}_0$. Hence, the Laue condition may be re-formalized as "diffraction occurs for all k' connecting the origin of the sphere and a reciprocal-lattice point.[1,15] The magnitude of the wave vector is given by the relativistic expression

$$k_0 = \frac{2\pi}{\lambda} = \frac{1}{\hbar}\sqrt{2m_0 qV + \left(\frac{qV}{c}\right)^2}, \tag{2.2}$$

where m_0 is the electron rest mass, q is its charge, and V is the accelerating potential. Expression (2.2) is sometimes written as

$$\lambda = \frac{h}{\sqrt{2m_0 qV + \left(\frac{qV}{c}\right)^2}} \cong \frac{12.3}{\sqrt{V(1+1.95\times10^{-6}V)}}, \tag{2.3}$$

where the wavelength λ is measured in Å and V is in volts.

The geometric model is used successfully to calculate the lattice spacing in the reciprocal space. A simple way to describe that is to consider Fig. 2.3, which is a top

view showing the projection of the reciprocal space. The spots in the RHEED pattern are the result of the intersections of the Ewald's sphere with the reciprocal lattice rods. What is seen on the phosphor screen is the projection of these spots. By applying the principle of similar triangles to the two triangles at the bottom of the figure (the shadowed triangle and the bigger one), it is easy to see that $W/L \sim a^*/(2\pi/\lambda)$. Hence,

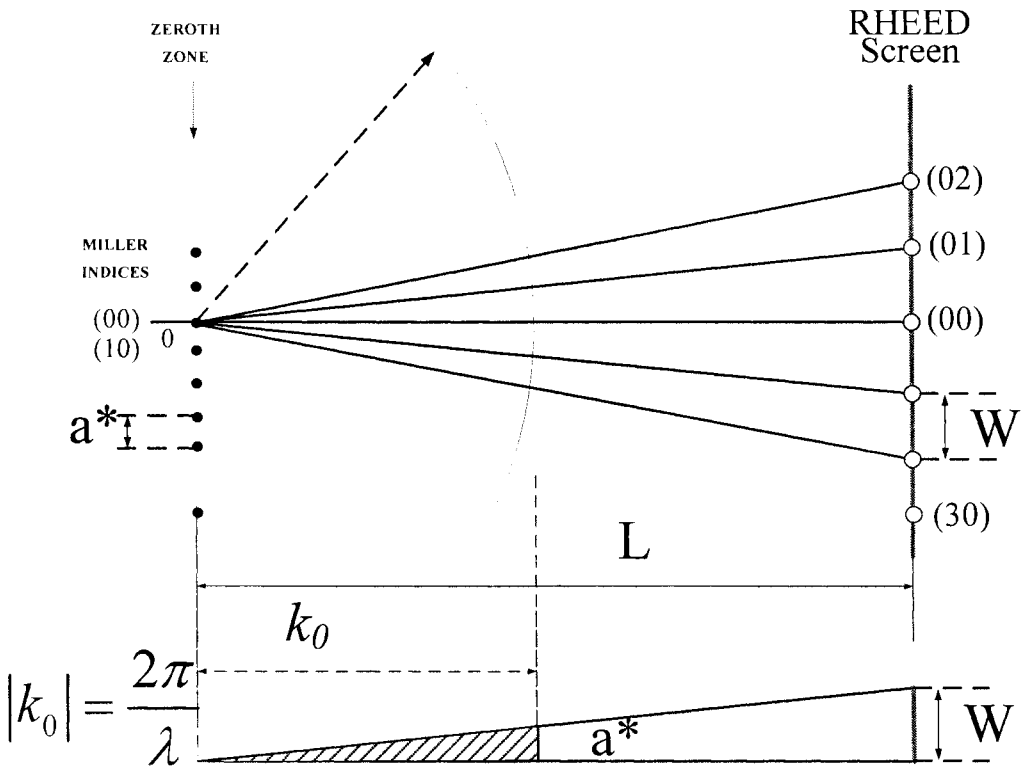

FIG. 2.3. A plan view describing the relation between the intrarow spacing of the reciprocal lattice of the zeroth zone and the spacing of the RHEED streaks according to the geometrical model.

$$a^* = \frac{2\pi W}{\lambda L}, \tag{2.4}$$

where W is the streak separation, and L is the sample to screen distance.

II.3.B. Kinematical and Dynamical Model

The Schrödinger equation for the wave-function of the scattered wave, $\psi(\underline{r})$, is given, in terms of effective potential $U(\underline{r})$,[1,16]

$$\left(\frac{-\hbar^2}{2m}\nabla^2 + V(r)\right)\psi(r) = E\psi(r) \tag{2.5}$$

Or

$$\left(\nabla^2 + U(\underline{r}) + k_0{}^2\right)\psi(\underline{r}) = 0\,. \tag{2.6}$$

where

$$U(r) = \frac{2m}{\hbar^2}V(r)\,,\ \text{and}\ k_0 = \frac{2m}{\hbar^2}E \tag{2.7}$$

In almost all scattering problems, we deal with short-range potentials, *i.e.*, $V(r) \approx 0$ beyond a certain distance, $|r| \sim a$, where a is the scatter size. In all applications, including RHEED, we are interested in measuring the scattered electrons far away from the scattering center, i.e. $|r| \sim a$, which is realistic since the detector is always located at distances much larger than the scattering center. Hence,

$$\left(\nabla^2 + k_0{}^2\right)\psi(\underline{r}) = 0\,. \tag{2.8}$$

This is the plane wave (free particle) equation that has the eigenfunctions $\varphi(r) = e^{i\vec{k}\bullet\vec{r}}$ and the eigenvalues $E = \dfrac{\hbar^2 k^2}{2m}$.

Now, in the neighborhood of the scattering centers, we would like to find the modification of the eigenfunctions in the presence of the scattering potential. This is the well-known scattering problem, which is solved by different techniques.[17,18]

Considering the "Lippmann-Schwinger" treatment, which is described in Ref. [17], we start by rewriting equation (2.5) using the "ket" notation,[18]

$$(H_0 + V)|\psi\rangle = E|\psi\rangle \tag{2.9}$$

Or

$$(E - H_0)|\psi\rangle = V|\psi\rangle \tag{2.9*}$$

Roughly, we may write

$$|\psi\rangle = \frac{V}{(E - H_0)}|\psi\rangle \tag{2.10}$$

To go around the pole of $1/(E - H_0)$, we may specify a boundary condition to the solution. We may write $1/(E - H_0 + i\varepsilon)$ where we take the limit $\varepsilon \to +0$ at the end of the calculations. In this notation, the plane wave solution away from the scattering center $|\varphi\rangle$ satisfies the equation $H_0|\varphi\rangle = E|\varphi\rangle$. Therefore, the solutions must satisfy the condition $|\psi\rangle \to |\varphi\rangle$ as $V \to 0$. Therefore, the solution could be written as

$$|\psi\rangle = |\varphi\rangle + \frac{V}{(E - H_0 + i\varepsilon)}|\psi\rangle. \tag{2.11}$$

This is the so-called "Lippmann-Schwinger" equation. Multiplying Eq. (2.11) by the "bra" $\langle\vec{r}|$,

$$\langle\vec{r}|\psi\rangle = \langle\vec{r}|\varphi\rangle + \langle\vec{r}|\frac{V}{E - H_0 + i\varepsilon}|\psi\rangle \tag{2.12}$$

II.4. RHEED pattern of Si(111)-1x1

In real (non-flat) surface, streaks or elongated spots are common to the RHEED patterns. The reciprocal lattice that has lowest orders intersects with the Ewald sphere at small angles, causing the divergence for the electron beam (in this case, electrons have a range of energies). The Ewald sphere streaks appear at the perfect points, i.e. where the broadened roads intersect. Silicon has a diamond structure, which is shown in Fig. 2.4.

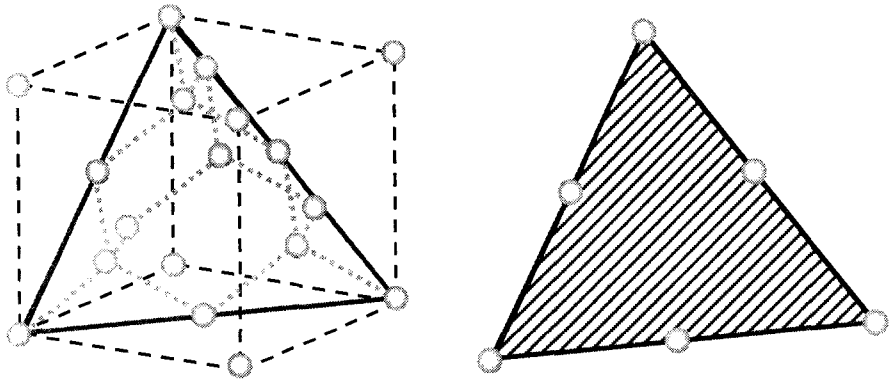

(a) (b)

FIG. 2.4. (a) Diamond lattice structure of Silicon crystal lattice, (b) sketch of the Si(111) plane.

Real and reciprocal lattice of Si(111)-1x1

The reciprocal lattice is a set of imaginary points constructed in such a way that the direction of a reciprocal lattice vector from one point to another coincides with the direction normal to the real lattice planes. The separation of those points is equal to the reciprocal of the real inter-planar distance. Suppose the lattice vectors for a real lattice

unit cell are $\bar{a}_1$, $\bar{a}_2$, and $\bar{a}_3$ then the reciprocal lattice vectors are $\bar{a}_1$*, $\bar{a}_2$*, and $\bar{a}_3$*. For two-dimensional lattice, the expression becomes:

$$\bar{a}_1^* = 2\pi \frac{\bar{a}_2 \times \hat{n}}{A} \tag{2.13}$$

$$\bar{a}_2^* = 2\pi \frac{\hat{n} \times \bar{a}_1}{A} \tag{2.14}$$

where the area A is

$$A = \bar{a}_1 \bullet (\bar{a}_2 \times \hat{n}) \tag{2.15}$$

where $\hat{n}$ is the unit vector of the surface normal direction. A is then reduced to the area of the unit cell of the reciprocal lattice. The reciprocal lattice points are then extended in the surface normal direction and become the reciprocal lattice rods. The RHEED pattern of a surface structure is a projection of the reciprocal lattice rods on the phosphor screen through the Ewald sphere. In Si(111), the crystalline net of the surface is a closed-packed hexagonal array. An incident electron beam (with energy ~8.6 keV) along the <100> direction with angle of incidence of ~3° was used to calculate the reciprocal lattice parameters, as shown in Fig. 2.5. The surface net and reciprocal net used for lattice parameters calculations are shown in Fig. 2.6.

FIG. 2.5. Experimental RHEED pattern of Si(111), with the incident beam along <112> where the angle of incidence ~3°. A high quality of the Kikuchi lines was also seen.

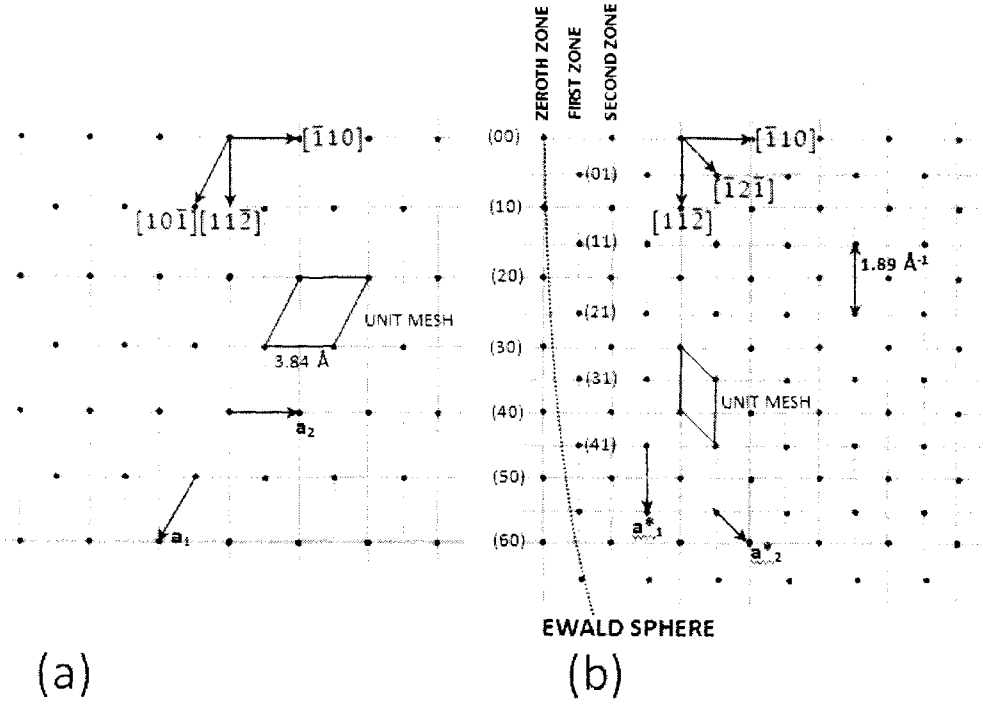

FIG. 2.6. Calculations of the real (a) and the reciprocal (b) nets of Si(111).

The lattice parameter is a = 5.43 Å. So, using FIG. 2.10, the real lattice vectors of Si(111) mesh are

$$\bar{a}_1 = \frac{5.43}{2}\langle 10\bar{1}\rangle = 2.72\ \langle 10\bar{1}\rangle \text{ Å},$$

$$\bar{a}_2 = \frac{5.43}{2}\langle \bar{1}10\rangle = 2.72\ \langle \bar{1}10\rangle \text{ Å},$$

and the unit vector normal to the surface is $\hat{n} = \frac{1}{\sqrt{3}}\langle 111\rangle$.

The net point spacing is 3.84 Å.

The corresponding basis vectors of the reciprocal net are:

$$\bar{a}_1^* = \frac{2\pi}{3*(5.43/2)}\langle 11\bar{2}\rangle = 0.77\langle 11\bar{2}\rangle \text{ Å}^{-1},$$

$$\bar{a}_2^* = \frac{2\pi}{3*(5.43/2)}\langle \bar{1}2\bar{1}\rangle = 0.77\langle \bar{1}2\bar{1}\rangle \text{ Å}^{-1},$$

and the point spacing of the reciprocal net is 1.89 Å^{-1}.

Si(111) has fourteen spots in the first zone for the beam energy, as shown in Fig. 2.7(a). For incident beam along $\langle 11\bar{2}\rangle$ comparing with the <110>, the streak spacing is large, as shown in Fig. 2.7(b).

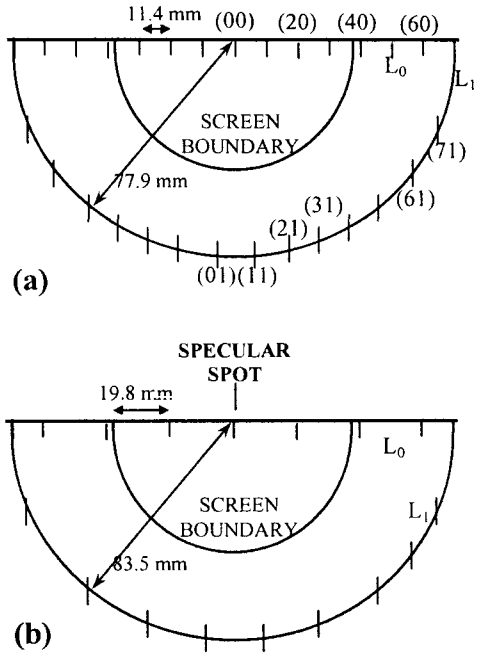

FIG. 2.7. RHEED patterns of Si(111), where the incident beam along (a) <110>, and (b) along <112>, [after ref. 19].

II.5. RHEED pattern of Si(111)-7x7

Two basic concepts are directly related to the reconstruction occurring on the semiconductor surface: chemical bonding and charge density. In elemental semiconductors, the atoms are bonded together by directional covalent bonds; and in the compound semiconductors, atoms are bonded by partial covalent and partial ionic bonds. When a surface is formed, some of these bonds are broken, leading to the associated surface charge densities that have only one unpaired electrons. Such 'cut' bonds are called 'dangling' bonds. The lack of electron pairing makes dangling bonds unstable, requiring the surface atoms to seek new coordinates. At this point, the atoms in the

surface region relax from their bulk positions in order to reduce the surface-free energy and form new bonds. The surface reaches a structure that exhibits a local minimum in the surface free energy, thus, implying that the chemical valences of the surface species are fulfilled in the surface reconstruction geometry.

For a typical surface, multiple local minima that are associated with different surface structures occur in the free energy.[20] In this case more information is required to describe which structure occurs in a given situation. Not only does the surface of the semiconductor exhibit relaxed atomic positions, but also shows different chemical compositions from the bulk, even for clean surfaces. These compositions are controlled by the requirement that the surface region be charge neutral.[21] This requirement leads to the prediction of certain stoichiometries for the surface compounds. Which composition actually occurs depends on the condition under which the surface is prepared. If the bulk semiconductor is uncharged (i.e., has no space charge region at the surface), then the surface compound is uncharged and the surface is said to be auto-compensated. In general, a semiconductor exhibits a space charge region, in which case, the surface compound contains just enough charge to render the entire space charge region electrically neutral. In this situation, the charge in the surface compound is typically achieved by the generation of charged defects in an otherwise periodic auto-compensated structure.[22]

The Si(111) surface provides an illuminating example of the reconstructed surface. The low temperature cleavage generates a (2x1) structure, which upon heating first becomes a (5x5) and then a (7x7) structure, and upon further heating the surface disorders to give a $(1x1)_h$ structure. Thus, the kinetic accessibility as well as ground-state

free energy play an important role in determining which of the various possible reconstructions actually occur under specific preparation conditions.

Several surface structural models have been proposed to describe the surface reconstruction. The most consistent with all the available experimental results is the Takayanagi model.[23] In this model, the reconstruction is described by the dimer adatom stacking fault (DAS) model and characterized by:

1) a dimerization of second-layer atoms,
2) existence of adatoms, and
3) stacking fault between the first and the second is over one-half of the 7x7 unit cell.

The ideal (unrelaxed) 7x7 structure would contain 49 Si atoms in every surface layer, according to DAS model, the 7x7 reconstruction has:

1) 12 adatoms in T_4 sites in a 2x2-like arrangement in the top layer,
2) 6 rest atoms, three-fold coordinate,
3) 9 dimers along the boundary of the faulted half of the surface unit cell, and
4) a corner hole.

Total of 102 Si atoms exist in the top of three layers of the 7x7 unit cell. These can be concluded as: 12 atoms in the adatom layer, 42 atoms in the restatom layer, and 48 atoms in the layer containing the stacking fault, as shown in Fig. 2.8(a) and Fig. 2.8(b). The density of atoms at the 7x7 reconstruction surface is 4% higher than the atom density on the unreconstructed surface. Therefore, the formation of the reconstruction is accompanied by material transport.

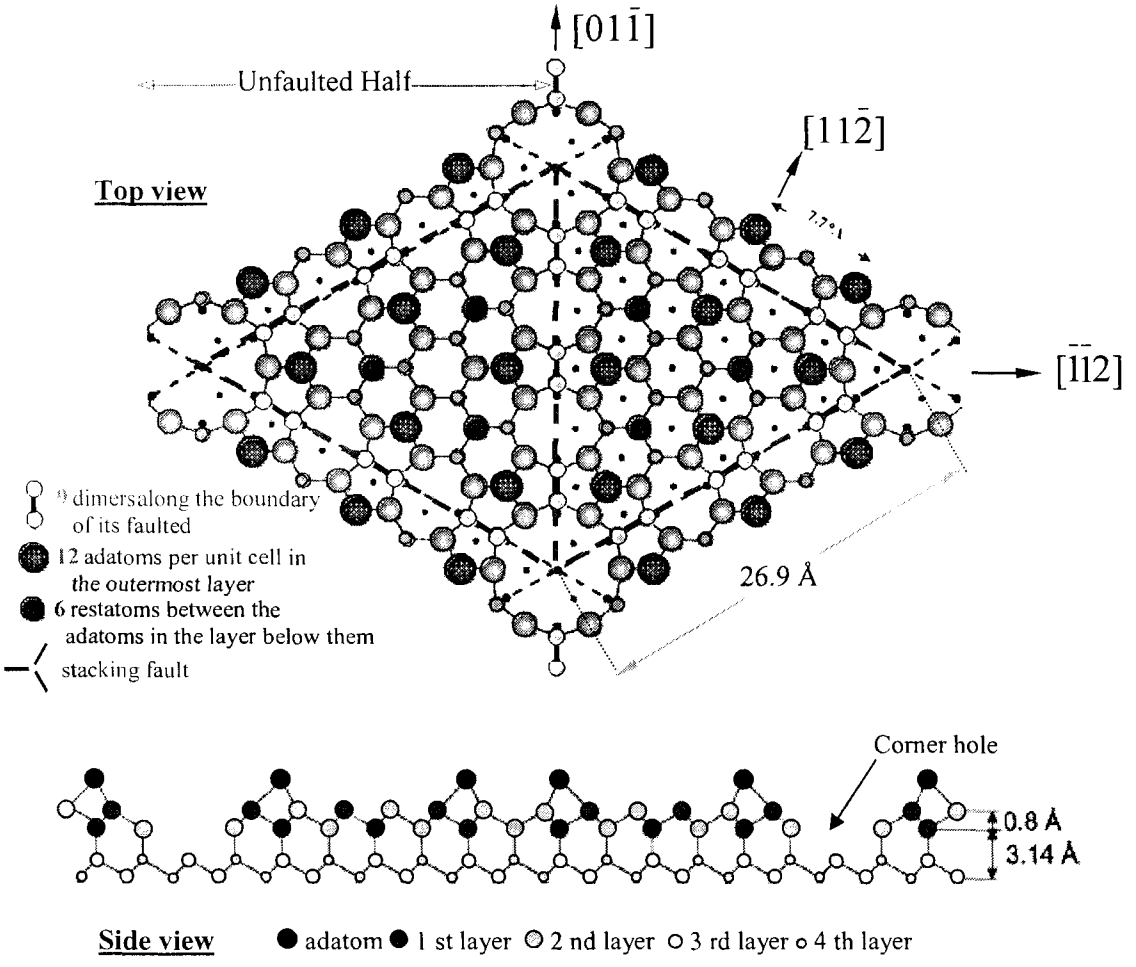

FIG. 2.8(a). Unit mesh of the Si(111)-7x7 surface reconstruction according to dimers, adatoms and stacking fault (DAS) model with the unit cell of (7x3.84 Å) 26.9 Å. DAS reconstruction in one-half of the unit cell lead to a reduction of the surface energy on the reconstructed surface compared to the unreconstructed surface.

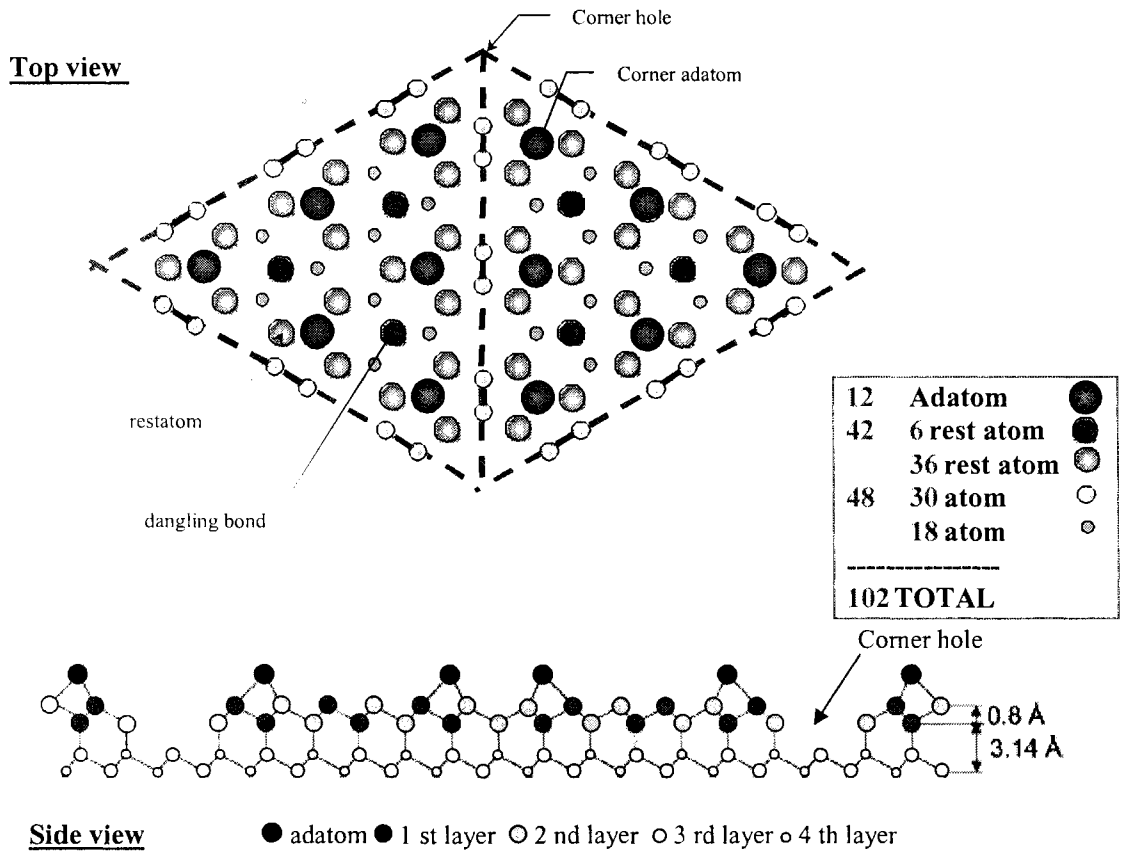

FIG. 2.8(b). Supercell of the Si(111)-7x7 surface reconstruction according to DAS model [after ref. 23].

II.6. Surface reconstruction of Si(111)

Surface at the Si(111)-7x7 surface have been studied using Reflection High-Energy Electron Diffraction, by measuring the superlattice-spot intensity from a clean surface during the phase transition between (7x7) and (1x1) structure. This phase transformation is characterized by the disappearance of all fractional $\frac{1}{7}$ order. Debye-Waller analysis of the temperature dependence of the RHEED intensity was also applied.

Lander[24] reported that the surface transformation of the (7x7) structure to (1x1) using LEED. This phase transformation was found to be reversible around 850°C. Using RHEED, the diffuse spots were reported at positions of the superlattice Bragg spots of $(\sqrt{3}x\sqrt{3})R30^{\circ}$ structure in the high temperature (1x1) stage.[25]

The nature of this transition depends on the structure of the $(1x1)_h$ (high-temperature phase) as well as the (7x7) dimer-adatom stacking-fault (DAS) structure at low temperatures.[26] A few theoretical studies were reported to explain the structural transition $7x7 \leftrightarrow 1x1$.[27,28] We studied the surface reconstruction of Si(111)-7x7 by measuring the RHEED intensity at different temperatures in a wide temperature range (20 to 900° C) to calculate the effective surface Debye temperature.

II.6.A. Mean vibration amplitude and Debye-Waller factor

In the kinematic model of electron diffraction, the atoms are treated as rigidly located on the lattice sites. By this way, the spacing between the RHEED streaks can be explained. Meanwhile, the atoms actually vibrate randomly at temperatures above 0 K in their lattice origins. The thermal vibration of atoms causes the de-phasing effect on the diffracted electron beam, resulting in thermal diffuse scattering of the beam and in the decrease of the beam peak intensity. The magnitude of the thermal de-phasing effect on the RHEED intensity is related to the mean vibrational amplitude by Debye-Waller extinction, which can be expressed as:

$$I(T) = I_0 e^{(-2MT)}, \tag{2.16}$$

where I_0 is the intensity at (T = 0K), and $2MT = \langle \mathbf{S}.\mathbf{u} \rangle^2$, where $\mathbf{S} = \mathbf{k} - \mathbf{k_0}$ is the momentum transfer of the diffracted electron and **u** is the atomic vibrational vector. In

the quasiharmonic approximation, $\langle \mathbf{S}.\mathbf{u} \rangle^2 = \mathbf{S}.\langle \mathbf{u}^2 \rangle$, where u is the projection of the atomic vibrational amplitude vector along the direction of momentum transfer, and $\langle u^2 \rangle = [3\hbar^2 T/mk_B\theta_D^2]$ T. θ_D is the Debye temperature, $\hbar$ is the Plank's constant, k_B is the Boltzman's constant, and m is the atomic mass. Therefore, the Debye-Waller factor is given by $2M = S.[3\hbar^2 T / mk_B\theta_D^2]$. The Debye temperature can then be obtained from the Debye-Waller extinction of the diffracted electron beam intensity.

The experiment was performed in an UHV chamber equipped with a RHEED system. The residual gas pressure was less than $5x10^{-10}$ torr. The electron beam energy was 9 keV. The investigated sample was a p-type Si(111) wafer with resistivity between 20-50 Ωcm, and the sample size was 5x4x0.4 mm^3. The surface of Si(111) was first chemically etched by immersing the sample in a solution of H_2SO_4 and H_2O_2 (4:1) for 10 minutes, then exposing the sample to a 10% hydrofluoric acid (HF) for 1 min, the sample was rinsed with de-ionized water for 10 minutes, then the whole process was repeated once more. This treatment is known to remove native oxide and terminate the surface silicon dangling bonds with hydrogen. A clear (7x7) RHEED pattern was observed after flashing the sample to a temperature of 1200 °C for up to 2 minutes by applying direct current. The sample was cooled slowly between 1000 °C and 800 °C to ensure a good and clear (7x7) reconstruction. The cleanliness of the sample could be checked using Auger Analyzer. The sample's temperature was measured using Pt/PtRh(10%) thermocouple pressed against the surface of the sample with an error of ±2 °C (calibrated in both the freezing temperature of water and the melting point of Ge), in addition to optical infrared pyrometer with compensating emissivity of 0.5 and ±10 °C accuracy.

High-energy electrons with primary energy 9 keV are incident with a grazing angle (<3°) onto the sample's surface, and the diffracted beams are observed on a fluorescent screen. The fluorescent screen needs no high-voltage source and no acceleration of the electrons is necessary since the high primary energy is sufficient to produce fluorescence. The screen is planar and is coated onto the inside of a window of the UHV system, along with a conducting film to prevent charging. No energy filtering of inelastic and secondary electrons is necessary since the diffracted beams are much more intense than the background. At the phosphor screen, a typical RHEED image consists of bright spots against a diffuse background. The arrangement of these bright spots on the screen is related to the arrangement of atoms at the surface.

Si(111) is one of the lowest energy surfaces of this element, but when the crystal is cleaved at room temperature, the (2x1) reconstruction appears.[28] Heating around 250 °C, a 1x1 RHEED pattern appears. With increasing temperature, higher than 400 °C, a 7x7 superstructure occurs, indicating an extremely long-range periodicity. The DAS structure is, therefore, more stable energetically; but it requires atom exchange, which is not possible at RT. At 830 °C, the 7x7 pattern disappeared and was replaced reversibly by a simple 1x1 pattern.

The 7x7 structure is one of a family of DAS structures of the form (2n+1)x(2n+1); the smallest of these (3x3), in comparison with the unreconstructed 1x1. M.C. Payne *et. al.*[29] started to calculate the energy of DAS structures. Since the basic adatom unit is in a 2x2 arrangement, other possible arrangements are also approached. There was an enormous effort spent on calculating the energy of the 7x7.[11] Indeed, the 7x7structure has lower energy than both the 3x3 and 5x5, and also lower energy than the

2x1; for this reason, the 7x7 structure is the most stable one. Values of these energies are shown in Table 2.1.

The stacking fault in the DAS structures enable dimers to form along the cell edges and the ring at the corners of their intersection. Without the stacking fault, we simply have the adatoms, which are arranged in a 2x2 array. The Ge(111) structure is thought to be based simply on these adatoms; within the cell there are two local geometries, subunits of 2x2 and c2x4; together, they make the larger c2x8 reconstruction as determined by X-ray diffraction.[30] Takayanagi and Tanashiro[28] generalized their Si(111)-7x7 model to produce a model of Ge(111)-c2x8 based on dimer chains.

The high temperature 1x1 structure of the Si is known to form a disordered structure of mobile adatoms which may locally be in the 2x2 or a similar configuration. Diffuse scattering from these adatoms has been seen for both Si(111) and Ge(111), e.g., using RHEED[31] and Medium-Energy Ion Scattering.[32] Similar structures are expected on Ge/Si mixtures, where Ge segregates to the surface because of the lower binding energy.

Table 2.1. Calculated Energies of reconstucted Si(111) surfaces (eV/ surface atom).[28]

Reference	1x1 relaxed	2x1 cleaved	2x2 adatom	3x3 DAS	5x5 DAS	7x7 DAS
Si(111) Payne '87	1.15		1.04	0.88		
Meade '89	1.39		1.12			
Stich '92				1.196	1.168	1.153
Brommer '92		1.239				1.179

D. Vanderbilt[33] tries to estimate the energy costs of the stacking fault (f) and of the corner holes (c), expressed as a ratio to the dimer wall energy. He then draws a 'phase

diagram'. This exhibits a series of DAS structures if "f" is small, which has increasing (2n+1) periodicity as "c" increases. At larger values of "f", the stacking fault is unfavorable, and there is a 'transition' to an ordered adatom structure.

II.6.B. Characteristics of Si(111)-7x7 RHEED pattern

An accelerated voltage of the incident electrons ~9 keV was used with an azimuthal angle rotated in the direction 3.5° from the $[11\bar{2}]$ direction. The Debye Waller curve and Debye temperature were measured. The integrated intensity of the specular reflection was plotted as a function of glancing angle (θ). The RHEED intensity of the 7x7 structure changes with the varying azmiuthal angle, glancing angle and acceleration voltage, as shown in Fig. 2.9(a). Diffraction intensity distribution can be noticed by observing the superlattice reflection spots of the RHEED patterns. The strongest spots appear at $(\frac{3}{7}\,0)$, $(\frac{4}{7}\,0)$, $(\frac{3}{7}\,\frac{1}{7})$, $(\frac{4}{7}\,\frac{\bar{1}}{7})$ positions and their equivalent. The characteristics for the given (h k) rods of the 7x7 structure can be summarized as: the RHEED patterns have three-fold symmetry. $(\frac{3}{7}\,0)$, $(\frac{4}{7}\,0)$, $(\frac{3}{7}\,\frac{1}{7})$, $(\frac{4}{7}\,\frac{\bar{1}}{7})$ rods show the strongest intensity. $(\frac{1}{7}\,0)$, $(\frac{6}{7}\,0)$ rods show medium intensity. $(\frac{1}{7}\,\frac{1}{7})$, $(\frac{2}{7}\,0)$, $(\frac{2}{7}\,\frac{1}{7})$, $(\frac{2}{7}\,\frac{2}{7})$ rods and equivalent ones generally show weak intensity. $(\frac{2}{7}\,0)$ rod and equivalent ones generally show weaker intensity than $(\frac{1}{7}\,0)$ rods. The electron beam is inelastically scattered by interaction with the atoms.

These electrons are scattered coherently when Bragg's law is satisfied at a suitable set of reflecting planes, causing Kikuchi pairs as shown in Fig. 2.9(b).

The 2-dimensional images are shown in Fig. 2.10. where the change in Si(111) structure from 7x7 to 1x1 with increasing temperature can be noticed. The superlattice spots ($\frac{1}{7}, \frac{2}{7}, \frac{3}{7}$, etc..) start to disappear until the transition temperature ~830 °C is reached. A 3-dimensional plot of RHEED pattern of Si(111) obtained with different temperature is also shown in Fig. 2.11.

II.6.C. Surface Debye temperature of Si(111)-7x7

Thermal vibration of surface atoms is one of the important parameters in understanding the surface structure. In general, surface atoms have less number of nearest neighbors than atoms in the bulk, which cause the atoms to vibrate more intensely than do the bulk atoms. The vibration amplitude increases with increasing lattice temperature which affects the surface phase transition temperature. In other words, the Debye-Waller effect describes the reduction in elastic diffraction intensity with increasing lattice temperature.[35]

In this part, atomic vibrations are assumed to be harmonic. Electron beam was incident with a small grazing angel (~2°) such that the bulk Debye-temperature effect becomes small and does not affect the diffraction intensity from the surface. The clean and strong 7x7 reconstruction was obtained as described above. A 9 keV electron beam is incident on the Si(111)-7x7 along $[\bar{1}2\bar{1}]$ direction. To determine the Debye-temperature we calculated the RHEED intensity at various temperatures using the dynamical

diffraction theory.[36] In this case, the RHEED intensity for the (00) spot was monitored using the CCD camera in the temperature range 300 to 1270 K.

Figure 2.12. represents the change in the integrated spot intensity corrected with the Debye-Waller for the (00) spot. The transition temperature of (7x7) to (1x1) is measured to be around 830 °C. The effective Debye temperature θ_D is obtained from the Equation 2.17.[35]

$$M = \frac{|\Delta k_n|^2}{|\Delta k_o|^2}|\Delta k_o|^2 \frac{\langle u^2(T)\rangle}{T} = \frac{|\Delta k_n|^2}{|\Delta k_o|^2}(\frac{4\pi}{\lambda}\sin\theta)^2 \frac{3\hbar^2}{mk_B\Theta_D} \qquad (2.17)$$

The attenuation of the RHEED intensity is due to the increase in the temperature results from the thermal vibration of the atoms. The slope M of ln[I(T)] vs T gives the surface Debye-temperature θ_D = 579 K which was obtained below the transition temperature (830 °C). Since atoms at the surface have less numbers of nearest neighbors than do the surround atoms in the bulk, θ_D is smaller than the bulk ($\theta_{D(bulk)}$ = 675 K).[37] Controversy, surface Debye temperature was higher than that reported by Y. Fukaya *et al.* (510 K) who used the Rocking curve at room temperature for the measurement.[38] This disagreement is alleviated when θ_D is thought of to be composed of the surface (θ_S) and the bulk (θ_B).

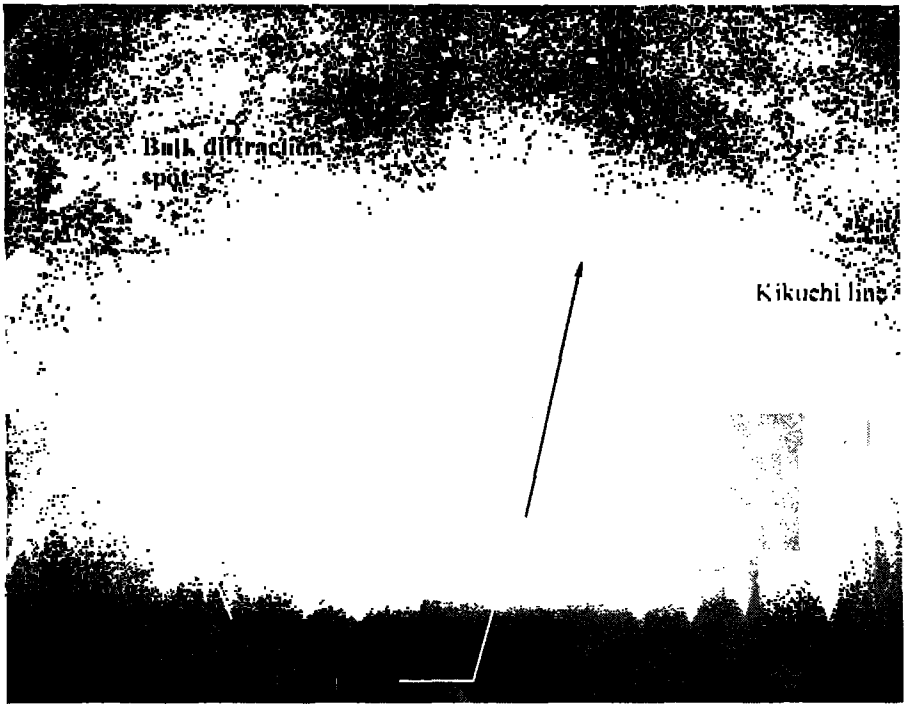

(a)

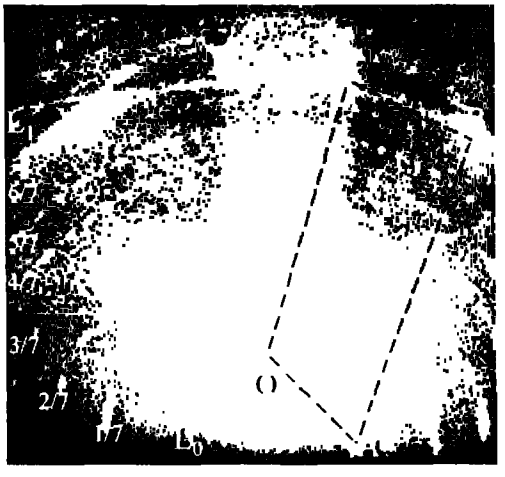

(b)

FIG. 2.9. RHEED spots pattern taken from Si(111)-7x7 structure at [11$\bar{2}$] azimuth represents: (a) super-lattice spots, specular beam, streaks, Kikuchi lines, bands, and shadow edge as well as (b) the reciprocal lattice unit cell (OABC), and Laue zone.

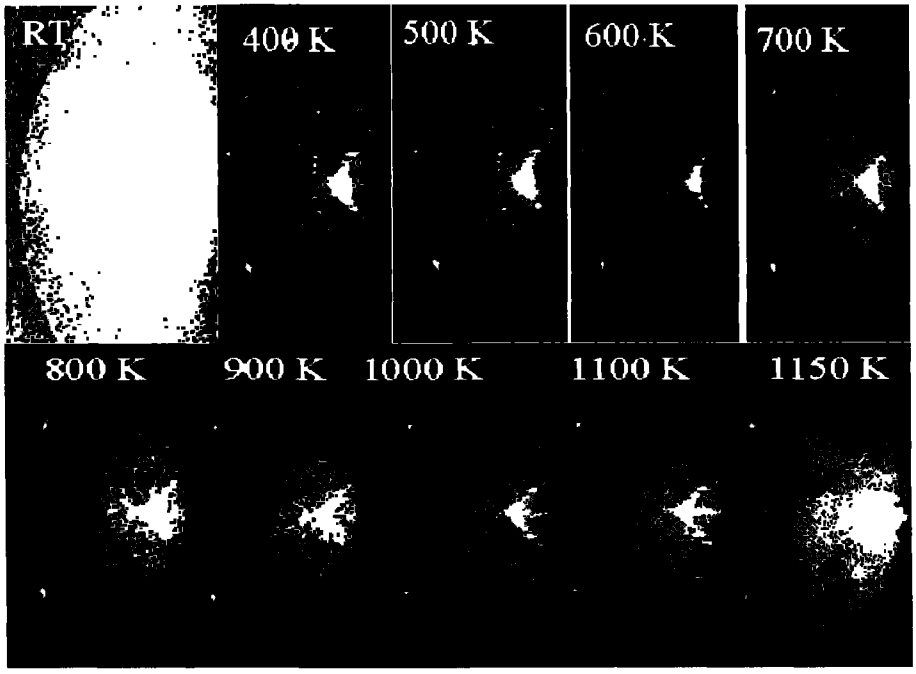

FIG. 2.10. Reconstructed RHEED patterns of Si(111) transformation (7x7)↔$(1x1)_h$ at different temperatures. The electron beam was 9 keV incidents along $[\bar{1}2\bar{1}]$.

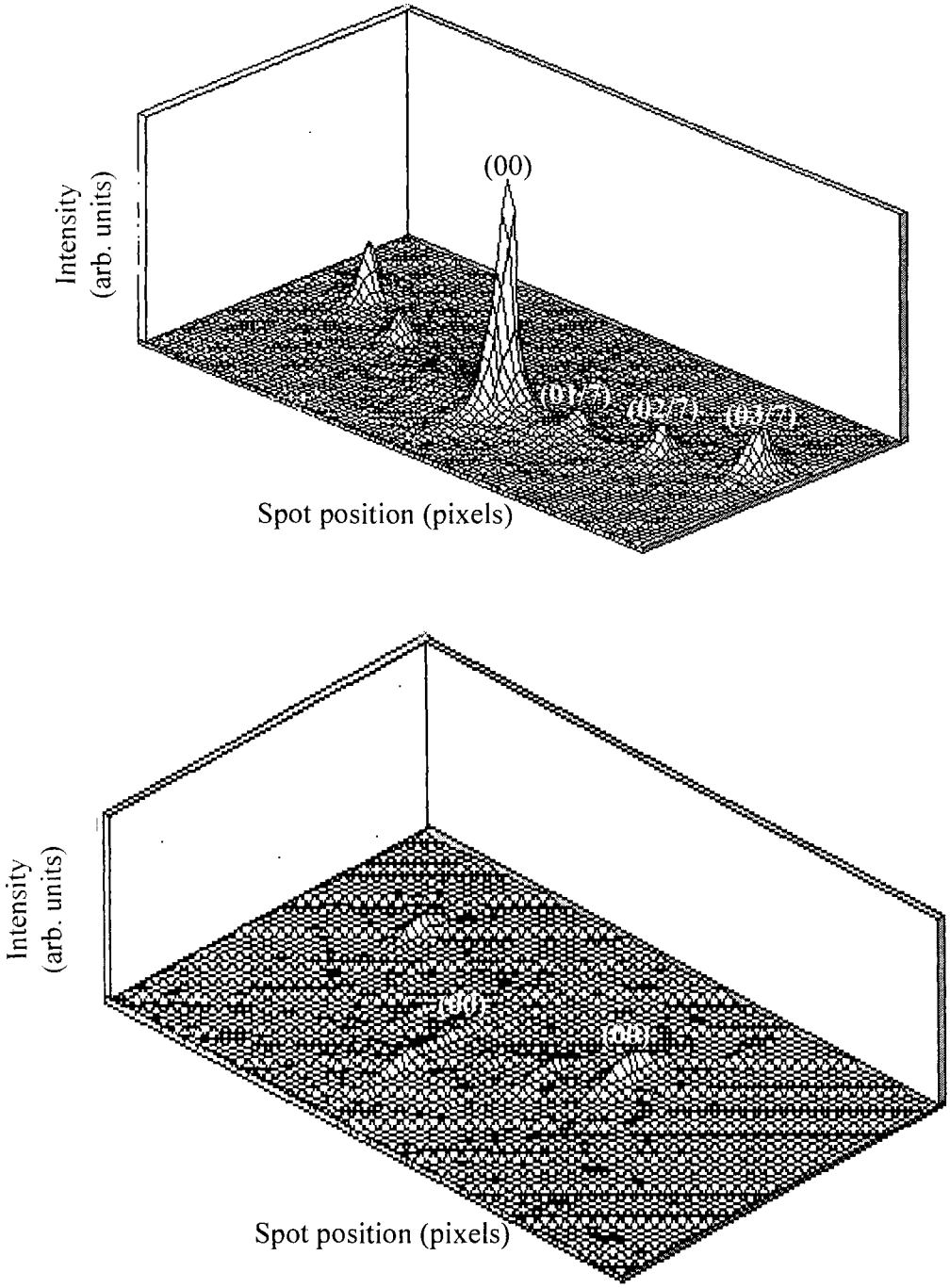

FIG. 2.11. 3-D spots intensity of Si(111)-7x7, (a) at room temperature shows the peak intensity for (00), $(0\frac{1}{7})$, $(0\frac{2}{7})$, and $(0\frac{3}{7})$ spots; (b) at surface transition temperature ~830 °C shows the Si(111)-$(1x1)_h$.

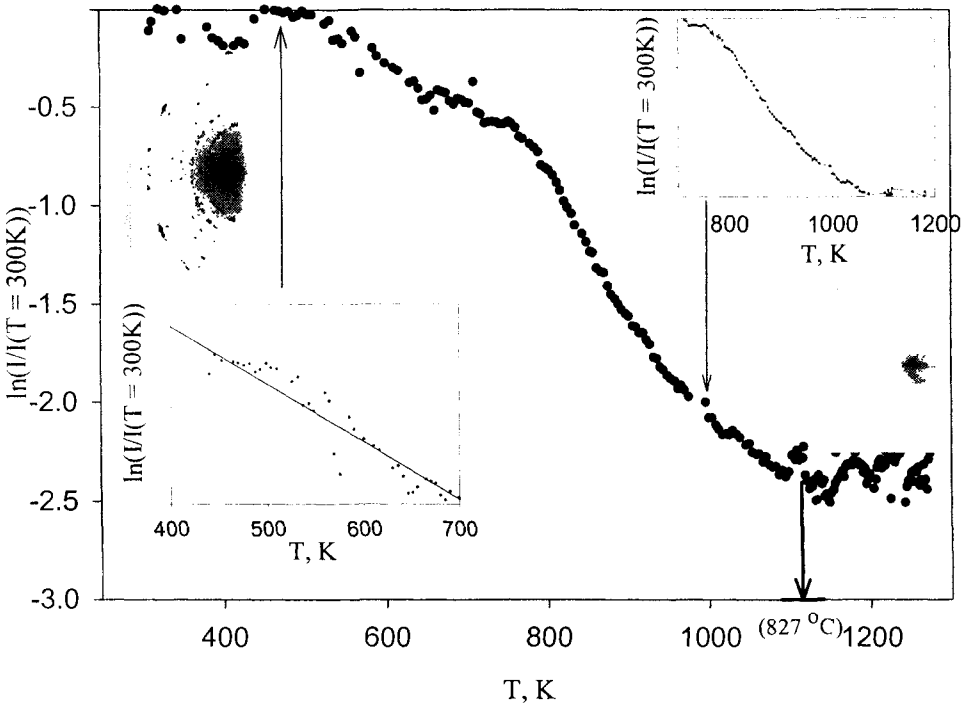

FIG. 2.12 Normalized RHEED intensity of the (00) spot for (7x7)-(1x1) phase transition at electron beam energy 9 keV and incident angle 2° and θ_D is 587 K.

II.7. References

1. W. Braun, *Applied RHEED: reflection high-energy electron diffraction during crystal growth,* Springer-Verlag, New York (1999).
2. K. Britze and G. Meyer-Ehmsen, "High energy electron diffraction at Si(001) surfaces," *Surf. Sci.* **77**, 131-141 (1978).
3. X. Zeng, B., Lin, I. El-Kholy, and H. Elsayed-Ali, "Time-resolved reflection high-energy electron diffraction study of the Ge(111)-$c(2\times8)$–(1×1) phase transition," *Phys. Rev. B* **59**, 14907-14910 (1999).
4. X. Zeng, B., Lin, I. El-Kholy, and H. Elsayed-Ali, "Time-resolved structural study of the Ge(111) high-temperature phase transition," *Surf. Sci.* **439**, 95-102 (1999).
5. M. Itoh, "Relation between surface reconstructions and RHEED intensity oscillations," *Phys. Rev. B* **58**, 6716-6719 (1998).
6. J. Y. Lee, J. Y. Juang, J. H. Ou, Y. F. Chen, K. H. Wu, T. M. Uen, and Y. S. Gou, "RHEED intensity oscillations in homoepitaxial growth of $SrTiO_3$ films," *Physica B* **284-288**, 2099-2100 (2000).
7. K. Inumaru, T. Ohara, S. Yamanaka, "Pulsed laser deposition of epitaxial titanium nitide on MgO(001) monitored by RHEED oscillation," *Appl. Surf. Sci.* **158**, 375-377 (2000).
8. LS. -J Peng, X. X. Xi, and B. H. Moeckly, "Strain relaxation during *in situ* growth of $SrTiO_3$ thin films," *Appl. Phys. Lett.* **83**, 4592-4594 (2003)

9. A. Daniluk, P. Mazurek, K. Paprocki, P. Mikołajczak, "Monte-Carlo simulation of Ge on Si(111) MBE growth: analysis of percolative structure," *Thin Solid Films* **306**, 220-223 (1997).

10. N. Levanov, V. S. Stepanyuk, W. Hergert, O. S. Trushin, K. Kokko, "Molecular dynamics simulation of Co thin films growth on Cu(001)," *Surf. Sci.* **400**, 54-62 (1998).

11. P. J. Dobson, A. Howie, and U. Valdre, *Surface and Interface Characterization by Electron Optical Methods.* Plenum Press: New York (1988).

12. E. G. Gamaly, A. V. Rode, and B. Luther-Davies, "Ultrafast ablation with high-pulse-rate lasers. Part I: Theoretical considerations," *J. Appl. Phys.* **85**, 4213-4221 (1999).

13. Z. Zhang, P. A. VanRompay, J. A. Nees, R. Clarke, R., X. Pan, P. P. Pronko, "Nitride film deposition by femtosecond and nanosecond laser ablation in low-pressure nitrogen discharge gas," *Appl. Surf. Sci.* **154-155**, 165-171 (2000).

14. D. H. Lowndes, D. B. Geohegan, A. A. Puretzky, D. P. Norton, C. M. Rouleau, "Synthesis of Novel Thin-Film Materials by Pulsed Laser Deposition," *Science* **273**, 898-903 (1996).

15. J. E. Mahan, K. M. Geib, G. Y. Robinson, and R. G. Long, "A review of the geometrical fundamentals of reflection high-energy electron diffraction with application to silicon surfaces," *J. Vac. Sci. Technol. A* **8(5)**, 3692-3700 (1990).

16. E. Bauer, *Reflection electron diffraction (RED),* in *Techniques for the direct observation of structure and imperfections,* ed. Bunshah, R. F., *Techniques of metals research,* Vol. **II**, Part 2, 501, Interscience, New York (1969).

17. J. J. Sakurai, *Modern Quantum Mechanics,* Addison and Wesley, New York (1994).

18. J. E. G. Farina, *Quantum theory of scattering processes,* Pergamon Press (1973).

19. J. E. Mahan and K. M. Geib, "A review of the geometrical fundamentals of reflection high-energy electron diffraction with application to silicon surfaces," *J. Vac. Sc. Technol. A.* **8**, 3692-3700 (1990).

20. C. B. Duke, "Semiconductor Surface Reconstruction: The Structural Chemistry of Two-Dimensional Surface Compounds," *Chem. Rev.* **96**, 1237-1260 (1996).

21. (a) W. A. Harrison, "Theory of polar semiconductor surfaces," *J. Vac. Sc. Technol.* **16**, 1492-1497 (1979); (b) W. A. Harrison, "Surface reconstruction," *J. Vac. Sci. Technol.* **14**, 883 (1977).

22. M. D. Pashley and K. W. Haberern, "Compensating surface defects induced by Si doping of GaAs," *Phys. Rev. Lett.* **67**, 2697-2700 (1991).

23. K. Takayanagi, Y. Tanishiro, M. Takahashi, and S. Takahashi, "Structural analysis of Si(111)-7×7 by UHV-transmission electron diffraction and microscopy," *J. Vac. Sci. Technol.* **A3**, 1502-1506 (1985).

24. J. J. Lander and J. Morrison, "Structures of Clean Surfaces of Germanium and Silicon. I," *J. Appl. Phys.* **34**, 1403-1410 (1963).

25. S. Ino, "Some New Techniques in Reflection High Energy Electron Diffraction (RHEED) Application to Surface Structure Studies," *Jpn. J. Appl. Phys.* **16**, 891-908 (1977).

26. R. Seiwatz, "Possible structures for clean, annealed surfaces of germanium and silicon," *Surf. Sci.* **2**, 473-483 (1964).

27. K. Takayangi, Y. Tanishiro, S. Takahashi, and M. Takahashi, "Structure analysis of Si(111)-7×7 reconstructed surface by transmission electron diffraction," *Surf. Sci.* **164**, 367-392 (1985).

28. H. Lüth, "*Surfce and interfaces of sold materials*" 3rd ed. Springer, (1995).

29. M. C. Payne, "An ab initio investigation of the Takayanagi reconstruction," *J. Phys. C.* **20**, L983-L987 (1987).

30. R. Fiedenhans'l, J. S. Pedersen, J. Bohr, M. Nielse, F. Grey, and R. L. Johnson, "Surface structure and long-range order of the Ge(111)-c(2×8) reconstruction," *Phys. Rev. B* **38**, 9715-9720 (1988).

31. S. Kohmoto and A. Ichimiya, "Metastable structure of Si(111) surface during homoepitaxial growth," *Surf. Sci.* **242**, 162-165 (1989).

32 A. W. Denier van der Gon, J. Gay, J. Frenken, and J. van der Veen, "Order-disorder transitions at the Ge(111) surface," *Surf. Sci.* **241**, 335-345 (1991).

33 D. Vanderbilt, "Model for the energetics of Si and Ge (111) surfaces," *Phys. Rev, B.* **36**, 6209-6212 (1987).

34. A. Ichimiya, *"The structure of surface III," Springer Series*, **24**, 162 (1991).

35. H. E. Elsayed-Ali, "Surface Debye temperature measurement with reflection high-energy electron diffraction," *J. Appl. Phys.* **79**, 6853-6857 (1996).

36. C. H. MacGillavry, G. D. Rieck, (Eds.), *International tables for X-ray crystallography,* **III**, Kynoch, Birmingham (1973).

37. David, R. L., *CRC Handbook of Chemistry and Physics*, 89th ed, CRC Press/Taylor and Francis, Boca Raton, FL (2009).

38. Y. Fukaya and Y. Shigeta, "New Phase and Surface Melting of Si(111) at High Temperature above the (7×7)-(1×1) Phase Transition," *Pys. Rev. Lett.,* **85**, 5150-5153 (2000). Y. Fukaya, K. Nakamura, and Y. Shigeta, "Wide range temperature dependence of reflection high-energy electron diffraction rocking curve from a Si(111)7×7 surface," *J. Vac. Sci. Technol. A* **18**, 968-971 (2000).

CHAPTER III

fs-PULSED LASER DEPOSITION

III.1. Introduction

Pulsed laser deposition (PLD) is a growth technique in which photonic energy is coupled to the bulk, causing material to vaporize via thermal or electronic processes.[1,2] An intense laser pulse is passed through a vacuum chamber's optical window and focused onto a solid or liquid surface (target), where it is partially absorbed. Above a certain power density, significant material removal occurs in the form of an ejected luminous plume. The threshold power density needed to produce such a plume depends on the target material, its morphology, and the laser pulse wavelength and duration. Material from the plume is re-condensed on a substrate, where film growth occurs.

Laser deposition for thin film growth has many advantages:

(i) the energy source (laser) is outside the vacuum chamber, which provides a greater degree of flexibility in materials use and geometrical arrangements;

(ii) almost any condensed material can be ablated;

(iii) the pulsed nature of PLD means that film growth rates can be controlled to any desired amount;

(iv) the amount of evaporated source material is localized only to that area defined by the laser focus;

(v) under optimal conditions, the ratios of the elemental components of the bulk and film are the same, even for chemically complex systems (stoichemetric process);

(vi) the kinetic energies of the ablated species lie mainly in a range that promotes surface mobility while avoiding bulk displacements; and

(vii) the ability to produce species with electronic states far from chemical equilibrium opens up the potential to produce metastable materials that would be unattainable under thermal conditions.[3,4]

PLD has also technical and fundamental disadvantages, in particular:

(i) the production of macroscopic eject during the ablation process;

(ii) impurities in the target material;

(iii) crystallographic defects in the film caused by bombardment by high kinetic energy ablation particles; and

(iv) inhomogeneous flux and angular energy distributions within the ablation plume.

In the present work, homoepitaxial growth of Si on Si(111)-7x7 thin film deposited by PLD was around 210 °C where the deposition by MBE reported to be at 525 °C using gas source MBE.[1,2]

III.2. PLD Characteristics

There are some characteristics that distinguish the PLD from the other thin film growth techniques. These characteristics affect either the intrinsic film properties, like

particle kinetic energy distribution, deposition rate, and flux stoichiometry, or the film thickness uniformity, such as flux angular distribution and particulate deposition.[5-7]

i) Particle kinetic energy distributions

Typically, particle kinetic energies which increase with increasing laser fluence[8-10] are much higher than those associated with thermal or electron beam evaporation. In PLD, the energetic flux has an impact on the properties of films produced. For example, the single crystal Ge film deposited by PLD at 300 °C is comparable with those deposited by molecular beam epitaxy (MBE) on atomically clean substrate at 350 °C. This result is attributed to the enhancement of initial nucleation by enhancing the energetic plume species.[11]

ii) Peak deposition rates

Flight times are determined by the particle velocity distributions as well as by the deposition rate. The range of flight times (resulting from the spread in the velocity distribution) defines the time interval over which the particles are deposited. This time interval Δt can be approximated by $(h/\nu_{mp})(\Delta\nu_{FWHM}/\nu_{mp})$, where h is the target to substrate distance, ν_{mp} is the most probable particle velocity, and $\Delta\nu_{FWHM}$ is the width of the velocity distribution. Figure 3.1. illustrates how the on-axis deposition rate varies as a function of time for various target-substrate distance for a flux time-of-flight (TOF) distribution of the form $F(t) = At^{-5}e^{-(\frac{m}{2kt})*(\frac{h}{t})^2}$ where t is the TOF, A is a normalization constant, k is the Boltzmann constant, T is the temperature, and m is the particle mass.[13]

iii) Flux angular distribution and Plume Direction

Plumes generated by a short pulse length ($\tau \leq 30$ ns) laser are usually oriented along the target surface normal,[14] even for non-normal laser angles of incidence.[15] However, the plume axis has been observed to tilt from the target surface normal both towards and away from the direction of the incident laser beam. Asymmetries of the plume have been attributed to the presence of large mass clusters. Plume tilting may also arise if the laser beam on the target is asymmetric and/or non-uniform.[16,17]

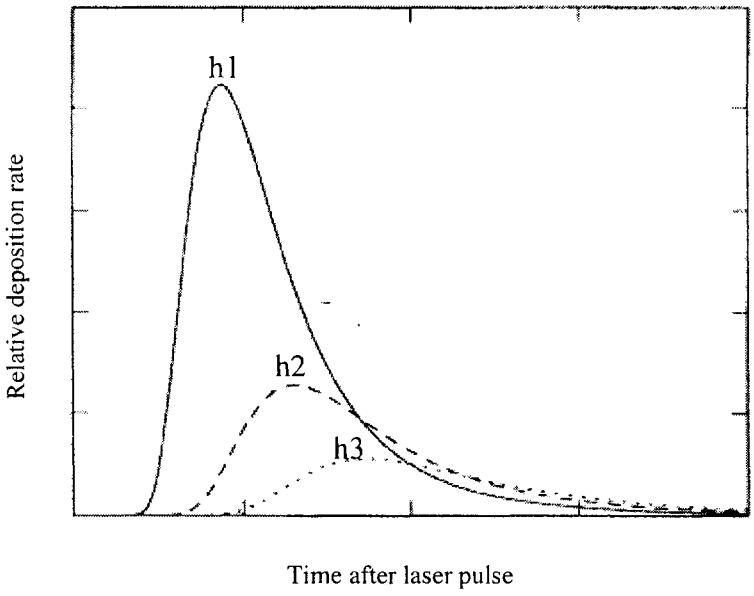

FIG. 3.1. On axis deposition rates as a function of time after the laser pulse for target substrate distances h1<h2<h3. The flux and deposition rate are described by $F(t)=At^{-5}\, e^{-(m/2kT)(h/t)^2}$ [after ref 16].

iv) Stoichiometry of removal species

One of the most important features of the PLD is that the flux material from the target often matches the target stoichiometry. Due to the fast heating rate

of the deposition, the material removal occurs before the individual components of the target can segregate into different vapor pressure components.[16]

v) Particulates

Particles with dimensions ranging from sub-micrometer to several micrometers (molten droplets) can be released from pulsed laser irradiation of the target. In Si, both crystalline and amorphous particulates have been observed.[18] Particulates dramatically affect the surface morphology of the produced films. Films with high particle content have a rough surface.[17]

vi) Particulate reduction

Some techniques have been investigated for reducing film particulate content. These techniques can be summarized, as shown in Fig. 3.2, by using the following:

1. Molten targets to ensure smooth, crater-free, self-heating surface.
2. Electrostatic deflectors to reduce particle content of the film, implying that most of the particulates are charged.[16]
3. Mechanical chopping to filter out the low speed particulates.[19]
4. Second pulse laser to vaporize the in-flight particulates.[17]
5. Heated screen to reflect the non-particulate flux onto substrate.[20]
6. Gasdynamic separation process, where two laser-generated plumes from separate targets are intersected. The light species are redirected onto the

substrate by momentum-changing collisions, while the heavy parties retain their initial velocity and miss the substrate.[20]

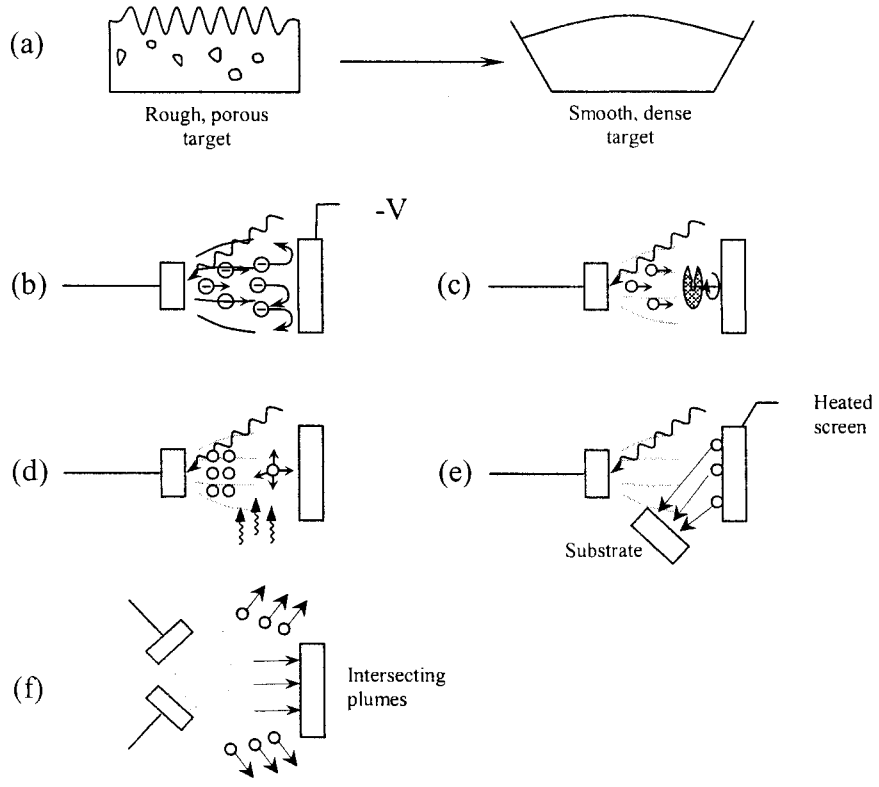

FIG. 3.2. Particulate reduction techniques, (a) molten target; (b) electrostatic deflectors; (c) mechanical chopper; (d) in-flight vaporization; (e) reflector heating screen; (f) gasdynamic separation.

III.3. Nature of the Laser Ablation

Materials ablation by lasers falls on a continuum between two extremes: thermal and non-thermal ablations. In thermal ablation, where the laser energy exceeds the energy damage threshold, laser photons are absorbed and the resulting heat melts and vaporizes the material. For metal targets, laser absorption by free electrons takes place via an inverse Bremsstrahlung mechanism. Thermalization of these hot electrons takes place through (i) heat transport into the bulk by thermal diffusion and (ii) electron-phonon coupling by transferring their energy to the lattice. The main parameters of interest in such absorption mechanism are the peak surface temperature and the volume of the heated region, which are governed by the optical properties (reflectivity, R, and absorption coefficient, α) and the thermal properties of the target (specific heat, C, the vaporization energy, and thermal conductivity, K) and the laser peak intensity, I_p. The rise in the substrate temperature, ΔT, is calculated from the heat diffusion equation:

$$\rho C \frac{\Delta T(z,t)}{\Delta t} = K \frac{\Delta T(z_0 + \Delta z) - \Delta T(z_0)}{(\Delta z)^2} + (1-R)\alpha I_p \exp[-\alpha z].\exp[-\frac{t^2}{\tau^2}], \tag{3.1}$$

with

$$\tau = \frac{\tau_{FWHM}}{\sqrt{(4 * \log(2)}}, \tag{3.2}$$

where τ_{FWHM} is the FWHM of the laser pulse. Ablation takes place when the laser energy dumped into the system exceeds a certain threshold to melt and vaporize the target.

On the other hand, non-thermal ablation takes place by a variety of ways, depending on the properties of the laser and those of the substrate. Examples of the non-thermal ablation processes are:

(1) Desorption induced by electronic transitions (DIET): Photon absorption takes place by valance electrons, which causes their excitation into anti-bonding states. This results in the emission of atoms, molecules and ions.[21,22]

(2) Collisional sputtering: This is an indirect process, in which plasma formed by laser interaction with matter bombards and sputters the surface of the material [23].

(3) Hydrodynamic sputtering: In this process, the target's surface is melted by the laser energy, forming small droplets. Pressure waves, due to motion of the liquid in the surface, result in the ejection of such droplets from the surface.[24,25]

(4) Fracto-emission: In this case, particles are emitted from freshly fractured surfaces by thermal or mechanical stresses.[26]

The important parameters determining the effect of the laser pulse length on the ablation process include: the heat diffusivity of the material, velocity of sound, and the time scale for electron-electron thermalization and electron-phonon coupling, which was shown to be on the order of ~1 picosecond.[27] The important thermal processes, which occur in laser ablation, have been shown to be greatly modified once the laser pulses are shortened to a picosecond or femtosecond time scale.[28,29] Due to their better spatial concentration compared to ns pulses, ultrashort (ps and fs) laser pulses decrease the required laser (threshold) fluence for ablation, increase the thermal gradient in the target, decrease the amount of energy lost to plasma, and increase energy coupling to vaporize

rather than melt the target. A time-resolved microscopic study showed that the actual ablation by ultrashort lasers takes much longer than the thermalization of the absorbed laser energy.[37] The same study showed that ablation of metals and semiconductors by ps and fs laser pulses occur on the nanosecond time scale.[30]

It is commonly assumed that the ablation process near the threshold is always initiated by the ultrafast melting of the material. However, a recent study on femtosecond laser ablation of silicon reported the occurrence of several physical processes, depending on the laser fluence.[31] These are, arranged in ascendant laser fluence order, oxidation, amorphization, re-crystallization, formation of bubbles due to boiling below the surface, and ablation.[31] Another study on the physics of the fs laser ablation of wide band-gap materials reported two different ablation phases: a gentle phase with low ablation rates and a strong (etch) phase characterized by higher ablation rates but accompanied by a reduction of the degree of ionization.[32]

III.3.A. Plume characteristics

Exploring the nature of the plume and its dependence on the properties of the ablating laser is important for understanding how one can control the growth of thin films by using PLD. Extensive theoretical and experimental work is being performed in order to study all of the plume's characteristics. Among these important characteristics are:

i) Plume expansion: This refers to the spatial expansion of the ablated species as a function of time. It is found to depend on the parameters of the ablating laser (wavelength, pulse width and fluence),[33] target material and ambient pressure.

It was shown that fs-lasers result in plumes of less lateral expansion (or more forward-directed) than those generated by the ns lasers.[34] However, increasing the laser fluence results in sharpening the plume which is due to the interaction between the ablated particles.[35] Another interesting study showed that the plume sharpness increases with the target's atomic mass.[36] The plume angular dependence was shown to have the form

$$\frac{dN}{d\Omega} = a\cos\phi + b\cos^n\phi \tag{2.3}$$

when a, b, and n are material dependents, leading to film thickness variation of the form $\cos^n\theta$ with $n = 3k^2$.[36,37]

ii) Energy (velocity) distributions: It is understood that the ablated species are emitted with very high kinetic energies, ranging between 0.1-1000 eV. Each of the emitted species has its own energy (or velocity) distribution. Such distributions depend on the laser's fluence and pulse width as well as the target material itself. Ablation by femtosecond pulses results in the ejection of highly energetic particles, with velocities that can be an order of magnitude higher than those ablated in the nanosecond regime.[34] As for the laser fluence, its increase results in the increase of the ablated particles' mean velocities.[38]. Depending on the laser fluence, the composition of the plume changes significantly, since it can contain fine clusters when the applied laser fluence is much higher than the ablation threshold. Furthermore, depending on the composition and density of the plume, the velocity distribution can be described by a one-temperature shifted Maxwell–Boltzmann function or a two-temperature (parallel and perpendicular) distribution.[39]

iii) Effect of background (ambient) gas: The velocities of the ablated species and the expansion dynamics strongly depend on the type and pressure of the background gas.[34,40] For example, the width of the angular distribution of Ag ions increases with the Ar background pressure. In a He background however, the plume first narrows for a certain pressure range before it widens for higher pressures.[40] Also, the length of the plume shortens when the ambient pressure increases.[41]

III.3.B. Particulates formation

The three mechanisms for forming particulates are splashing, recoil pressure, and fracto-emission. In splashing, a thin layer of the surface superheats above the vaporization temperature and a molten overlayer is blown off and disintegrates into liquid droplets.[42-44] However, in recoil pressure, vaporized materials exert pressure on the molten layer, which is formed by laser irradiation and, as a result, liquid droplets are ejected.[45] Lastly, fracto-emission is the process in which emission from the microcracks in the target is caused by laser-induced thermal shocks.[40]

Some mechanical filters have been used to prevent particulates from reaching the substrate; however, none of them could be considered as a universal solution for such a problem. Particulates formation is affected by a number of parameters:

(1) Target density: increasing the target density can minimize the formation of particulates.[46]

(2) Laser pulse duration and repetition rate: using ultrashort (fs and ps) lasers minimizes or eliminates their formation due to the lower thermal losses compared to the ns pulses, which causes smaller amounts of molten material and liquid droplets in the plume.[47-49]

(3) Target surface quality: the probability of emission from rough surfaces is quite high. Therefore, using rotated polished targets minimizes the particulates formation by expositing fresh target areas to the laser all the time.

(4) Laser wavelength: YBC and BiSrCaCuO films deposited with 1.064 μm were rough, in contrast to the smoother ones deposited with UV wavelengths.[50] However, the wavelength that yields the best film morphology depends on the target material.

(5) Laser fluence: generally the particulates formation increases with the laser fluence. Particulate-free $CaZrO_3$ films were prepared by 0.64 J/cm^2 fluence, while SEM showed some particulates for those prepared with the same laser but with 16 J/cm^2 fluence.[51]

III.4. fs-Pulsed laser deposition system

The experiment was performed in a UHV chamber equipped with a RHEED system. The residual gas pressure was $5x10^{-10}$ torr and the electron beam energy was kept at 8.6 keV. The investigated sample was a p-type Si(111) wafer with electrical resistivity between 20 and 50 Ωcm and sample dimensions 5x3x0.4 mm.

III.4.A. Experimental setup

The ultrahigh vacuum chamber was equipped with turbo-molecular and ion pumps. A pressure of ~ 5×10^{-9} Torr can be reached without backing. If the system is backed, a base pressure of < 1×10^{-10} Torr could be reached. A convectron (reading from 760 Torr down to 1×10^{-3} Torr) and an ion gauge (measuring from 1×10^{-3} Torr down to 1×10^{-11} Torr) are used to monitor the pressure at the different pressure ranges. A "homemade" sample holder, which is used to mount the substrate, was designed to heat the sample by means of direct heating, so that very high temperatures could be easily reached. The substrate holder is mounted on a manipulator (on a 4.5-inch conflat flange), which enables the azimuthial rotation of the sample by 360° and the adjustment of the sample-target distance. The target is mounted on an electrically rotated sample holder with a variable rotation speed. The rotation of the target minimizes the formation of particulates by exposing a fresh area to the laser all the time; thus, the probability of fracto-emission is minimized. The system is designed so that the laser, which enters the system through a 2.5 inch sapphire window, hits the target at ~45°. To monitor the deposition, a CW-electron gun operated at 8.6 keV is used. An 8 inch phosphor screen is used to show the electron diffraction pattern, which is recorded by a CCD camera and later analyzed by image analysis software.

The homoepitaxial growth of Si on Si(111)-7x7 is performed on this system as shown in Fig. 3.3. The energy of the fs laser is set to the desired value, using a half wave plate, a polarizer and a neutral density (ND) filter. Then, it is focused on a mechanically rotated Si target and its position on the target is adjusted while a mechanical shutter is hiding the sample from the plume. Meanwhile, the sample is heated to the desired

temperature. The focused laser beam on the target is elliptic in shape, with major and minor diameters of ~270 μm and ~160 μm, respectively (both measured at 1/e of the peak maximum). Movies of the RHEED pattern are recorded during PLD using a CCD camera. The recorded movies are later analyzed by studying the change of the intensity and the shape of the RHEED pattern with deposition time.

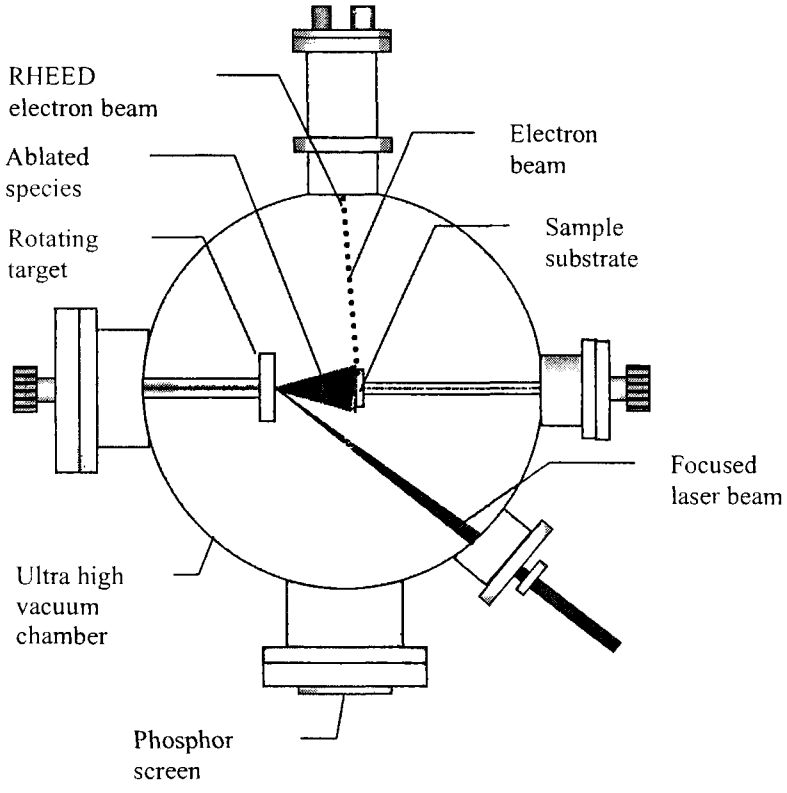

FIG. 3.3. Pulsed laser deposition setup. An UHV chamber equipped with a RHEED system. A 100 femtosecond Ti-Sapphire laser was used to ablate Si target. The residual gas pressure was better than $5x10^{-9}$ torr and the electron beam energy was kept at 8.6 keV.

III.4.B. Sample preparation

A clear 7x7 RHEED pattern was observed after *ex-situ* chemical cleaning using modified Shiraki method,[52] and *in-situ* heating to ~1200 °C for up to 2 min then cooling slowly (~2 °C/s) between 1000 °C and 800 °C to ensure a good and clear 7x7 reconstruction. The sample's temperature was measured using a Pt/PtRh(10%) thermocouple pressed against the surface of the sample with an error of ±2 °C accuracy. High-energy electrons were incident with a glancing angle less than 4° onto the sample's surface, and the diffracted beams were observed on a fluorescent screen. At the screen, a typical RHEED image consisting of bright spots against a diffuse background appears. The arrangement of these bright spots is related to the arrangement of atoms at the surface, as shown in Fig. 3.4.

FIG. 3.4. Si(111) with the 7x7 reconstruction RHEED patterns along (a) $[\bar{1}2\bar{1}]$ and (b) $[01\bar{1}]$ incidence at electron energy 8.6 keV. A clean sample was prepared for PLD.

III.5. Effect of substrate temperature on Si(111)-7x7 homoepitaxy

A Ti-Sapphire laser (100 fs, 800 nm, 1 kHz) was used to ablate the Si target on Si(111)-7x7 substrate at different temperatures, while real-time movies for RHEED pattern during deposition were recorded. Fig. 6(a) and Fig. 6(b) show the decay of the intensity of a specular spot, as a function of deposition time at different temperatures (210 °C to 920 °C). The decay of the RHEED pattern during deposition was due to increasing the surface roughness. The films showing no change in RHEED patterns indicated step-flow growth.

The growth mechanisms can be divided into three different regimes.

1) Growth at substrate temperature below 210 °C. In this case, the sample was pumped by a laser with a fluence of 300 mJ/cm^2 and substrate temperature between room temperature and 210 °C. The intensity of the RHEED pattern for all spots during deposition until the pattern completely disappears is shown in Fig. 3.5(a). Figure 3.5(b) shows a decay of the intensity of the (00) spot as a function of deposition time. The disappearance of the RHEED pattern during deposition is explained as an increase of the surface roughness.
2) The second regime starts above ~210 °C to the transition temperature (830 °C) of reconstructed Si(111). In this case, the diffraction pattern decays during deposition and recovers after the deposition stops, indicating a step-flow growth as shown in Fig. 3.5(b) for the (00) spot. However, the intensity of the $(0\frac{4}{7})$ reconstructed spot does not completely decay; therefore, it is more useful to monitor the change of the intensity as a function of time for this

reconstructed spot. The intensity increases back after the deposition stops. The region is characterized by the recovery of all the 7x7 spots indicating a step flow growth.

3) The third regime is when the deposition temperature is higher than the surface transition temperature (~830 °C). The RHEED patterns show a recovery of all $(\text{“1x1”})_h$ spots only, with the disappearance of all the reconstructed spots as expected.

In conclusion, there is not any epitaxial growth below the 210°C, and the step-flow epitaxial growth is noticed between the 210 °C and 830 °C; in addition, the step-flow growth is noticed for the Si(111)-$(1x1)_h$ above the transition temperature (> 830 °C). In Fig. 3.6(a), the RHEED pattern shows a step-flow growth for homoepiatxial growth of Si on Si(111)-7x7 at 210 °C. Also, the intensity of the $(0\frac{1}{7})$, $(0\frac{2}{7})$, and $(0\frac{4}{7})$ spots decrease during the deposition but do not completely disappear as shown in RHEED line scan in Fig. 3.6(b).

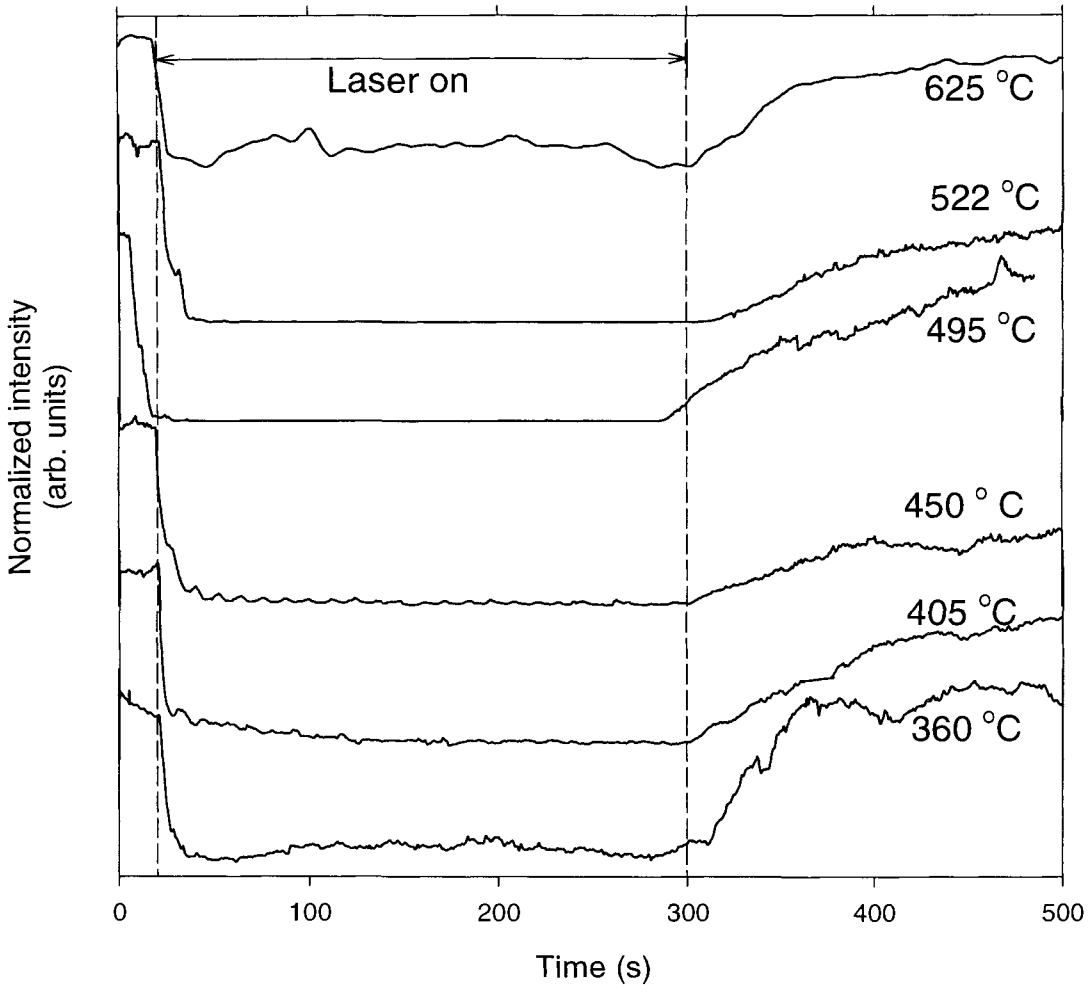

FIG. 3.5(a). Temperature dependence of RHEED intensity for Si/Si(111) at substrate temperature between 360-625 °C. The detector was placed at an incident angle 1.39° to specular spot using 8.6 keV electrons in the $[\bar{1}2\bar{1}]$ azimuth direction. Laser beam was kept at constant fluence of 300 mJ/cm^2 at base pressure better than 1x10^{-8} torr.

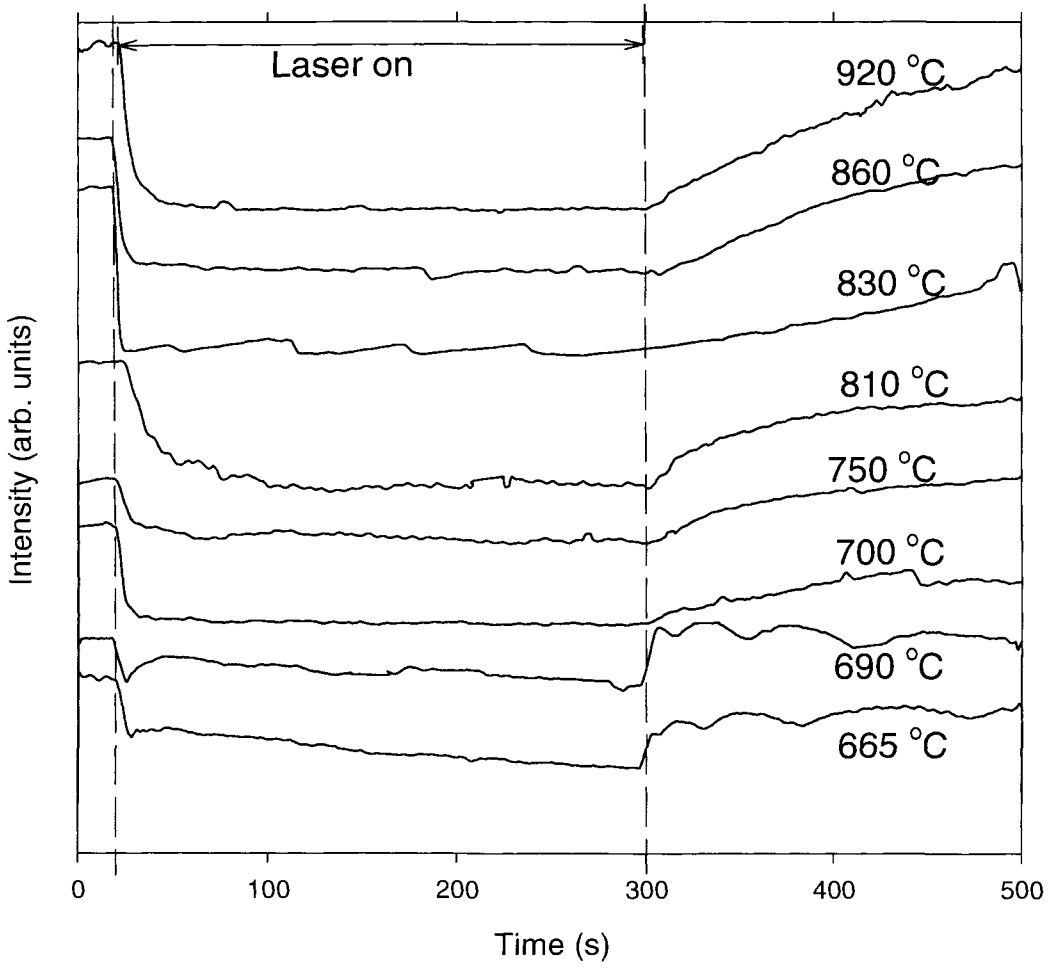

FIG. 3.5(b). Temperature dependence of RHEED intensity for Si/Si(111) at substrate temperature between 665-920 °C. The detector was placed at an incident angle 1.39° to specular spot using 8.6 keV electrons in the $[\bar{1}2\bar{1}]$ azimuth direction. Laser beam was kept at constant fluence of 300 mJ/cm^2 at base pressure better than 1x10^{-8} torr

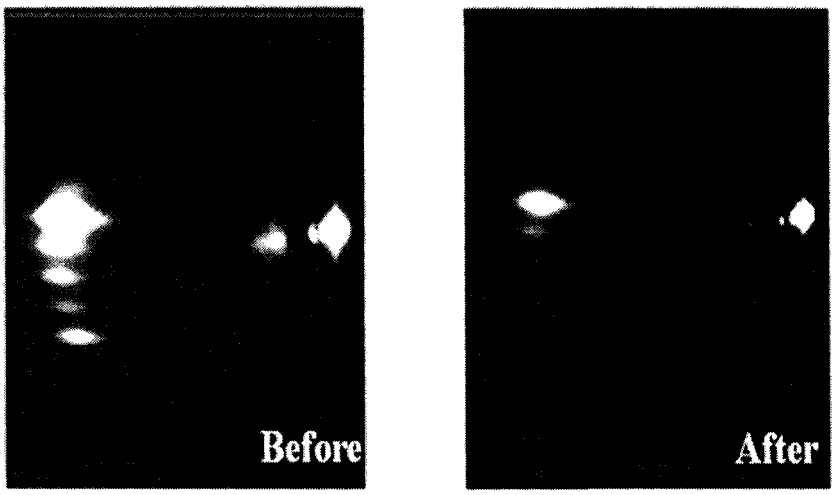

FIG.3.6(a). RHEED observation for homoepitaxial growth for Si on Si(111)-7x7 at 210 °C. Both specular and reconstructed spots are present; the laser beam fluence was kept at 300 mJ/cm^2.

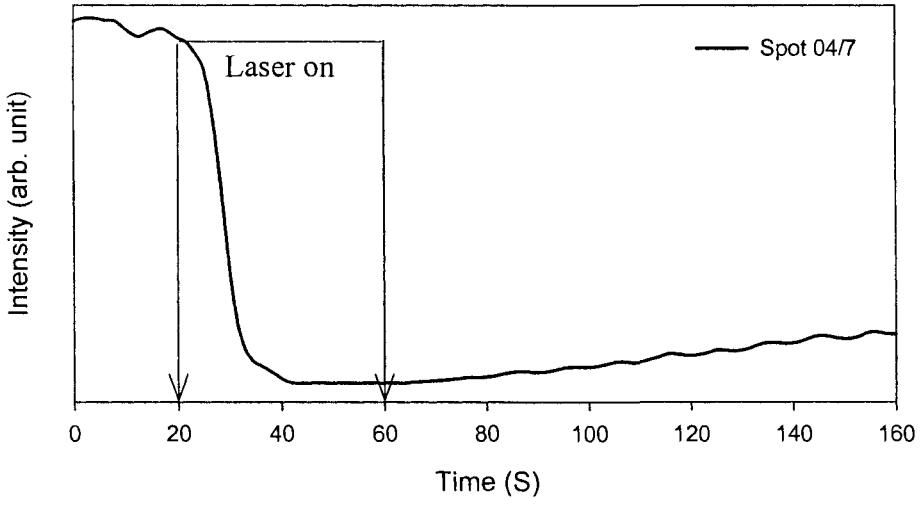

FIG. 3.6(b). Normalized RHEED intensity for Si(111)-7x7 at 210 °C. Laser beam was kept at constant fluence of 300 mJ/cm^2 at base pressure better than 1x10^{-8} torr after deposit ~ 10 ML.

III.6. Effect of substrate temperature on the island density size

Since its invention by Binnig *et al.*,[53] atomic force microscopy (AFM) has been established as a powerful method for the study of topographies on crystal surfaces. In the present work, we use an atomic force microscope, operated in non-contact mode (NC-AFM), to study the effect of temperature on the crystallite (density, shape, and size of the droplets) on the atomic scale. The AFM has been used to investigate surface structures of homoepitaxial growth of Si(111)-7x7 as well as the temperature effect on the crystallite by measuring the density, number, and average size of the droplets.[54-56] The measurements were done using a NC-AFM DI model nanoscope. As shown in Fig. 3.7. and Fig. 3.8., increasing the temperature substrate decreases the number of clusters and increases the cluster average size.

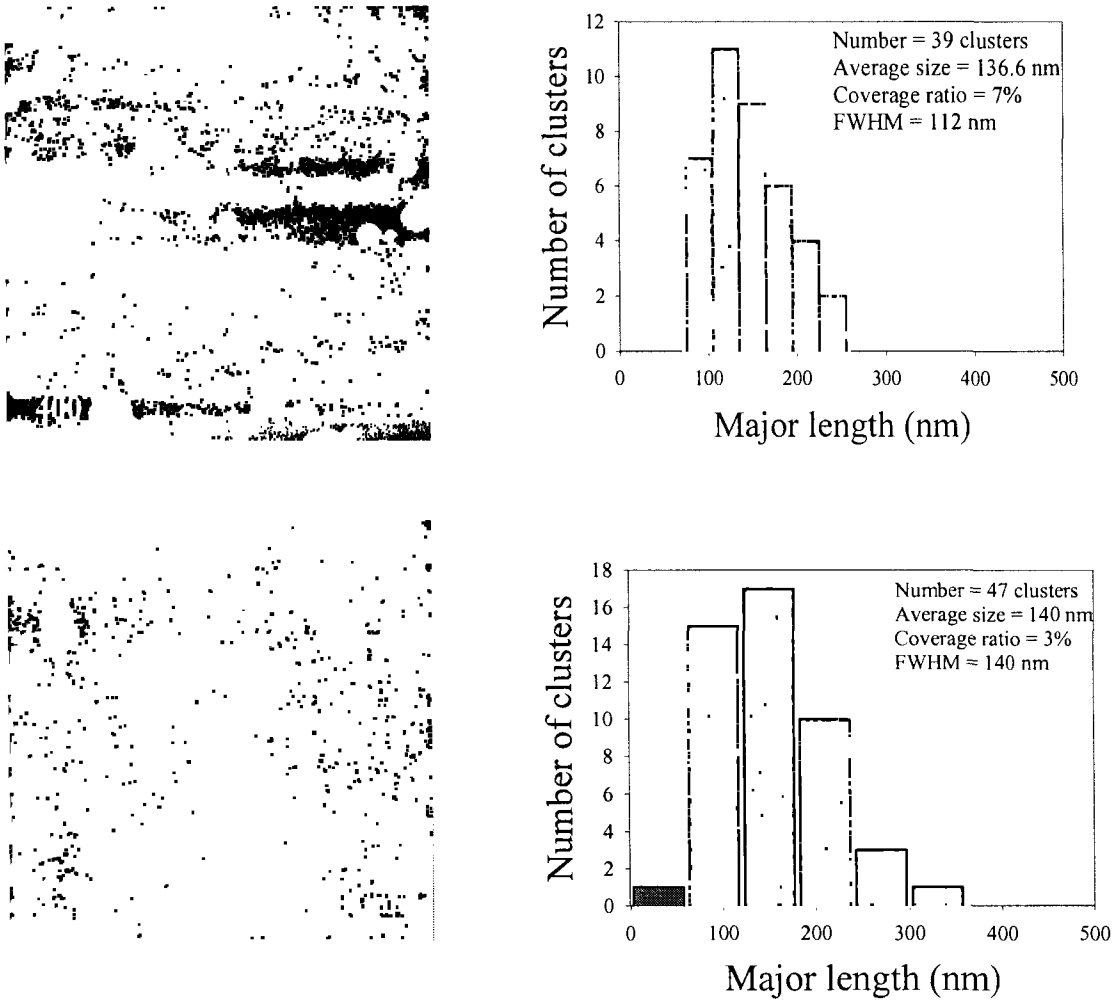

FIG. 3.7. AFM Micrograph of Si/Si(111)-7x7 at different substrate temperature, laser fluence was 0.3 J/cm^2, after depositing 20 ML..

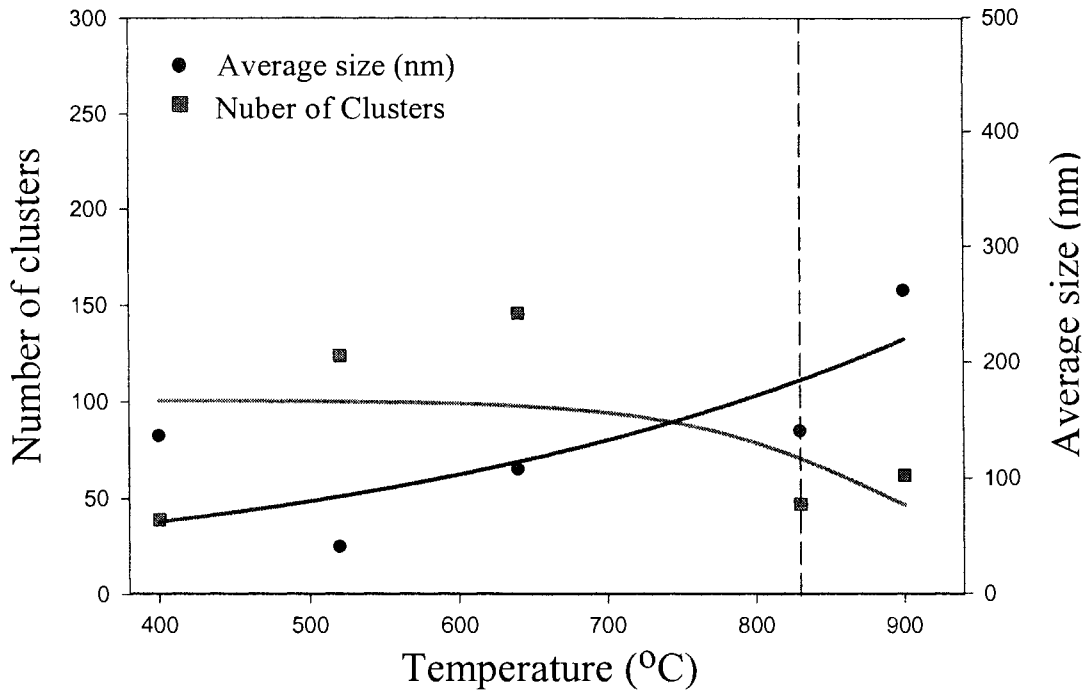

FIG. 3.8. Number of clusters, and cluster average size are temperature dependent

III.7. Conclusion:

In this part, we report that the minimum temperature for homoepitaxial growth to be ~210 °C, for 70 ML films at a growth rate of ~ 0.3 ML/s. In the low temperature range the growth is essentially amorphous, and in the high temperature range until the transition temperature a step flow growth for 7x7 phase becomes dominant. Above the transition temperature the step flow growth on $(1x1)_h$ becomes dominant. By measuring the density, the shape, and the size of the clusters on the atomic scale with different temperatures, it is found that increasing the temperature substrate decreases the number of clusters and increases the cluster average size.

III.8. References

1. P. R. Willmott and J. R. Huber, "Pulsed laser vaporization and deposition," *Rev. Mod. Phy.* **72**, 315-328 (2000).
2. D. B. Chrisey and G. K. Hubler, *Pulsed Laser Deposition of Thin Films*, Wiley, New York (1994).
3. D. Dijkkamp, T. Venkatesan, X. D. Wu, S. A. Shaheen, N. Jisrwi, Y. Min-Lee, W. L. McLean, and M. Croft, "Preparation of Y-Ba-Cu oxide superconductor thin films using pulsed laser evaporation from high Tc bulk material" *Appl. Phys. Lett.* **51**, 619-621 (1987).
4. X. D. Wu, A. Inam, T. Venkatesan, C. C. Chang, E. W. Chase, P. Barboux, J. M. Tarascon, and B. Wilkens, "Low-temperature preparation of high T_c superconducting thin films," *Appl. Phys. Lett.* **52**, pp.754-756 (1988).
5. H. Tabata, O. Murata, T. Kawai, and S. Kawai, "Superlattices of Y-Ba-Cu-O/Yy-Pr1−y-Ba-Cu-O grown by pulsed laser deposition ," *Appl. Phys. Lett.* **56**, 400-402 (1990).
6. H. Sankur, J. DeNatale, W. Gunning, and J. G. Nelson, "Dense crystalline ZrO2 thin films deposited by pulsed-laser evaporation," *J. Vac. Sci. Tech. A* **5**, 2869-2874 (1987).
7 R. A. Neifeld, E. Potenziani, W. R. Sinclair, W. T. Hill III, B. Turner, and A. Pinkas, "Properties of the ablation process for excimer laser ablation of Y1Ba2Cu3O7," *J. Appl. Phys.* **69**, 1107-1109 (1991).
8. P. D. Brewer, J. J. Zinck, and G. L. Olson, "Reversible modification of CdTe surface composition by excimer laser irradiation," *Appl. Phys. Lett.* **57**, 2526-2528 (1990).

9. J. T. Cheung and H. Sankur, *CRC Crit. Rev. of Sol. St. Mater. Sci.* **15**, 63 (1988).

10. H. Okumura, T. Ishikawa, T. Akane, M. Sano, and S. Matsumoto, "Low temperature growth of Si on Si(111) by gas-source MBE with rapid thermal annealing: AFM study on surface morphology," *Appl. Sur. Sci.* **135**, 121-128 (1998).

11. R. Kelly and R. W. Dreyfus, "On the effect of Knudsen-layer formation on studies of vaporization, sputtering, and desorption," *Surf. Sci.* **198**, 263-276 (1988).

12. Lubben, D., Barnett, S. A., Suzuki, K., Gorbatkin, S., and Greene, J. E., "Laser-induced plasmas for primary ion deposition of epitaxial Ge and Si films," *J. Vac. Sci. Tech B* **3**, 968-974 (1085).

13. V. Venkatesan, X. D. Wu, A. Inam, and J. B. Wachtman, "Observation of two distinct components during pulsed laser deposition of high Tc superconducting films," *Appl. Phys. Lett.* **52**, 1193-1195 (1988).

14. R. A. Neifeld, S. Gunapala, C. Liang, S. A. Shaheen, S. A. Croft, J. Price, D. Simons, D., and W. T. Hill, "Systematics of thin films formed by excimer laser ablation: Results on SmBa2Cu3O7," *Appl. Phys. Lett.* **53**, 703-704 (1988).

15. K. L. Saenger, *Process. Adv. Mater.* **2**, 1 (1992); K. L. Saenger, *Process. Adv. Mater.* **3**, 63 (1993).

16. J. A. Greer and H. J. Van Hook, *Mater. Res. Soc. Sym. Proc.* **38**, 325 (1985).

17. O. Auciello, S. Athavale, O. E. Hankins, M. Sito, A. F. Schreiner, and N. Biunno, N., "Spectroscopic analysis of electronically excited species in XeCl excimer laser-induced plasmas from the ablated high-temperature superconductor YBa2Cu3O7," *Appl. Phys. Lett.* **53**, 72-74 (1988).

18. R. W. Dreyfus, "Cu0, Cu+, and Cu2 from excimer-ablated copper," *J. Appl. Phys.* **69**, 1721-1729 (1991).

19. R. Kelly, "On the dual role of the Knudsen layer and unsteady, adiabatic expansion in pulse sputtering phenomena," *J. Chem. Phys.* **92**, 5047-5056 (1990).

20. R. E. Muenchausen, K. M. Hubbard, S. Foltyn, R. C. Estler, N. S. Nogar, and C. Jenkins, "Effects of beam parameters on excimer laser deposition of YBa2Cu3O7−δ," *Appl. Phys. Lett.* **56**, 578-580 (1990).

21. J. Kanasaki, N. Mikasa, and K. Tanimura, "Laser-induced electronic desorption from InP surfaces studied by femtosecond nonresonant ionization spectroscopy," *Phys. Rev. B.* **64**, 035414-10 (2001).

22. P. Avouris and R. E. Walkup, "Fundamental Mechanisms of Desorption and Fragmentation Induced by Electronic Transitions at Surfaces," *Ann. Rev. Phys. Chem.* **40**, 173-206 (1989).

23. G. Falcone, "Ejection process in collisional sputtering," *Phys. Rev. B* **33**, 5054-5056 (1986).

24. R. Kelly, J. J. Cuomo, P. A. Leary, J. E. Rothenberg, B. E. Braren, and C. F. Aliotta, "Laser sputtering: Part I. On the existence of rapid laser sputtering at 193 nm," *Nucl. Inst. Meth. B* **9**, 329-340 (1985).

25. R. Kelly and A. Miotello, *Mechanisms of Pulsed Laser Sputtering in Pulsed Laser Deposition of Thin Films,* D. B. Chrisey and G. K. Hubler (editors), John Wiley & Sons Inc., New York, (1994).

26. E. E. Donaldson, J. T. Dickinson and S. K. Bhattacharya, "production and properties of ejecta released by fracture of materials," *J. Adhesion* **25**, 281-302 (1988).

27. H. E. Elsayed-Ali, T. B. Norris, M. A. Pessot, and G. Mourou, "Time-resolved observation of electron-phonon relaxation in copper," *Phys. Rev. Lett.* **58**, 1212-1215 (1987).

28. P. P. Pronko, S. K. Dutta, D. Du, and R. K. Singh, "Thermophysical effects in laser processing of materials with picosecond and femtosecond pulses," *J. Appl. Phys.* **78**, 6233-6240 (1995).

29. P. P. Pronko, P. A. Van Rompay, and S. Sato, "Thin film synthesis with ultrafast lasers," *Proc. SPIE- Intrational Society for Optical Engineering* **3269**, 46-56 (1998).

30. D. von der Linde and K. Sokolowski-Tinten, "Self-organized growth of semiconductor nanostructures for novel light emitters," *Appl. Surf. Sci.* **154-155**, 1-7 (2000).

31. J. Bonse, S. Baudach, J. Krüger, W. Kautek, and M. Lenzner, "Femtosecond laser ablation of silicon–modification thresholds and morphology," *Appl. Phys. A* **74**, 19-25 (2002).

32. I. V. Hertel, R. Stoian, D. Ashkenasi, A. Rosenfeld, and E. B. Campbell, "On the physics of material processing with femtosecond lasers," *Riken Review* **32**, 23-30 (2001).

33. M. W. Stapleton, A. P. McKiernan, and J. -P. Mosnier, "Expansion dynamics and equilibrium conditions in a laser ablation plume of lithium: Modeling and experiment," *J. Appl. Phys.* **97**, 064904-12 (2005).

34. J. Perrière, E. Millon, W. Seiler, C. Boulmer-Leborgne, V. Craciun, V., O. Albert, J. C. Loulergue, and J. Etchepare, "Comparison between ZnO films grown by femtosecond and nanosecond laser ablation," *J. Appl. Phys.* **91**, 690-696 (2002).

35. N. N. Nedialkov, P. A. Atanasov, S. E. Imamova, A. Ruf, P. Berger, and F. Dausinger, "Dynamics of the ejected material in ultra-short laser ablation of metals," *Appl. Phys. A* **79**, 1121-1125 (2004).

36. E. Buttini, A. Thum-Jäger, and K. Rohr, "The mass dependence of the jet formation in laser-produced particle beams," *J. Phys. D: Appl. Phys.* **31**, 2165–2169 (1998).

37 S. I. Anisimov, D. Bäuerle, B. S. Luk'yanchuck, "Gas dynamics and film profiles in pulsed-laser deposition of materials," *Phys. Rev. B* **48**, 12076-12081 (1993).

38. M. Ye and C. P. Grigoropoulos, "Time-of-flight and emission spectroscopy study of femtosecond laser ablation of titanium," *J. Appl. Phys.* **89**, 5183-5190 (2001).

39. M. Zeifman, B. Garrison, and L. V. Zhigilei, "Combined molecular dynamics–direct simulation Monte Carlo computational study of laser ablation plume evolution," *J. Appl. Phys.* **92**, 2181-2193 (2002).

40. S. Amoruso, B. Toftmann, and J. Schou, "Expansion of a laser-produced silver plume in light background gases," *Appl. Phys. A* **79**, 1311-1314 (2004).

41. Z. Chen, D. Bleiner, and A. Bogaerts, "Effect of ambient pressure on laser ablation and plume expansion dynamics: A numerical simulation," *J. Appl. Phys.* **99**, 063304 1-9 (2006).

42. J. Ready, "Development of plume of material vaporized by giant-pulse laser," *Appl. Phys. Lett.* **3**, 11-13(1963).

43. R. K. Singh, D. Bhattacharya, and J. Narayan, "Subsurface heating effects during pulsed laser evaporation of materials," *Appl. Phys. Lett.* **57**, 2022-2024 (1990).

44. D. Bhattacharya, R. K. Singh, and P. H. Holloway, "Laser-target interactions during pulsed laser deposition of superconducting thin films," *J. Appl. Phys.* **70**, 5433-5439 (1991).

45. H. Dupendant, J. P. Gavigan, D. Givord, A. Lienard, J. P. Rebouillat, and Y. Souche, "Velocity distribution of micron-size particles in thin film laser ablation deposition (LAD) of metals and oxide superconductors," *Appl. Surf. Sci.* **43**, 369-376 (1989).

46. S. J. Barrington, T. Bhutta, D. P. Shepherd, R. W. Eason, "The effect of particulate density on performance of Nd:$Gd_3Ga_5O_{12}$ waveguide lasers grown by pulsed laser deposition," *Opt. Comm.* **185**, 145-152 (2000).

47. F. Qian, R. K. Singh, S. K. Dutta, and P. P. Pronko, "Laser deposition of diamondlike carbon films at high intensities," *Appl. Phys. Lett.* **67**, 3120-3122 (1995).

48. E. G. Gamaly, A. V. Rode, and B. Luther-Davies, "Ultrafast ablation with high-pulse-rate lasers. Part I: Theoretical considerations," *J. Appl. Phys.* **85**, 4213-4221 (1999).

49. E. G. Gamaly, A. V. Rode, and B. Luther-Davies, "Ultrafast ablation with high-pulse-rate lasers. Part II: Experiments on laser deposition of amorphous carbon films," *J. Appl. Phys.* **85**, 4222-4230 (1999).

50. A. Cheenne, J. Perriere, F. Kerherve, G. Hauchecorne, E. Fogarassy, and C. Fuchs, *Mat. Res. Soc. Symp. Proc.* **191**, 229-234 (1990).

51. M. Joseph, N. Sivakumar, P. Manoravi, and S. Vanavaramban, "Preparation of thin film of CaZrO3 by pulsed laser deposition," *Solid State. Ion.* **144**, 339-346 (2001).

52. A. Ishizaka and Y. Shiraki, "Low Temperature Surface Cleaning of Silicon and Its Application to Silicon MBE," *J. Electrochem. Soc.* **133**, 666-671 (1986).

53. G. Binnig, C. F. Quate, Ch. Gerber, "Atomic Force Microscope," *Phys. Rev. Lett.* **56**, 930-933 (1986).

54. R. Nishi, S. Araragi, K. Shirai, Y. Sugawara, and S. Morita, "Atom selective imaging by NC-AFM: case of oxygen adsorbed on a Si(111)-7×7 surface," *Appl. Surf. Sci.* **210**, 90-92 (2003).

55. T. Arai and M. Tomitori, "Bias dependence of Si(111)-7×7 images observed by noncontact atomic force microscopy," *App. Surf. Sci.* **157**, 207-211 (2000).

56. D. A. MacLaren, N. J. Curson, P. Atkinson, and W. Allison, "An AFM study of the processing of hydrogen passivated silicon (111) of a low miscut angle," *Surf. Sci.* **490**, 285-295 (2001).

CHAPTER IV

EPITAXIAL GROWTH OF Si ON Si(111)-7X7 AT ROOM TEMPERATURE

IV.1. Introduction

Epitaxial growth of Si on Si(111)-7x7 is a well-studied system because of its role for giving a fundamental understanding of homoepitaxy and potential applications in semiconductor devices.[1,2] Most of the available literature discussing growth of Si on Si(111)-7x7 have focused on molecular beam epitaxy (MBE)[3] and chemical vapor depositions (CVD).[4,5]

Homoeptaxial growth of thin films normally develops by the Frank-Van der Merwe (layer-by-layer) growth or by step propagation (step-flow) growth for a vicinal surface. For high-temperature growth, adatoms diffuse and adhere to step edges; therefore, nucleation does not take place on terraces. This results in the step-flow growth mode. When this growth mode is observed by reflection high-energy electron diffraction (RHEED), the diffraction pattern remains unchanged during growth.[6] As the substrate temperature is lowered, islands nucleation on terraces becomes preferential, resulting in the growth mode becoming layer-by-layer growth.[7] This growth mode is observed in RHEED as oscillations in the diffraction spots intensity. With further reduction in temperature, disordered three-dimensional (3D) structures and increased surface roughness develops due to further reduction in surface diffusion. In this case, the RHEED pattern decays and completely disappears after a certain thickness.

Only a few studies of pulsed laser deposition (PLD) of Si on Si were performed.[8,9] PLD is characterized by its periodic nature, in which the bursts of ablated materials reaching the substrate are separated by periods of no deposition. This results in an instantaneous high density of adatoms on the surface. The high energy of the plume species in PLD results in adatom energy much higher than for other deposition techniques, thus, enhancing surface diffusion. This has been shown to result in the observation of epitaxy for the growth of Si on Si(111)-7x7 at a lower substrate temperature than that observed for MBE, as has been discussed in previous chapters.

Development of low-temperature growth methods are of much interest in semiconductor fabrication. Lowering the epitaxial growth temperature is a key parameter to suppress the introduction of defects, such as dislocations and staking faults.[10] It has been shown that for Si-Ge the maximum epitaxial thickness without the introduction of any defects, referred to as critical thickness, is a function of the epitaxial growth temperature and the Ge mole fraction.[11] In their work, Eaglesham et al.,[12] showed that for Si on Si(100) grown at room temperature, the deposited Si becomes amorphous after growth of a limiting epitaxial thickness ($h_{epi} \sim$ 10-30 Å). This thickness increases rapidly with temperature. The mechanism involved is due to surface roughness during low temperature growth, which is postulated to be a general phenomenon occurring in other systems. In this sense, low temperature epitaxy refers to lowering the temperature at which the limiting epitaxial thickness becomes equal or longer than that required in thin film fabrication. The ability to achieve low temperature epitaxy prevents the alteration of the characteristics of those devices already fabricated on the wafer. This is particularly critical for submicron structures with abrupt interfaces or sharp doping profiles. To lower

the epitaxial growth temperature, or more accurately to increase the limiting epitaxial thickness h_{epi} at a certain substrate temperature, external energy sources, such as ions, electrons, or photons, were used to enhance surface diffusion.[13-15]

Electronic excitations by laser or electron beam interaction with surfaces have been shown to modify the surface properties.[16-20] Electronic-induced surface processes include selective removal of surface atoms, surface layer modifications, and the alternation of rates of some surface processes.[21] Removal of surface atoms occurs due to bond breaking as a result of single or multiple photon excitations. In semiconductors, bond breaking by laser pulses below the melting threshold is purely electronic.[22] Even what was thought of as purely thermal desorption was reported to involve electronic excitations.[23]

In Si(100)-2x1, bond breaking takes place due to the localization of two photo-generated surface holes at dimer sites [22]. Two-hole localization on surface sites of nonequilibrated valance holes was concluded to be the mechanism responsible for bond breaking when a Si(111)-(2x1) surface was excited by 1064 nm, 3.5 ns laser pulses.[24] The number of the electronically-removed atoms, due to laser excitations, depends on the laser wavelength and is a superlinear function of laser fluence, but is independent of the material's temperature.[20,21]

A few publications have considered the effects of the electronic excitations on the growth of thin films and nanostructures. Illumination of silica substrates with a low-fluence diode laser during deposition has been reported to unify the cluster's shape and narrow the size distribution of Ga nanoparticles grown at ~100 °C.[25] Recently, we studied the effects of laser-induced electronic excitations on the self-assembly of Ge quantum

dots on Si(100)-2x1 grown by pulsed laser deposition.[26] Electronic excitation was found to result in the formation of an epitaxial wetting layer and crystalline Ge quantum dots at ~260 °C, a temperature at which no crystalline quantum dots form without excitation under the same deposition conditions. Also, irradiation by a few hundred eV electron beam during deposition of CeO_2 on Si was reported to enhance epitaxy and reduce the required temperature for epitaxial growth from that without electron irradiation by more than 100 °C.[19] We report, on observation, of epitaxial growth of pulsed laser deposited Si on Si(111)-7x7 at room temperature depositing around 5.4 ML when femtosecond laser pulses are used to electronically excite the substrate. Reflection High-Energy Electron Diffraction shows that growth occurs by step flow. Without laser substrate excitation, disordered islands are formed. The effect is nonthermal.

IV.2. Experiment

Before loading into the deposition chamber, the Si(111) substrates (p-type, 20–50 Ω.cm, 4x2x0.4 mm in size) are first chemically cleaned, using modified Shiraki method.[27] After baking the deposition chamber and pumping it to ultrahigh vacuum (UHV), the Si substrate is cleaned by gradually heating it to ~1200 °C using direct current for about 2 minutes then cooling slowly (~2 °C/s) to 1000-800 °C. This procedure results in the formation of a strong (7x7) reconstruction pattern characteristic of clean Si(111)-7x7. Deposition is performed in the UHV chamber with the residual gas pressure lower than $5x10^{-10}$ torr. A RHEED system is used to probe the surface structure during pulsed laser deposition. The electron beam energy was kept at 8.6 keV during all

deposition runs and the electrons were incident, with a glancing angle of less than 4^{o} with the sample's surface. The diffracted patterns were observed on a fluorescent screen. These patterns were recorded during deposition using a charge-coupled device (CCD) camera.

A Ti:sapphire laser beam (pulse width ~100 fs, wavelength 800 nm, repetition rate 1 kHz) was split into two beams. The first beam was focused to 0.25 mm, measured at full-width at half-maximum (FWHM), and used to ablate the Si target with an energy density of 300 mJ/cm^2. The second beam was defocused to produce a beam with a FWHM of 3 mm, resulting in an energy density of 25 mJ/cm^2 on the Si(111) substrate. This energy density is far below the damage threshold of Si. The experimental setup is shown in Fig. 4.1. This surface excitation laser was incident with an angle of 45^{o} to the substrate's surface normal. To study the effect of laser excitation on the film morphology, two sets of samples were grown at room temperature for 20 second depositing (8.4 nm) ~5.4 ML. In the first set, the films were grown with no laser excitation beam on the substrates. In the second set, the substrates are subjected to laser excitation during deposition. In that case, the excitation laser beam was turned on and off with the ablation beam.

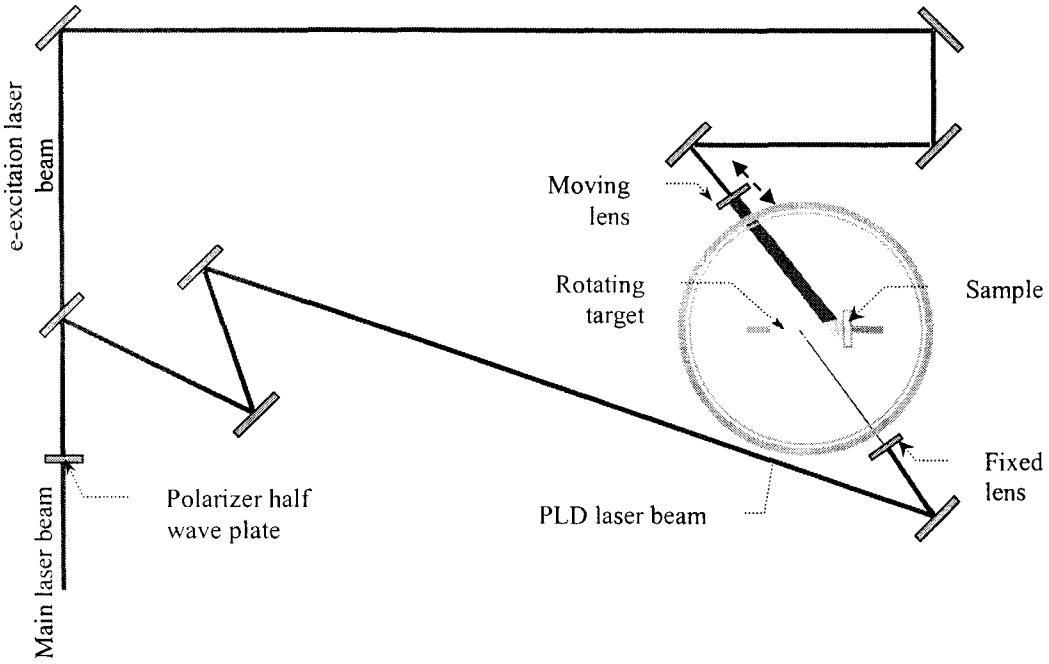

FIG. 4.1. Electronic excitation experimental optical setup. 100 fs laser beam is split into two beams. The first is focused and used to deposit the thin film. The second is incident on the sample during the deposition.

IV.3. Results and discussion

Figure 4.2 compares the change in the RHEED patterns for the films grown without laser excitation and those grown under laser excitation. Without laser excitation, Figs. 1(a)-(c), all of the (7x7) RHEED spots continuously decay during deposition until they completely disappear after 8.5 nm, indicating the formation of films that lack the long-range order. This is expected at room temperature, due to the lack of enough diffusion energy of the adsorbate atoms, which agrees with other observations as described above. The reconstructed spots completely disappear before the non-reconstructed ones, resulting in an intermediate (1x1) structure. On the contrary, for films

grown under the substrate laser excitation, laser pulses were 100 fs in duration at 1 kHz rate with pulse energy density of 25 mJ/cm^2. Fig. 4.2(d) – (f), the intensities of all the (7x7) pattern decay to a certain value during deposition and recover to their original values when the lasers are switched off. This is an indication of an epitaxial growth by step flow, as seen by a RHEED electron beam incident parallel to the terrace step edges.[28,29]

FIG. 4.2. RHEED images for laser enhanced epitaxial growth of Si on Si(111)-7x7 at room temperature along $[01\bar{1}]$ at electron energy 8.6 keV. (a) before PLD shows the 7x7, (b) after 10 s of PLD without laser of excitation, (c) after 20 s without laser of excitation, (d) before PLD and laser of excitation, (e) after 10 s of PLD with laser of excitation, and (f) after 20 s where PLD and laser excitation are off.

Normalized beam intensity versus time has been used to calculate the recovery time for the beam spot at room temperature with laser excitation. It has been established that RHEED intensity recovery tolerates a similarity to the surface-roughness recovery. The line scans in Fig. 4.3 describe the behavior of the reconstructed spot $(0\frac{4}{7})$ for two different runs. The curve labeled (a) is for the film deposition without laser excitation, showing no recovery for the spot intensity after the laser is turned off, as expected. The

curve labeled (b) is for deposition under laser excitation. In this case, the beam intensity drops suddenly to a plateau region, with no further intensity decay. The spot intensity relaxes back to its original value when both lasers are switched off. This behavior is the main characteristic of step-flow growth. The initial drop in intensity is attributed to the increase in the surface disorder due to the large density of adatoms. However, due to adatoms' surface diffusion to the terrace edges, continuous intensity decay to its complete disappearance does not take place. The intensity relaxation to the original value when the lasers are off is due to the diffusion of the excess adatoms to the terrace edges. The recovery time of the RHEED $(0\frac{4}{7})$ beam intensity after laser termination in Fig. 4.3. curve (b) was analyzed. This recovery curve shows two processes, an initial fast stage with recovery time τ_1 followed by a slow stage with a recovery time τ_2. The recovery of RHEED intensity with time after termination of deposition can be expressed by $I(t)=A_0 - A_1(1-\exp(-t/\tau_1)) - A_2(1-\exp(-t/\tau_2))$, where A_0, A_1, and A_2 are constants, and τ_1 and τ_2 are temperature dependent time constants of the fast and slow processes of recovery, respectively. From the RHEED intensity curve (b), the recovery time constants are τ_1 = 1.25 s, and τ_2 = 6.6 s. The surface diffusion coefficient (D) can be calculated from the relation $\langle x^2\rangle = 2D\tau$, where $\langle x^2\rangle$ is the mean square displacement of the adatom diffusion (diffusion length which is restricted by the terrace width in case of step-flow growth), and τ is the average diffusion time.[30] For the fast-recovery stage, $D_1 = (8.6\pm0.75)\times10^{-13}$ cm^2/s and for the slow recovery stage $D_2 = (1.6\pm0.31)\times10^{-13}$ cm^2/s. Comparing the results we obtained, it was found that the self-diffusion coefficient for Si at room temperature (~2.8×10^{-8} cm^2/s at RT)[31] was much higher than in the presence of laser excitation. Meanwhile, the surface diffusion coefficient with the laser excitation is in the same order

of magnitude with self-diffusion coefficient at high temperature (~5×10^{-13}cm^2/s at 1100 °C).[31] We deduce this as a direct effect of laser excitation.

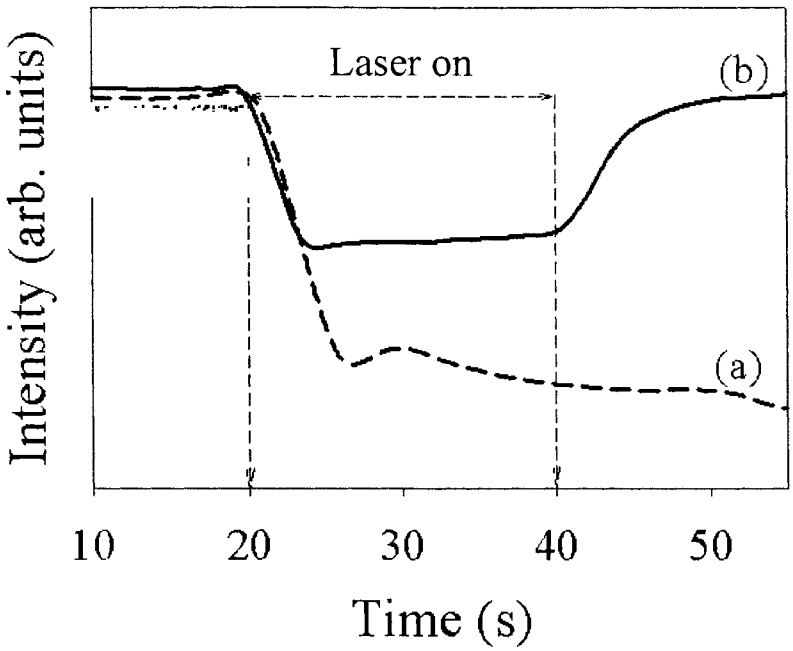

FIG. 4.3. Normalized RHEED intensity for reconstructed $(0\frac{4}{7})$ spot of Si(111)-7x7 at room temperature. PLD beam was kept at constant energy density of 300 mJ/cm^2 for 20 s while the laser excitation was kept at an energy density of 25 mJ/cm^2. (a) without excitation laser, (b) with excitation laser.

The full width at half maximum (FWHM) of the $(0\frac{4}{7})$ reconstructed spot parallel and normal to the incident beam (terrace step edge) shows no detectable change during deposition with the absence of the laser excitation as shown in Fig. 4.4(a). However, when the laser excitation is applied, the FWHM parallel to the terrace step edge (parallel to the beam) shows no change, while the one normal to the terrace step edge decays to a constant value during deposition and recovers again after both laser beams are turned off, as shown in Fig. 4.4.(b). Since the FWHM of the RHEED spot is interpreted as a change

in the average terrace width during growth,[28] this change can be linked to the effect of the applied laser excitation.

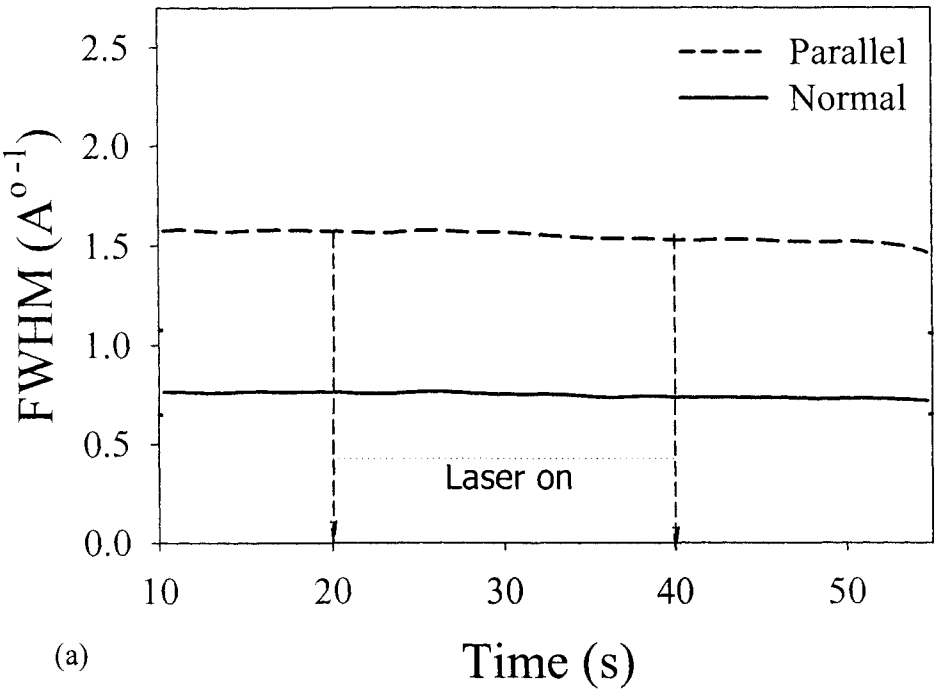

(a)

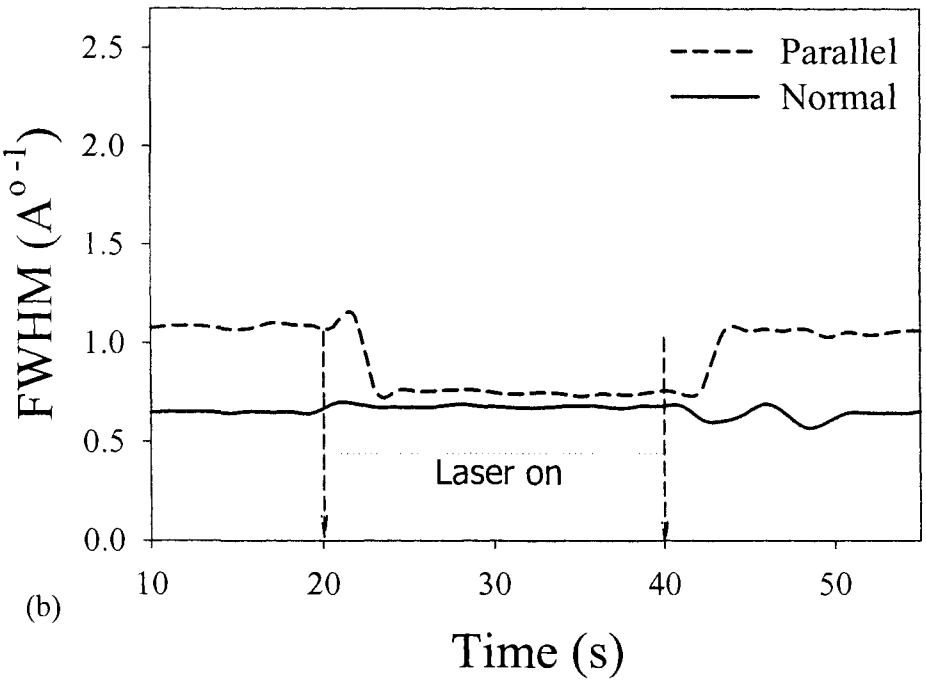

FIG. 4.4(a). Full width at half maximum (FWHM) normal and parallel to the step edge for reconstructed spot $(0\frac{4}{7})$ with PLD laser only, for 20 s at room temperature. (b) Full width at half maximum (FWHM) normal and parallel to the step edge for reconstructed spot $(0\frac{4}{7})$ with both PLD and excitation lasers on for 20 s at room temperature. Most probable movement of the adatom is in the direction normal to the terrace edge.

Figure 4.5. shows atomic force microscopy (AFM) scans for two different films (after depositing around 5 ML). In this figure, n is the number of the clusters, d is the average cluster size and θ is the coverage ratio (sum of the cluster areas per total scanned area). Fig. 4.5(a) is the AFM scan for deposition without laser excitation, whereas Fig. 4.5(b) is for deposition with laser excitation. Although the number of clusters per unit area (n) does not change, 33 and 32 clusters for samples deposited with and without laser excitation, respectively, the average cluster size is increased from 366 nm for samples deposited without laser excitation to 733 nm for samples deposited with laser excitation.

In addition, the coverage ratio θ is increased from 2% without laser excitation to 9% with laser excitation. These changes could enhance the film morphology.

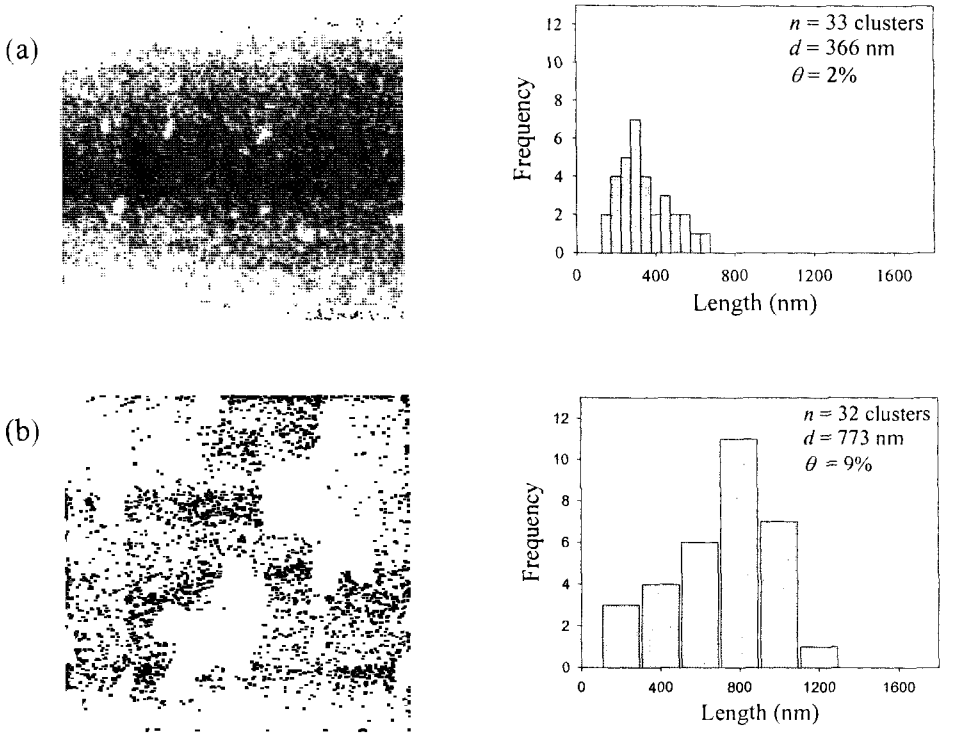

FIG. 4.5. AFM images and cluster distribution of Si 5.4 ML on Si(111)-7x7 at room temperature. (a) Sample without laser excitation, and (b) Sample with ~25 mJ/cm^2 laser excitation of the substrate. The average cluster size and coverage ratio increased in a sample exposed to laser excitation.

Based on the interaction of lasers with semiconductors below the damage threshold, two mechanisms have been proposed. The first one is due to the energy coupling between the surface and the adatoms. The second is the dimar-adatom vacancy creation mechanism. The most adequate model was developed by Itoh,[32] and was based on the theory of sputtering the surface by sub-bandgap lasers. In this mechanism, lattice modification takes place with higher efficiency on the surface than in the bulk because of atoms on the surface have fewer nearest neighbors than those in the bulk.[33] The ejection of surface atoms is a result of the rupture of the surface bond.

In the absence of laser excitation and when the substrate at either low temperature or under fast deposition the atom mobility is extremely low. In this case, the process takes place before the subsequent adatoms. The diffusion of these adatoms is unable to compete with the fluctuations due to those resulting from the subsequent adatoms, which cause an increase in the surface roughness. Whereas, in the presence of laser excitation, the diamer-adatom vacancy is created. In this case, the adatom has enough diffusion energy either to occupy the nearest vacant sites or to relax to the desired expitaxial sites.

IV.4. Conclusion

In conclusion, we studied the growth of Si on Si(111)-(7x7) using pulsed laser deposition at room temperature. By irradiating the substrate during the deposition, an external assistance involved with the laser fluence assist a successful epitaxial growth to be carried out. Characterization, using both RHEED and AFM analyses, shows that, under laser excitation, the cluster morphology significantly promises an improvement

through both lowering the growth temperature and increasing the crystal quality by decreasing the film roughness.

IV.5. References

1. Y. Shigeta, J. Endo, and K. Maki, "Scanning-tunneling-microscopy study of surface morphology at the initial growth stage of Si on a 7x7 superlattice surface of Si(111)," *Phys. Rev. B* **51**, 2021-2024 (1995); "A characteristic feature of crystalline thin-film growth of Si on a 7x7 super lattice surface of Si(111)," *J. Cryst. Growth* **166**, 1-4, 617-621 (1996).
2. T. Hasegawa, M. Kohno, S. Hosaka, and S. Hosoki, "Dynamic observation of Si crystal growth on a Si(111) 7X7 surface by high-temperature scanning tunneling microscopy," *Phys. Rev. B,* **48**, 1943-1946 (1993).
3. H. Omi, Y. Homma, V. Tonchev, A. Pimpineui, "New types of unstable step-flow growth on Si(111)-7X7 during molecular beam epitaxy: scaling and universality," *Phys. Rev. Lett.* **95**, 216101-4 (2005).
4. L. Andersohn, Th. Berke, U. Köhler, and B. Voigtländer, "Nucleation behavior in molecular beam and chemical vapor deposition of silicon on Si(111)-7X7," *J. Vac. Sci. Technol. A* **14(2)**, 312-318 (1996).
5. B. S. Swartzentuber, "Direct Measurement of Surface Diffusion Using Atom-Tracking Scanning Tunneling Microscopy," *Phys. Rev. Lett.* **76**, 459-462 (1996).
6. T. Shitara, D. D. Vedensky, M. R. Wilby, J. Zhang, J. H. Neave, and B. Joyce, "Step-density variations and reflection high-energy electron-diffraction intensity oscillations during epitaxial grown on vicinal GaAs(001)," *Phys. Rev. B* **46** (11), 6815-6824 (1992).

7. D. Y. Noh, Y. Hwu, and K. S. Liang, "Long-range behavior of the layer-by-layer growth in Si/Si(111)-7x7 homoepitaxy," *Phys. Rev. B,* **56 (12)**, R7080-R7083 (1997).

8. M. S. Hegazy and H. E. Elsayed-Ali, "Observation of step-flow growth in femtosecond pulsed laser deposition of Si on Si(100)-2x1," *J. Vac. Sci. Technol. A* **20(6)**, 2068-2071 (2002).

9. M. A. Hafez, M. S. Hegazy, H. E. Elsayed-Ali, H. E., "Indium growth on Si(100)-2x1 by femtosecond pulsed laser deposition," *J. Vac. Sci. Technol. A* **23(6)**, 1681-1686 (2005).

10. N. Tamura and Y. Shimamune, "45nm CMOS technology with low temperature selective epitaxy of SiGe," *Appl. Surf. Sci.* **254(19)**, 6067-6071 (2008).

11. D. C. Houghton, "Strain relaxation kinetics in Si(1-x)Ge(x)/Si heterostructures," *J. Appl. Phys.* **70**, 2136-2151 (1991).

12. Eaglesham, "Limiting thickness h_{epi} for epitaxial growth and room-temperature Si growth on Si(100)," *Phys. Rev. Lett.* **65(10)**, 1227-1230 (1990).

13. A. Hokazono, K. Ohunchi, K. Miyano, I. Mizushima, Y. Tsunashima, and Y. Toyoshima, *Tech. Dig. Int. Electron Devices Meet.* 243 (2002).

14. S. -H Lim, S. Song, T. -S. Park, E. Yoon, and J.-H Lee, "Si adatom diffusion on Si (100) surface in selective epitaxial growth of Si," *J. Vac. Sci. Tecnol. B* **21(6)**, 2388-2392 (2003).

15. R. M. Wallance, P. A. Taylor, W. J. Choyke, and Jr. Yates, "An ESDIAD study of chemisorbed hydrogen on clean and H-exposed Si(111)-(7×7)," *Surf. Sci.* **239**, 1-12 (1990).

16. K. Tanimura, E. Inami, J. Kanasaki, W. P. and Hess, "Two-hole localization mechanism for electronic bond rupture of surface atoms by laser-induced valence excitation of semiconductors," *Phys. Rev. B* **74**, 35337 1-8 (2006).

17. Y. Zhang, J. Lian, C. M. Wang, W. Jiang, R. C. Ewing, and W. J. Weber, "Ion-induced damage accumulation and electron-beam-enhanced recrystallization in $SrTiO_3$," *Phys. Rev. B* **72**, 094112 1-8 (2005).

18. N. Itoh and A. M. Stoneham, "TOPICAL REVIEW: Treatment of semiconductor surfaces by laser-induced electronic excitation," *J. Phys.: Condens. Matter,* **13(26)**, R489-R503 (2001).

19. T. Inoue, Y. Yamamoto, and M. Satoh, "Electron-beam-assisted evaporation of epitaxial Cdo_2 thin films on Si substrates," *J. Vac. Sci. Technol. A* **19(1)**, 275-279 (2001).

20. J. Kanasaki, K. Iwata, and K. Tanimura, "Translational Energy Distribution of Si Atoms Desorbed by Laser-Induced Electronic Bond Breaking of Adatoms on Si(111)-7x7," *Phys. Rev. Lett.* **82(3)**, 644-647 (1999).

21. A. Stoneham and N. Itoh, "Materials modification by electronic excitation," *Appl. Surf. Sci.,* **168**, 186-193 (2000).

22. J. Kanasaki, K. Katoh, Y. Imanishi, and K. Tanimura, "Electronic bond rupture of Si-Dimers on Si(001)-(2x1) induced by pulsed laser excitation," *Appl. Phys. A* **79**, 865-868 (2004).

23. B. R. Trenhaile, V. N. Antonov, G. J. Xu, K. S. Nakayama, and J. H. Weaver, "Electron-simulated desorption from an unexpected source: Internal hot electrons for Br Si(100)-2 x 1," *Surf. Sci.* **5839(1)**, L135-L141 (2005).

24. E. Inami, E. and K. Tanimura, "Electronic Bond rupture of Si atoms on Si(111)-2x1 induced by valence excitation," *Phys. Rev. B* **76**, 035311 1-11 (2007).

25. V. A. Fedotov, K. MacDonald, N. I. Zheludev, and V. I. Emel'yanov, "Light-controlled growth of gallium," *J. Appl. Phys.* **93(6)**, 3540-3544 (2003).

26. M. Hegazy and H. E. Elsayed-Ali, "Quantum-dot Infrared Photodetector Fabricated by Pulsed Laser Deposition," *J. Laser Micro/Nanoengineering* **1(2)**, 111-114 (2006).

27. A. Ishizaka and Y. J. Shiraki, "Low Temperature Surface Cleaning of Silicon and Its Application to Silicon MBE," *Electrochem. Soc.* **133**, 666-671 (1986).

28. J. Kanasaki and K. Tanimura, "Laser-induced electronic desorption of Si atoms from Si(111)-(7x7)," *Phys. Rev. B* **66(12)**, 25320-5 (2002).

29. A. Ishizaka and Y. J. Shiraki, "Low Temperature Surface Cleaning of Silicon and Its Application to Silicon MBE, " *Electrochem. Soc.* **133**, 666-671 (1986).

30. J. H. Neave, P. J. Dobson, B. A. Joyce, and J. Zhang, "Reflection high-energy electron diffraction oscillations from vicinal surfaces: a new approach to surface diffusion measurements," *Appl. Phys. Lett.* **47(2)**, 100-102 (1985).

31. W. E. Beadle, J. C. Tsai, and R. D. Plummer, *Quick reference manual for silicon integrated circuit technology,* Wiley, New York (1984).

32. N. Itoh and A. M. Stoneham, "TOPICAL REVIEW: Treatment of semiconductor surfaces by laser-induced electronic excitation," *J. Phys.: Condens. Matter* **13(26)**, R489-R503 (2001).

33. J. H. Neave, P. J. Dobson, B. A. Joyce, and J. Zhang, "Reflection high-energy electron diffraction oscillations from vicinal surfaces: a new approach to surface diffusion measurements," *Appl. Phys. Lett.* **47(2)**, 100-102 (1985).

CHAPTER V

INFLUENCE OF Si DEPOSITION ON THE PHASE TRANSITION TEMPERATURE

V.1. Introduction

Formation of metastable structures of Si(111) can probably be explained by understanding the role of impurities in the material. On the clean Si(111) surface, the (2x1) structure can be generated in a process involving mass transport. Annealing and subsequent quenching of Si(111) play important roles in the formation of the reconstructed surfaces. As an example, the Si(111) surface cleaved in ultrahigh vacuum exhibits a (2x1) structure. This structure is metastable and transferred into either the (7x7) or (5x5) structure upon heating to 400°C. Studies using Scanning Tunneling Microscopy (STM) and Reflection Electron Microscopy (REM) have shown that near the transition temperature the two phases exist on the surface.[1,2]

A secondary nuclei form of (7x7) on terraces can be observed only on terraces with very rapid quenching to low temperature.[3,4] The method relies on monitoring of the RHEED pattern of deposition Si on Si(111) sample during quenching and exact determination of the onset of the $(1x1)_h$ to (7x7) phase transition. Any structural analysis relies on rapid quenching which attempts to freeze surface characteristic features which then leads to understanding surface transformation. To achieve this goal, a special experimental setup was used.

In this part, high temperature reconstruction dynamics are modified through the pulsed laser deposition (PLD) of Si on Si(111)-7x7. Reflection high-energy electron diffraction (RHEED) during the Si(111)-$(1x1)_h$ to (7x7) phase transition shows that Si deposition lowers the transition temperature.

V.2. Experiment

The Si(111) sample was prepared for an epitaxial ready, as described above. After the cleaning process and obtaining a clear and strong (7x7) reconstruction, a Ti-sapphire laser (100 fs, 800 nm, 1 kHz) was used to ablate a Si target on Si(111)-$(1x1)_h$ during quenching from high temperature. To measure the transition temperature during quenching with and without Si deposition, the experiment was performed as follows:

Initially, in the absence of the laser ablation plume, the Si(111) was kept at a temperature above the phase transition temperature for 1 minute to ensure the uniformity of the temperature throughout the sample's surface area. The heating current was switched off and the RHEED pattern was recorded. To ensure that any change in transition temperature during quenching is a result of the Si deposition, a 5 ML of Si was deposited first at 920 ^{o}C (above the transition temperature) with a typical deposition rate of 0.4 ML/s. Then, the quenching process was performed.

In the later stage, the Si(111) was kept at a temperature above the phase transition temperature, and in the absence of the laser ablation plume, the heating current was switched off, while the RHEED pattern was recorded. Then, in the presence of Si laser

ablation plume, the sample was kept at the same high temperature as was done without an ablation plume. The RHEED intensity was observed as the substrate was exposed to the Si plume and the Si(111) substrate was quenched at a rate of ~40 °C/s.

V.3. Results and discussion

A RHEED pattern of the clean Si(111)-1x1 at high temperature (920°C) is show in Fig. 5.1.(a). After the quenching process without any deposition, a RHEED (7x7) reconstruction appears, as shown in Fig. 5.1(b). Fig. 5.1(c). shows the RHEED pattern for the reconstructed surface (7x7) after depositing a 5 ML at 920°C and the quenching process. A normalized RHEED line scan for the reconstructed spot $(0\frac{4}{7})$ was used to measure the transition temperature onset. We did not detect any changes for either samples, as shown in Fig. 5.1(d).

On the quenched samples where the laser ablation plume was incident, RHEED observations were recorded. A normalized RHEED line scan for spot $(0\frac{4}{7})$ shows a detectable change in the onset transition temperature. The transition temperature for a quenched sample without Si deposition is about 840 °C. On the other hand, there was a shift toward the low temperature and the onset transition temperature was about 820 °C, for the quenched sample with Si deposition as shown in Fig. 5.2.

We interpret this result based on the effect of adatom mobility on the nucleation of the (7x7) structure. In the vicinity of the transition temperature, the two phases co-exist

on the surface. When the surface temperature is lowered below the transition temperature, the reconstruction starts to grow at the step edges, then, expands across the terraces.[1] Since the high temperature $(1x1)_h$ phase has higher density than the (7x7) phase, the excess atoms, found on large terraces after quenching, are released when the lower density (7x7) is formed, as shown in Fig. 5.3. The quenching process results in the cooling of the surface at a lower rate than the time needed for adatoms to diffuse across the terraces; consequently, the adatoms are trapped on the surface, forming secondary (7x7) nuclei on terraces, thus reducing the observed $(1x1)_h$ to (7x7) transition temperature.

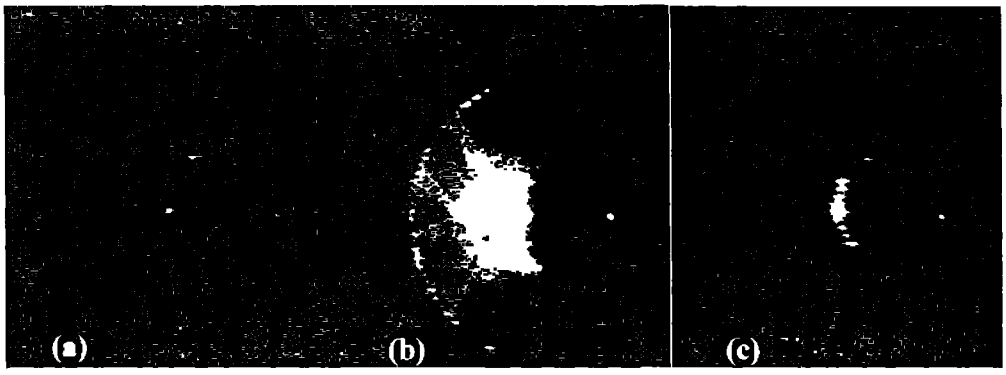

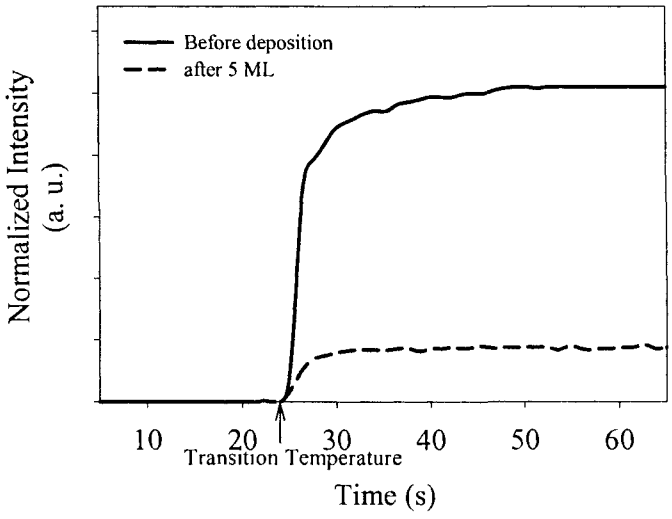

(d)

Fig. 5.1. RHEED observation during quenching process, (a) at 920 °C shows the $(1x1)_h$, (b) after the transition temperature without any deposition, (c) after transition temperature with a 5 ML of Si was deposit at 920 °C, (d) normalized RHEED intensities for $(0\frac{4}{7})$ reconstructed spot as a function of cooling time for both samples.

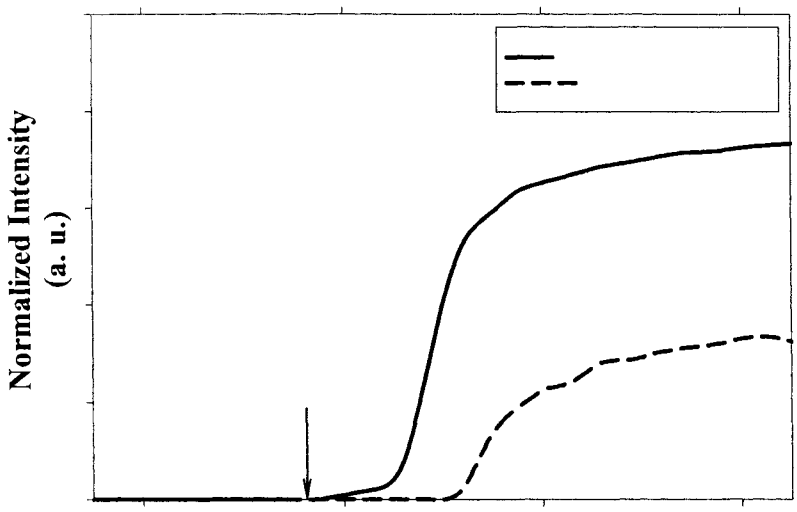

FIG. 5.2. Normalized RHEED intensity for $(0\frac{4}{7})$ reconstructed spot as a function of cooling time and temperature for sample without and during the laser ablation.

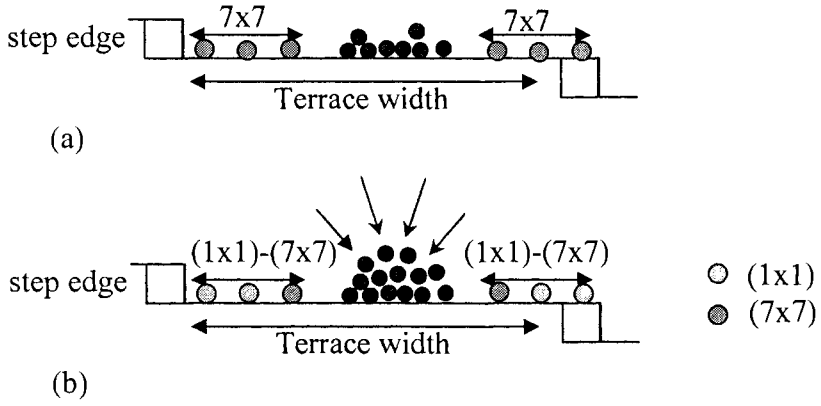

FIG. 5.3 Quench process model, around the transition temperature, at the step edge (a) in case of no Si deposition, the (7x7) phase becomes dominant, (b) in case of Si deposition, the $(1x1)_h$ phase becomes dominant.

V.4. REFERENCES

1. G. Binnig, C. F. Quate, and Ch. Gerber, "Atomic force microscope," *Phys. Rev. Lett.* **56**, 930-933 (1986).
2. W. Telieps and E. Bauer, "The 7 x 7 ↔ 1 x 1 phase transition on Si(111)," *Surf. Sci.* **162**, 163-168 (1985).
3. Y. -N Yang and E. D. Williams, "High atom density in the "1x1" phase and origin of the metastable reconstructions on Si(111)," *Phys. Rev. Lett.* **72(12)**, 1862-1865 (1994).
4. M. Fehrenbacher, H. Rauscher, and R. J. Behm, "Influence of SiH_4 deposition on the Si(111)1x1-7x7 phase transition," *Phys. Rev. B* **54**, R17284-R17287 (1996).

CHAPTER VI

ELECTRON STIMULATED DESORPTION ION ANGULAR DISTRIBUTION

VI.1. Introduction

Electron Stimulated Desorption Ion Angular Distribution (ESDIAD) has been used as a technique to acquire information on the configuration of adsorbates on solid surfaces. In this report, we built an instrument that measures ESDIAD images of desorbing ions in real time and modified this system to work as time-resolved ESDIAD, using a time-resolved surface lattice probe technique. Our goal is to test the ESDIAD system by monitoring the surface reactions for NaCl, single crystal, in real time.

Many techniques in surface studies involve the bombardment of the adsorbates with electrons, such as in LEED (Low Energy Electron Diffraction), HREELS (High-Resolution Electron Loss Spectroscopy) and ESDIAD. In ESDIAD, low energy electrons (less than 500 eV) interact with the adsorbed atoms or molecules on the surface to produce positive ions. The direction in which these ions are emitted is used to determine the bond's directionality. The first experiment of a positive ion's emission under an electron bombardment was reported by Dempster *et al.*[1] Later pioneering work on the electronic desorption of neutral species was conducted by Kobosew and Isikawa.[1] This technique, which uses a low energy electron beam to excite the surface desorption processes, has become generally identified as electron stimulated desorption (ESD).

The beginning of the modern approach to ESD as a surface technique is attributed to Young[2] and Moore,[3] who first undertook a systematic study of ion production using

mass spectrometric techniques. The first theory to explain the production of positive ions and neutrals was developed independently by Menzel, Gomer[4] and Redhead (MGR theory).[5] Their considerations are based on the excitation of valence electrons of adsorbate. leading to dissociation and subsequent expulsion of ions and neutrals. Feibelman and Knotek developed the theory of ESD further.[6] Later, Yates *et al.*[7] developed the digital ESDIAD system that measures the kinetic energy distribution of CO^+ ions.[8,9] Madey *et al.* used adopted pulse-gated systems to acquire mass-selected ESDIAD images.[10,11] Later, time of flight (TOF) measurements have been carried out to identify mass and transitional energy of desorbing ions.[12-17] Yates and co-workers also used time of flight TOF-ESDIAD system to investigate the striped structure of the oxidized Cu(110) surface and its interaction with co-adsorbed CO.[18] Afterward, we proposed time-resolved ESDIAD.

In this experiment, we built an ESDIAD setup at the Physical Electronics Research Institute at Old Dominion University as a tool to use electrons to probe the surface of NaCl crystal. The collected images for the NaCl have been converted to a contour space to determine the bond directionality.

VI.2. Electronic excitation

When considering collisions between an incident low-energy particle ($E_i \sim 500$ eV) of mass m and a free particle of mass M, the maximum energy transferred (dE) during the process with classical kinematics, for hard-sphere scattering, is $\frac{dE}{E_i} \cong \frac{2m}{M}$

where, m << M, corresponding to electrons impinging on atoms or molecules. Therefore, the fractional energy transfer is in the order of ~ 0.001 for electron atomic hydrogen collisions, implying that less than 0.5 eV would be partitioned to the H atom in this case for 500 eV.

However, ESD experiments often observe desorbing molecules, ions and molecular fragments with mass greater than 1 amu and with kinetic energies in the range from 2-10 eV. This indicates that direct momentum transfer is not usually dominant in electron adsorbate collisions and that electronic energy transfer must be considered.

VI.3. Models for electron stimulated desorption

Many theories have been proposed to explain the desorption process. The main one, which is widely accepted, is the Menzel-Gommer-Redhead (MGR) model. It also follows the Franck Condon principle, which states that the electronic transition takes place quickly, compared to the time required for a nuclear motion (*i.e.,* the velocity and inter-nuclear separations remain unchanged).

VI.3.A. The Menzel-Gomer-Redhead (MGR) model

The mechanism proposed is schematically shown in Fig. 6.1. The potential energy diagram shows the processes involved in the electron-stimulated desorption of an adsorbed species as an ion. According to the MGR model, the initiating step in the process is the ionization or excitation of an adsorbed atom or molecule by electron impact. An electron can be removed from one of the stable levels of an adsorbed species.

This excitation process results in charged or excited adspecies, whose interaction energy curve with the solid may be very different from that of the ground state neutral species. The excited species may have a shallow, attractive potential wall or no attractive region at all. After the excitation process, the system will relax by the excited species moving away from the surface, thus reducing the system's potential energy and imparting equivalent kinetic energy to the excited species. If no further processes intervene, then the ion or excited neutral will appear in the gas phase with a kinetic energy range as shown in the Fig. 6.1.

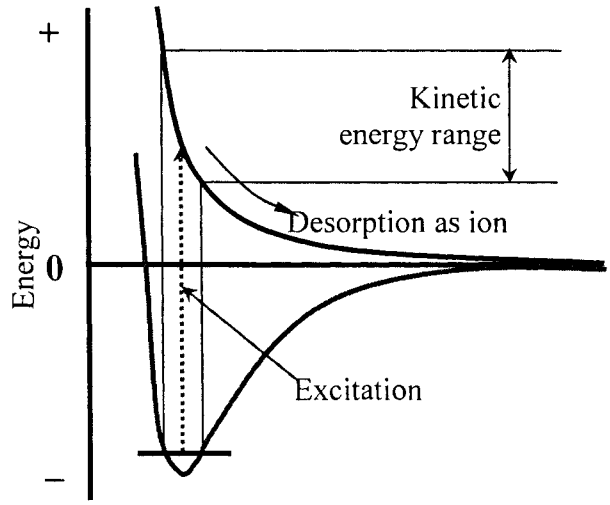

FIG. 6.1. MGR model mechanism shows the desorption of adsorbed

The generation of ground state neutral species with excess, which is a similar process, as shown in Fig. 6.2, explains kinetic energy. Since the excited species is very close to the surface, it has a finite probability of being neutralized by an Auger or

resonance neutralization process, in which an electron from the surface tunnels into the vacant electronic level of the excited species. The net result of this process is to return the excited species to the ground state potential energy curve but with some kinetic energy. If this kinetic energy is greater than the potential energy difference between the vacuum level and that represented by the ground state curve at the point of de-excitation, then the atom or molecule can escape from the surface as a neutral species. Because the probability of these neutralization or de-excitation processes is strongly dependent on the distance between the excited species and the surface, these processes will be much more efficient for species that are found close to the surface in the adsorbed ground state.

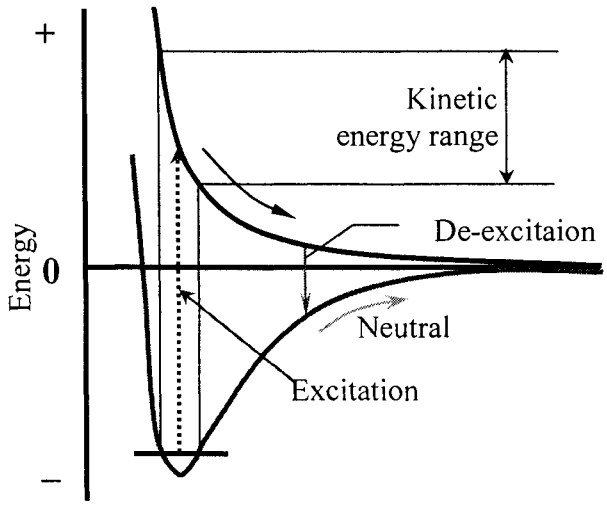

Fig. 6.2. ESD Potential energy diagram where the neutral desorption is shown.

VI.3.B. Antoniewicz model

Antoniewicz proposed a modification of the original MGR model which has been successful in describing ESD from physisorbed layers.[19] An adsorbate, by interaction

with an incident electron, becomes instantaneously positively ionized (with respect to time scales of nuclear motion). The ion experiences a screened image charge potential, which attracts it toward the surface. Pauli repulsion is also diminished for the ion (as compared to the neutral) since it has a smaller atomic radius. These two effects allow the ion to move very close to the surface, which, in turn, dramatically increases the probability of resonant tunneling or Auger neutralization by substrate electrons. Upon re-neutralization, the image potential vanishes, leaving only the Pauli repulsion. The re-neutralized species, still moving toward the surface, is repelled, thus, effectively bouncing off the substrate to escape as a desorbing neutral particle. Antoniewicz also proposed a more complex, two-electron process to explain desorption of the positive ions. This is illustrated in Fig. 6.3, where the ground-state configuration (M+A) is promoted to an excited ionic curve $(M+A^+)^*$. Again, the excited ion moves toward the surface, where tunneling neutralizes the ion, placing the system high on the ground-state (M+A) curve. Pauli repulsion suddenly dominates at very small separations and will deflect the hot neutral from the substrate, causing it to escape. Since the probability of electron hopping processes at short distances is finite, the neutral species may be re-ionized by resonant electron tunneling into the substrate during its escape, yielding ionic desorbing species, as shown by a curve crossing with the $(M+A^+)$ curve.[19]

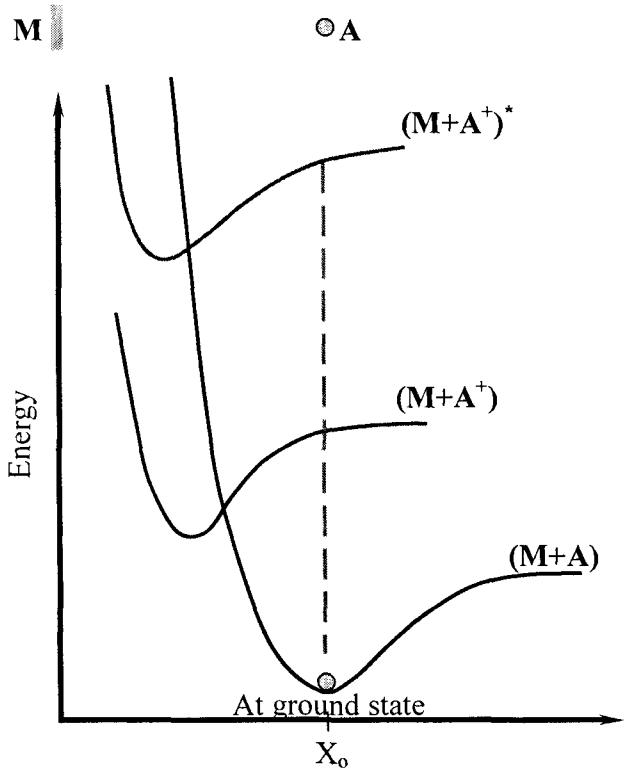

FIG. 6.3. Schematic representation of the Antoniewicz model, illustrates that the proposed sequence leading to neutral and ion particle desorption.

VI.4. Main idea for ESDIAD

For an electron beam incident on a surface, the ratio of the desorbed ion current to the impinging electron current defines the ion desorption efficiency (η). In turn, $\eta = nQ$, where Q is the ionic desorption cross-section and n is the gas coverage at the surface desorbable by electron impact. Desorption, like ion, is accompanied normally by a greater depletion of neutrals from the surface and, in principle, we can employ any surface sensitive technique to monitor changes in the surface coverage.

If the instrumental response is proportional to coverage n, then the depletion of the surface is given by $dn/dt = nQJ/e$, where Q is the total desorption cross-section and J and e are, respectively, the electron current density and the electron charge. This leads to an exponential decay and so by following the temporal decay of the signal (proportional to n), we have a basis for determining the total desorption cross-section. With a current density ~ 10^{-3} Acm^{-2}, as is the characteristic of many Auger experiments, then for a typical value of ESD total desorption cross-section of 10^{-18} cm^2, the signal will be reduced to 1% of its initial value during 12 min of bombardment. Under usual conditions with the technique of ESD, the electron current density is set < 10^{-6} Acm^{-2} in order to minimize the perturbation caused by the impinging electrons. It is important, when comparing total cross-section measurements derived from sampling ions in ESD with those derived from other surface sensitive techniques, to recognize the possible specificity of each response. Thus, for example, the same electron bombardment at a tungsten-oxygen interface, as monitored by AES and ESD, gave rise to a significantly higher value of total desorption cross-section as deduced by ESD. On this basis, it is, in general, better to employ methods based on the direct detection of ejected ESD species for the study of desorption mechanism, but, of course, parallel measuring techniques are complementary in the goal of understanding the overall surface phenomena.[20]

The most usual approach in recent years to identify ions desorbed from surfaces is by a mass spectrometer of the quadruple design.[21] This can be linked with a retarding grid assembly, serving as a high-pass filter, to determine the energy of the desorbed ions. Moreover, with a hemispherical grid assembly and the ion collector, there is a possibility

of collecting the whole of the desorbed current and fix desorption efficiency in the absorbate terms. A system of this kind is illustrated in Fig. 6.4.

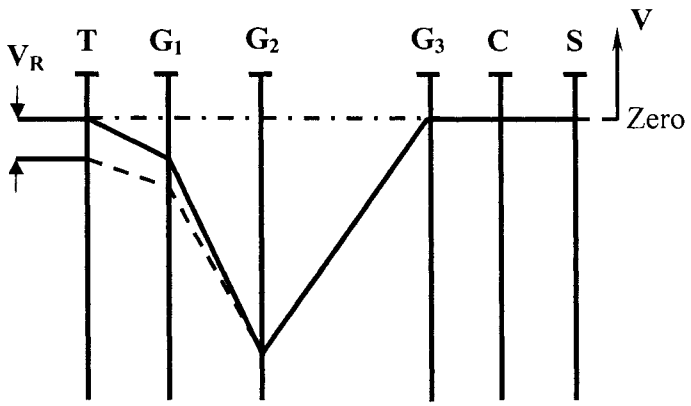

FIG. 6.4. Voltage configuration at electrodes (four grids optics)

Modern ESD has been carried out using a time-of-flight technique[22] in association with surface mass spectrometry based on a quadruple filter. The mass spectrometer allows identification of the desorbed species, while the time-of-flight technique is used to determine the energy distribution of the desorbed ions. The quadruple mass filter is interposed between the surface and a channel electron multiplier, which serves both as a single ion detector in flight-time studies (with the mass filter off) and as an ion detector for the mass filter. The approach with the time-of-flight technique is to set a pulsed electron beam of a suitable low intensity so that, at most, one ion is collected per electron pulse at the surface. The initiating electron pulse at the target and the output of the ion detector serve, respectively, as the start and stop signals of a time-to-voltage converter and by operating over many cycles (frequency > 1 kHz), a histogram of transit times is

built up in a pulse-height analyzer linked to the output of the time-to-voltage converter. The flight-time corresponds to the kinetic energy of the ions. In this way, the energy distribution of the desorbed ions is measured.

The arrangement of the hemispherical grids pair around the sample surface is similar to the earlier retarding field energy analyzer and serves here to accelerate the ions radically away from the surface.[23] Ions that pass through these grids are accelerated through a planar grid and under greater acceleration are brought to the microchannel plates (MCP), where the ESDIAD pattern is observed and recorded.

Figure 6.5. shows the chemisorption of oxygen on W(100).[24] With the electron beam energy 100-400 eV, the surface containing an adsorbed layer was bombarded with low energy electrons (~100 eV), thus, ions were desorbed leaving the surface in well defined cones along the bond direction. The generated images on the screen are sensitive functions of the bonding mode of the adsorbates to the surface, the cross section of desorption and the ion energy distribution. Thus, ESDIAD provides unique information about the structure of the surface and adsorbates. The particles ejected encounter a four-grid electrostatic lens array. All positive ions and neutral ESD species pass through the grid system, striking the first of two microchannel plates (MCP), then producing a large numbers of electrons (~10^6 electron) for each positive ion (or excited-state neutral). This electron pulse is accelerated into a resistive anode, causing an expanding ring of charge, centered at the pulse arrival point, to propagate across the thin conductive film. The position analysis computer translates it into a three-dimensional image.

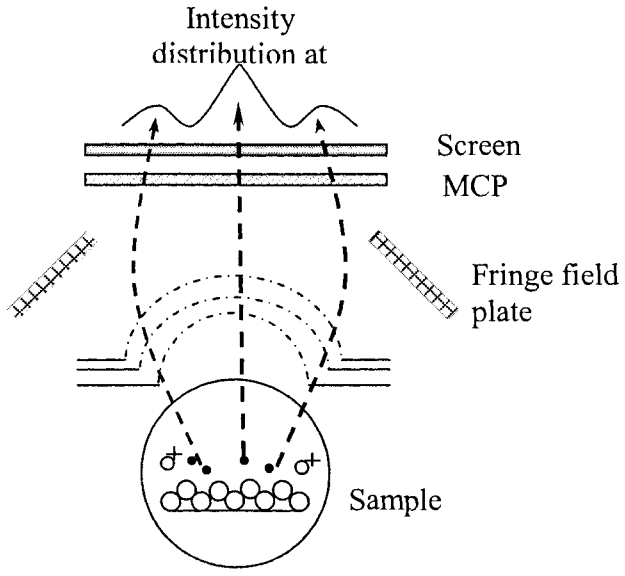

Fig. 6.5. Chemisorption of Oxygen on W(100) [after ref 24].

VI.5. Experimental setup

ESDIAD experiment was built similar to that built by Czyzewski *et al.*[19] with a modification demonstrated by Yates *et. al.*[1] as shown in Fig. 6.6. The apparatus consists of: a comprised two micro-channel plates (MCP) with a phosphor screen attached to four grids in the front (two spherical grids and two plane grids) and a continuous wave (CW) electron gun. The charged particles are transmitted through the grid system to MCP and then noticed by the phosphor screen.

The experimental work was carried out in UHV chamber with a base vacuum better than $5x10^{-10}$ torr pumped by the combined ion-titanium sublimation pump. A CW electron gun was used, with electron beam focused to a spot of 0.5 mm diameter on the surface of the sample. A clean NaCl single crystal was chosen to test the system because of its simple cubic surface cell structure, and it has a minimal surface mismatching. A

1x1 cm thin slab cut from NaCl was mounted on XYZ rotary manipulator and could be heated by attaching Ta wire to the edge of the sample holder.

A charge coupled device (CCD) camera was used to record ESDIAD images appearing on the phosphor screen. The incident electron beam impinges on the surface with polar angle of 45° from the surface normal. The primary energy of the electron beam can be set in a range between 100 V to 1000 V. ESDIAD images with different applied voltages on the mesh which were acquired with 160 ms exposure time. The patterns were digitally stored, processed and converted to a contour image format to detect the bond directionality.

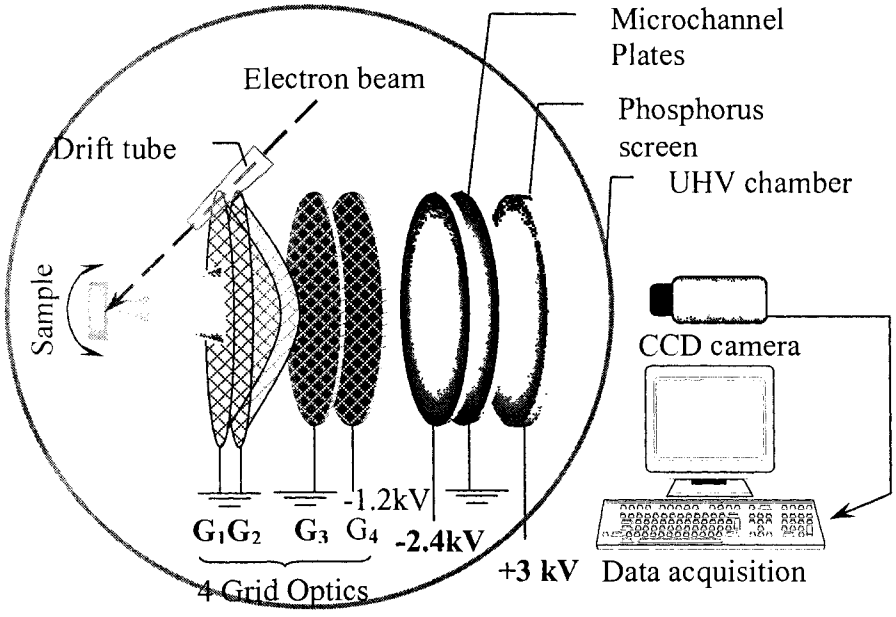

FIG. 6.6. Experimental block diagram for ESDIAD system using CW electron gun.

The sample is rotated about the vertical axis, and the patterns are displayed using micro-channel plates (MCP) with flurescent screen. The active area of the MCP is about 40 mm, as shown in Fig. 6.7., and the typical potential grids are $G_1 = G_2 = 0$ V (for spherical grids), $G_3 = 0$ V and $G_4 = -1$ kV (for plane grids). The MCP was connected as a positive ion detector assambly in imaging mode; MCP entrance voltage was -900 V and the outer one is grounded; the phosphour screen was about +2.0 kV; and the electron gun filament potential is 1 kV.

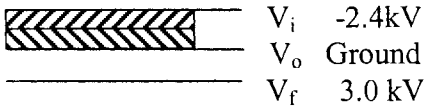

Fig. 6.7. Positive ion detector (Chevron assembly) in imaging mode with phosphorus screen.

The apparatus was prepared to observe the Na^+ ion angular distributions. The e-beam incident at angle near 45^o to the surface normal causes simulated desorption of the ion from adsorbed layer. The desorbed ions pass through high-transparency curved grids, and are accelerated to a chevron assembly microchannel plates (MCP). Ions that strike the first MCP produce a secondary electron signal, amplified by a factor 10^6 at the end of the second MCP, which enough for the qualitative assessment pattern. Since we do not know the threshold electron energy for desorption of Na^+ ions, we scanned the sample with different electron energies ranging between (100 to 1000 V). The real pictures with the image analyzer are shown in Fig. 6.8.

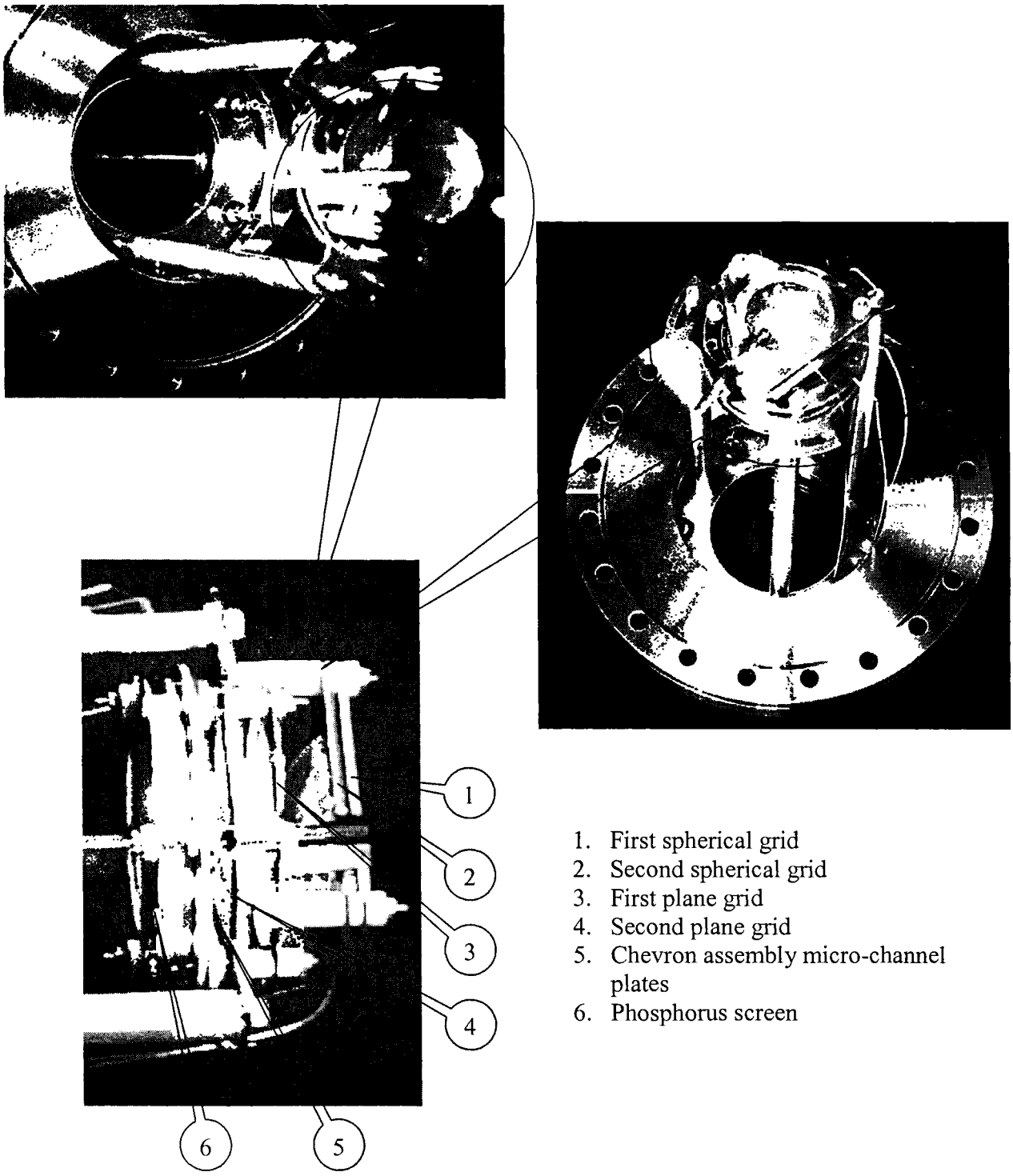

FIG. 6.8. Pictures for ESDIAD image analyzer at PERI, Old Dominion University.

VI.6. Results

In the ESDIAD, atoms are desorbed from the surface of the solid by low energy electrons. These atoms are ejected as a result of a multi-step process which consists of:

(1) Primary energy deposition via the electron collision cascade, which results in excitation within the valance electronic structure of the crystal.[25]

(2) Migration of the primary excitations with simultaneous cooling and self-trapping.[26]

(3) Defect diffusion in the crystal and evaporation of adatom from the surface.[27]

It was found that increasing the voltage on the Grid G_4 increases the intensity on the phosphor screen due to the retardation, which was obtained by shifting the potential of the surface at T (along with grid G_1) relative to the fixed negative potential at the grid G_2, with the ion collector C at the ground potential. The grid G_1 and the grid G_3 serve, respectively, to suppress secondary electron emission from the surface at T and to provide electrostatic screening of the collector C. The high gain of the multiplier compensates for the loss of ions due to the small aperture. The resolution of the apparatus, limited mainly by field distortion in the central region, was found to be 1 eV. The effect of field distortion is not only to broaden the energy distribution but, also, to shift the position of the most probable energy to a lower setting. The characteristic ESDIAD contour patterns for NaCl surface is shown in Fig. 6.9., and the real images in Fig. 6.10. In our example, the inelastic interactions of electrons with the surface crystals result in emission of various particles, such as ions, atoms and molecules. Electron stimulated desorption processes for this class of ionic crystals, namely for alkali halides,

is characterized be a thermal (Mawellian) spectrum of translational energies.[28] For several alkali halides (potassium and rubidium chorides, bromides and iodies) several of the halogen atoms are ejected with non-thermal energies, i.e., energies of the order of 0.1 eV.

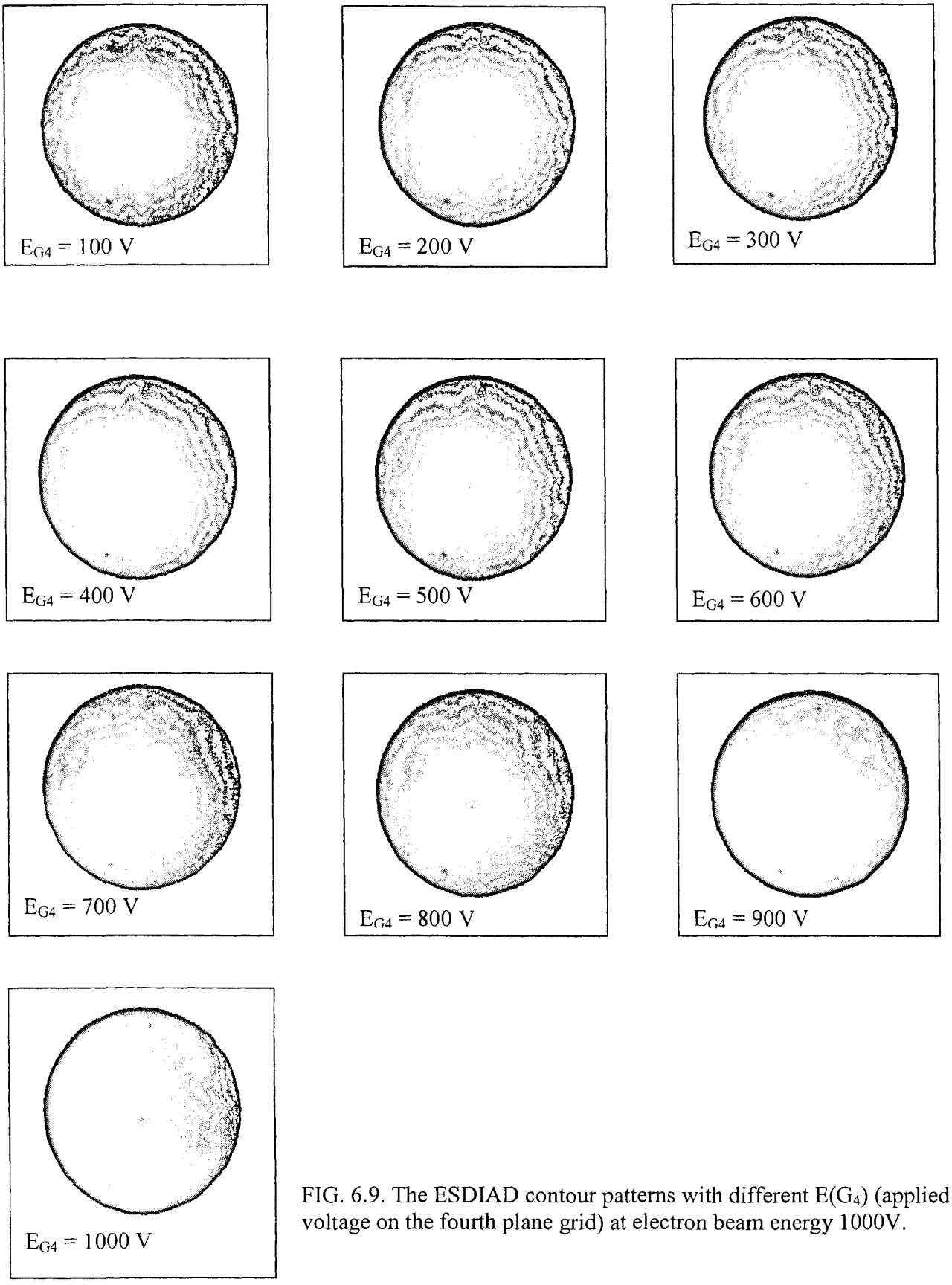

FIG. 6.9. The ESDIAD contour patterns with different $E(G_4)$ (applied voltage on the fourth plane grid) at electron beam energy 1000V.

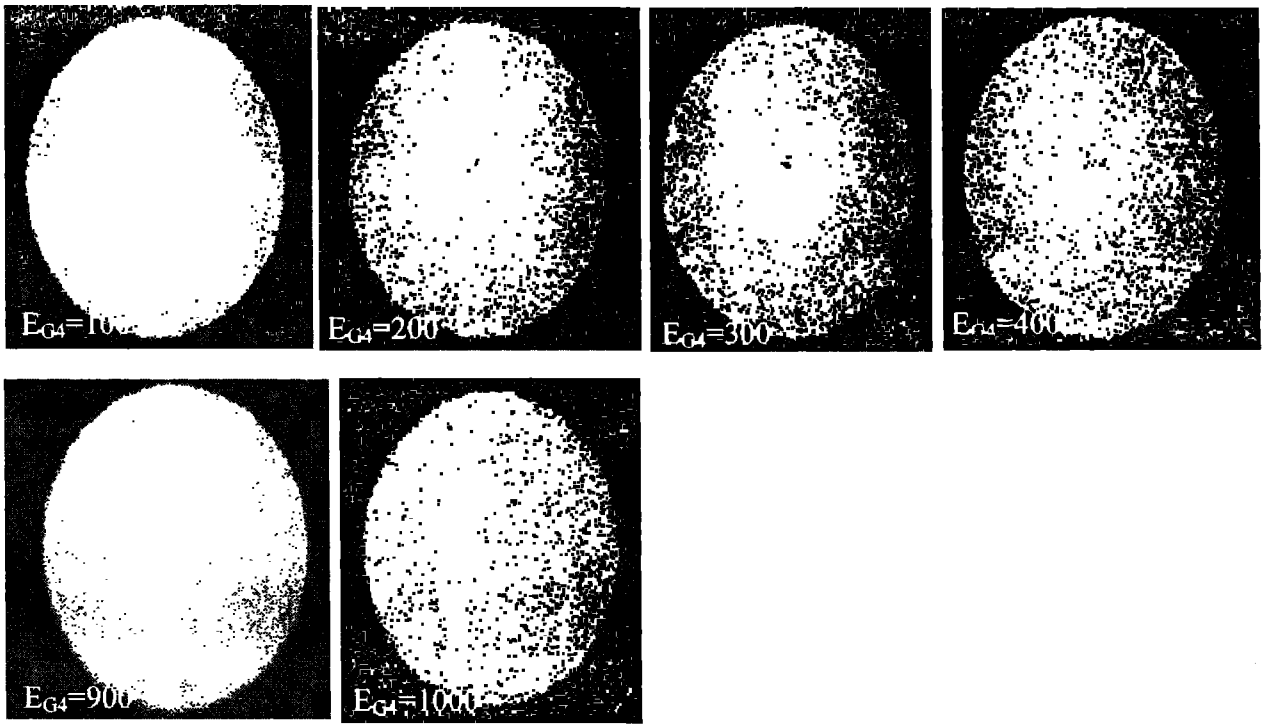

FIG. 6.10. Real time ESDIAD images for NaCl crystal with different E(G_4) volts.

VI.7. Conclusion

In summary, we have demonstrated a technique (ESDIAD) that allows the determination of a positive surface potential of ionic crystals like NaCl under electron irradiation. This technique is also useful for providing qualitative guidance to the construction of structural models of co-adsorption.

VI.8. References

1. R. D. Ramsier and J. T. Yates Jr., "Electron-stimulated desorption: Principles and applications," *Surf. Sci. Rep.* **12**, 243-378 (1991).
2. J. R. Young, "Evolution of Gases and Ions from Different Anodes under Electron Bombardment," *J. Appl. Phys.* **31**, 921-923 (1960).
3. G. E. Moore, "Dissociation of Adsorbed CO by Slow Electrons," *J. Appl. Phys.* **32**, 1241-1251 (1961).
4. D. Menzel and R. Gomer, "Desorption from Metal Surfaces by Low-Energy Electrons," *J. Chem. Phys.* **41**, 3311-3328 (1964).
5. P. A. Redhead, "Interaction of slow electrons with chemisorbed Oxygen," *Can J. Phys.* **42**, 886-905 (1964).
6. P. J. Feibelman and M. L. Knotek, "Reinterpretation of electron-stimulated desorption data from chemisorptions systems," *Phys. Rev. B* **18(12)**, 6531-6539 (1978).
7. M. J. Dresser, M. D. Alvey, and J. T. Yates Jr., "Enhancement of the ESDIAD method for imaging bond directionality in chemisorbed species," *Surf. Sci.* **169(1)**, 91-103 (1986).
8. D. Mocuta, J. Ahner, and J. T.Yates Jr., "Kinetic energy distributions and momentum resolved ESDIAD measurements of CO+ ions and excited neutral CO* molecules – CO/Cu(100)," *Surf. Sci.* **390**, 11-16 (1997).
9. D. Mocuta, J. Ahner, J. -G Lee, S. Denev, and J. T. Yates Jr., "Self-organized nanostructures: an ESDIAD study of the striped oxidized Cu(110) surface," *Surf. Sci.* **436**, 72-82 (1999).

10. S. A. Joyce, A. L. Johnson, and T. E. Madey, "Methodology for electron stimulated desorption ion angular distributions of negative ions," *J. Vac. Sci. Technol. A* **7(3)**, 2221-2226(1989).

11. N. J. Sack, L. Nair, and T. E. Madey, "Adsorption and angle-resolved electron-stimulated desorption of CCI4 on Ru(0001)," *Surf. Sci.* **310**, 63-72 (1994).

12. R. Stockbauer, E. Bertel, E. and T. E. Madey, "The origin of H^+ in electron stimulated desorption of condensed Ch_3OH," *J. Chem. Phys.* **76(11)**, 5639-5641 (1982).

13. N. D. Shinn and T. E. Madey, "Stimulated desorption from CO chemisorbed on Cr(110)," *Surf. Sci.* **180**, 615-632 (1987).

14. K. Ueda and A. Takano, "Time Sequential Measurement of the Precursor State of Oxygen on the Titanium Surface by Means of Time-of-Flight Spectroscopy for Electron Stimulated Desorption," *Jpn. J. Appl. Phys.* **28(12)**, 2594-2596 (1989).

15. I. Arakawa, M. Takahashi, and K. Takeuchi, "Electron stimulated desorption of excited neutrals from the surface of solid rare gas," *J. Vac. Sci. Technol. A* **7(3)**, 2090-2093 (1989).

16. K. Sakamoto, K. Nakatsuji, H. Daimon, T. Yonezawa, and S. Suga, "Electron-stimulated desorption (ESD) of the O2xSi(111) surface," *Surf. Sci.* **306**, 93-98 (1994).

17. S. L. Bennett, C. L. Greenwood, and E. M. Williams, "ESDIAD studies of fluorine and chlorine adsorption at Si(100)," *Surf. Sci.* **290(3)**, 267-276 (1993).

18. J. Ahner, D. Mocuta, and J. T.Yates Jr, "TOF-ESDIAD measurements of a coadsorbate system: CO on an oxidized Cu(110) surface," *Surf. Sci.* **390**, 126-131 (1997).

19. J. J. Czyzewski, T. E. Madey, and J. T. Yates Jr., "Angular Distributions of Electron-Stimulated-Desorption Ions: Oxygen on W(100)," *Phys. Rev. Lett.* **32**, 777-780 (1974).

20. Q. Guo, I. Cocks, and E. M. Williams, "Surface Structure of (1x2) Reconstructed TiO_2(110) Studied Using Electron Stimulated Desorption Ion Angular Distribution," *Phys. Rev. Lett.* **77(18)**, pp.3851-3854 (1996).

21. E. M. Williams and J. L. de Segovia, "Electron stimulated desorption of ions from surfaces: techniques, methodology and some recent findings with water at metals and semiconductors," *Vacuum* **39**, 633-642 (1989).

22. M. Q. Ding and E. M. Williams, "The interaction of electron beams with water admitted at aluminium single crystal (100) studied by ESD and AES," *Surf. Sci.* **160(1)**, 189-204 (1985).

23. T. E. Madey, "Electron- and Photon-Stimulated Desorption: Probes of Structure and Bonding at Surfaces," *Science* **234**, 316-322 (1986).

24. T. E. Madey, "Ion angular distributions in electron stimulated desorption: Adsorption of O_2 and H_2 on W (100)," *Surf. Sci.* **49(2)**, 465-496 (1975).

25. J. Kolodziej, P. Piatkowski, and M. Szymonski, "Electron-stimulated desorption of thin epitaxial films of KBr grown on (100) InSb," *Surf. Sci.* **390**, 152-157 (1997).

26. R. T. Williams, K. S. Song, W. L. Faust, and C. H. Leung, "Off-center self-trapped excitons and creation of lattice defects in alkali halide crystals," *Phys. Rev. B* **33(10)**, 7232-7240 (1986).

27. Z. Postawa and M. Szymoński, "Directional emission of nonthermal halogen atoms by electron bombardment of alkali halides," *Phys. Rev. B* **39**, 12950-12953 (1989).

28. M. Szymonski, J. Kolodziej, Z. Postawa, P. Czuba, and P. Piatkowski, "Electron-stimulated desorption from ionic crystal surfaces," *Prog. Surf. Sci.* **48**, 83-96 (1995).

APPENDIX A

RHEED EXPERIMENT

The time-resolved reflection high energy electron diffraction (RHEED) experiment at PERI, Lab 106 is consisting of three parts:

1. Laser system.
2. Ultra-High Vacuum system.
3. Data acquisition.

A.1. Laser system:

Before you start working with the laser system, be sure to fulfill all safety precautions and requirements to work with the Class 4 laser. Be sure to read and have a copy of the Laser Safety Operating Procedures (LSOP). A hard copy of the LSOP is always attached to the optical table.

In the laser setup, the fundamental laser beam (Nd:YAG, λ = 1064 nm, FWHM = 100 ps) is split into two beams, the first is amplified and interacts with the surface sample at near normal incidence. The second is frequency quadrupled to the ultraviolet (λ = 266 nm) and incident on the electron gun photocathode.

The laser system consists of a Nd:YAG oscillator (QUANTRONIX, series 4000), Nd:YAG regenerative amplifier (Home made), and one-pass Nd:YAG amplifier (Kigre model LCS-500). The oscillator operates at 76 MHz with 17 Watts and 1064 nm wavelength output. The regenerative amplifier is injected by the oscillator and can be run in two modes. The first mode is running at 800 Hz (with ~ 0.6 mW per pulse) and the

second mode is running at 50 Hz (with ~ 20 mW per pulse). Laser optical path is shown in the Fig. A.1. Laser equipments are shown in Fig. A.2.

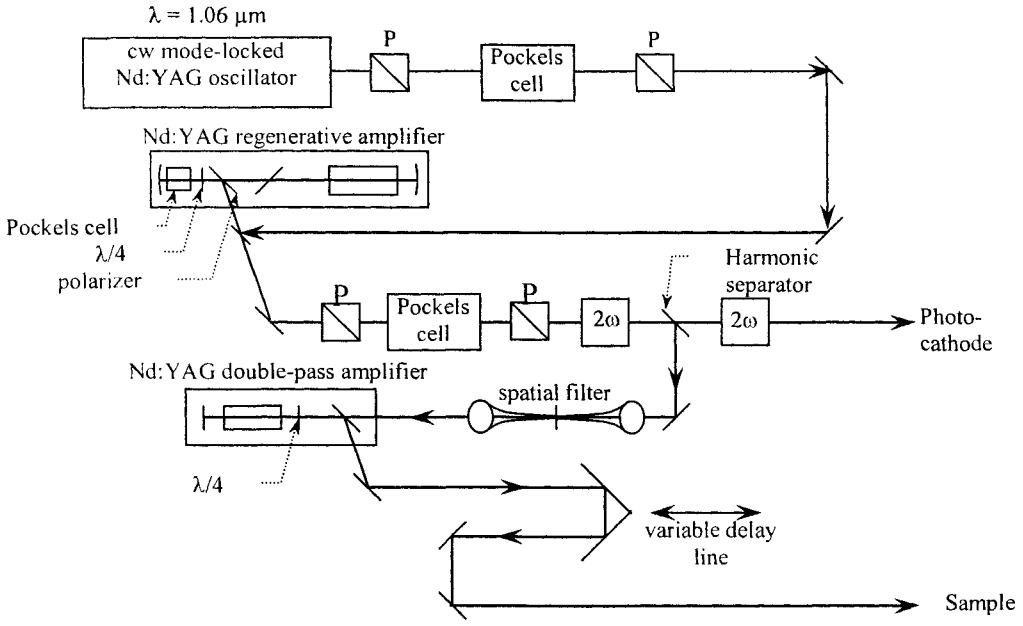

FIG. A.1. Schematic diagrams of the laser system driving the 100 ps pump probe apparatus.

Laser Specifications:

Oscillator

Type: Neodymium YAG (Nd:YAG)

Manufacture: Quantronix Corp. (http://www.quantron.com/)

41 Research Way, East Setauket, New York-11733

Phone: (631)784-6100

Fax: (631)784-6101

Model: 416 Lasers

Class: 4

Wavelength: 1064 nm and 532nm (Second Harmonic Operation)

Pulse width: 100 ps

Pulse energy: 2.07 mJ

Repetition rate: 82 MHz

Regenerative amplifier

Type: Neodymium YAG (Nd:YAG)

Manufacture: Home Made.

Model: 416 Lasers

Class: 4

Wavelength: 1064 nm and 532nm (Second Harmonic Operation)

Pulse width: 20 ps

Pulse energy: 1 mJ

Repetition rate: 800 Hz

One-pass amplifier

Type: Neodymium YAG (Nd:YAG)

Manufacture: Kigre Inc. (http://www.kigre.com/)

100 Marshland Road, Hilton Head Island,

SC-29926

Phone: (843) 681-4066

Fax: (843) 681-4559

Model: RCS-3000

Class: 4

Wavelength: 1064 nm

Pulse width: 120 ps

Pulse energy: 25 mJ

Repetition rate: 50 Hz

Operation:

Laser system can be run in two modes. Before you run the laser, check the two water chillers in the back and be sure there is no water leak and that the water level is at normal position.

Laser procedure for 800 Hz:

1. Start the refrigerated recirculation.
2. Switch on the cooling water of the oscillator, regenerative amplifier, Pockels cell, and the one pass amplifier.
3. Turn on the RF power supply for the oscillator (turn the key two steps).
4. Turn on the power for oscillator, regenerative amplifier, Pockels cell driver.
5. Let the system warm up for 20 minutes
6. Fire the regenerative amplifier.
7. Start lasing the oscillator.
8. Turn on the high voltage of the Pockels cell.
9. Now the laser is running at 800 Hz.

Run the laser system at 50 Hz:

1. Connect the output of the digital delay generator to the "Delay 1 In" of the RF driver for the Pockels cell.

2. Turn on the digital delay generator.
3. Turn on the photodiode to trigger the digital delay generator.
4. Fire the one-pass amplifier.
5. Now the laser is running at 50 Hz.

Results: 1.1 watt, 22 mJ @ 2100 V applied on Kigre where delay time was T+125 μs.

Laser maintenance:

Always check the water level in every chiller before you run the laser. Every once in a while, depending on the laser type, check the laser operation hours of the flash lamps for the laser system. Maintain the normal operation hours for the flash lamps guarantee the laser stability and the laser power.

Suppliers and contact information:

Cascade laser Corp.

101 N. Elliott Rd., Newberg, OR-97132

Phone: (503) 554-1926

Laser lamp, regenerative amplifier # LLQ117X-E

& oscillator #LL116X-E

KIGRE, INC.,

100 Marshland Road, Hilton Head, SC-29926

Phone: (843) 681-5800

Fax: (843) 681-4559

E-mail: info@kigre.com

Laser lamp # K304

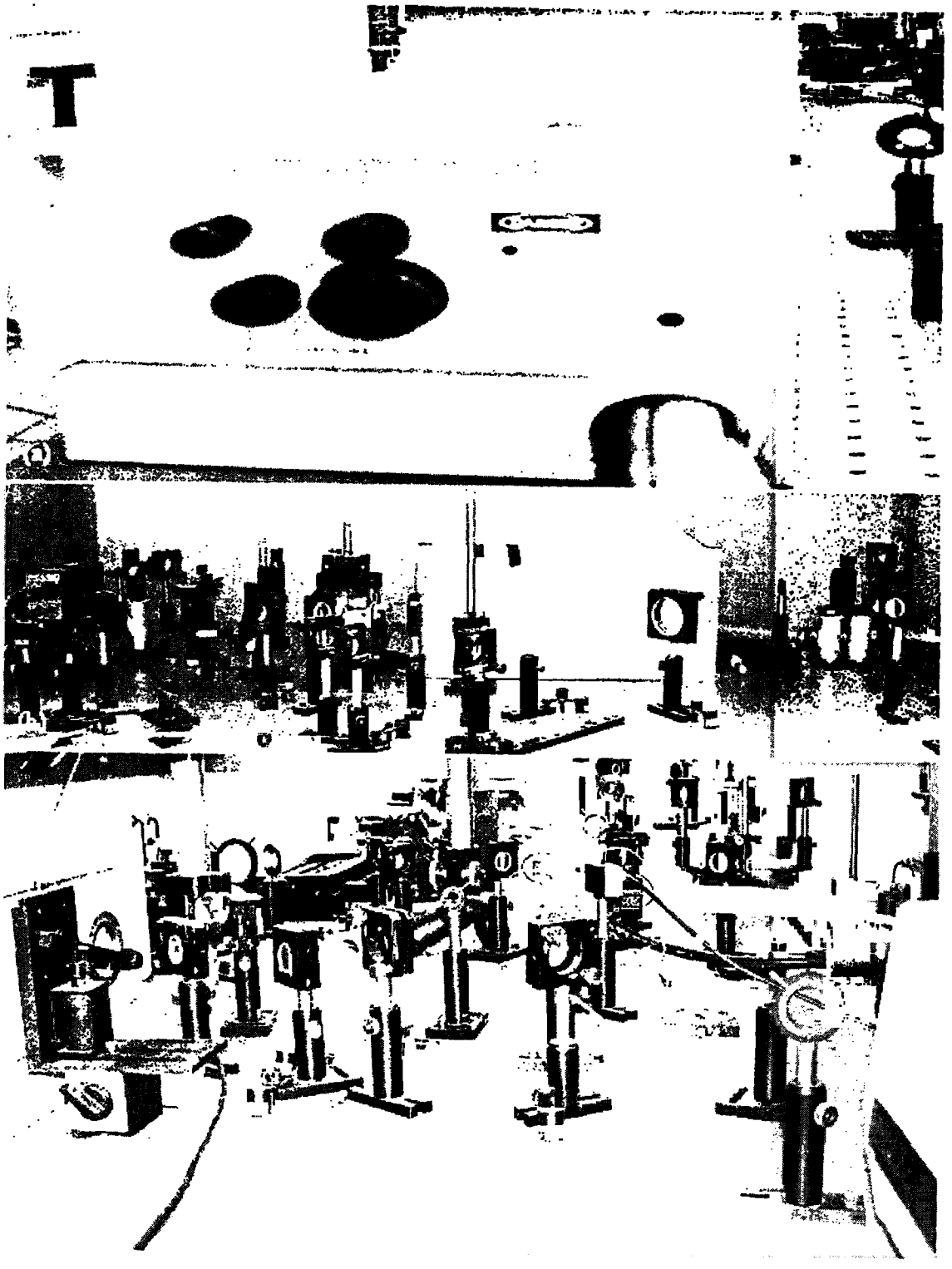

FIG. A.2. Three parts of a 100 ps laser system (a) Oscillator, (b) Regenerative amplifier, and (c) One-pass amplifier.

A.2. UHV system

There are some necessities in order to work in the UHV system, such as special materials to be used in the vacuum system, extreme cleanliness to maintain the vacuum system, and baking of the entire system to remove water vapor and other trace gases that adsorb on the chamber's surface.

Accomplish the UHV

Some steps are required to reach the UHV, as following:

1. High pumping speed system, in our case we used multiple vacuum pumps in a series, starting with mechanical pump (atmospheric to 10^{-3} torr), turbo-molecular pump (~ 10^{-6} torr), and ion pump (~10^{-9} torr), shown in Fig. A.3.
2. Clear and high conductance tubing to pump, short and straight without obstruction as possible.
3. Low out-gassing materials such as stainless steels, tantalum, molybdenum and tungsten. If you have to use cupper, be sure to use the cured type.

Use low vapor pressure materials (ceramics, glass, metals, teflon if unbaked), bake the system (~250 °C to 280 °C) to remove water or hydrocarbons adsorbed to the walls while vacuum pumps are running.

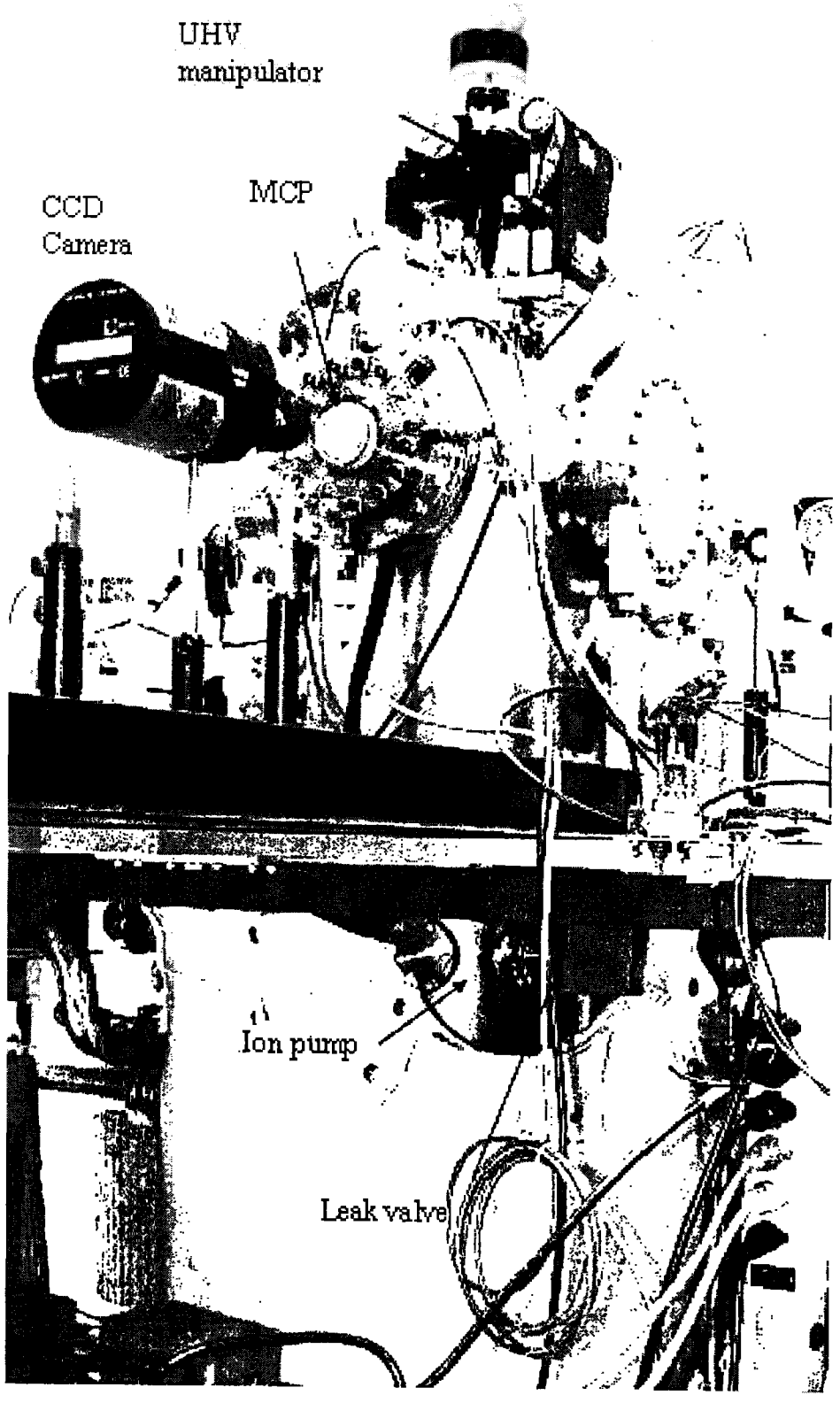

FIG. A.3. UHV chamber contains RHEED system, MCP, Photoactivated electron gun.

Operation:

Pump up procedure:

1. Confirm the chamber is properly sealed.
2. Start the mechanical pump, and then the turbo pump, wait until the turbo controller reaches the maximum speed.
3. Monitor the turbo pump current, temperature, and power readings.
4. When the turbo reaches maximum speed, open the ion pump isolation valve.
5. Check the digital gauge meter. When the pressure drops lower than 10^{-5} torr, start backing the chamber to turbo.
6. While backing process degas the sample by keeping the sample's temperature above 280 °C.
7. After 10 hrs stop the backing. Now you should be able to reach 10^{-8} torr.
8. Close the valve to the turbo. Start the ion pump.
9. Backing the system for 10 hrs to the ion pump.
10. Now, the pressure should be able to reach lower 10^{-9} torr.

Pump down procedure:

1. Be sure the sample is at the room temperature.
2. Do not vent the chamber if the manipulator, or sample holder are still warm. Wait at least 2 hours after blowing out the nitrogen.
3. Vent the UHV chamber to dry nitrogen by the following procedure: turn off all filaments, ion gauges, RHEED electron guns and ensure the sample is at room

temperature. Isolate the ion pump by closing the valve. At present, the chamber has to be rough pumped through the turbo pump. Therefore, the turbo pump must be turned on during pump-down. Open the valve between the turbo pump and the chamber. Wait until the pressure goes up to 10^{-4} torr. Turn off both the turbo and roughing pumps. Slowly and manually open the leak valve (if it is not automatically opened) followed by roughing out the chamber by using the mechanical pump.

Bakeout procedure on turbo pump

Ensure there are no leaks, prepare for bakeout as follows:

1. Remove all cables except for the ion gauge and titanium sublimation pump (TSP) cables which are bakeable and should remain on during the bake.
2. Remove the connecting cable from MCP flange.
3. Do not bake leak valves tightly closed.
4. Before covering up the system with the bakeout shrouds or IR lamps, check that the heater tapes all work by turning on the bakeout for a few minutes.
5. Be aware that there are two parts in the chamber for backout. The lower part which has the ion pump and TSP, and the upper part which has the manipulator, MCP, ion gun, and photoa-ctivated electron gun.
6. For the lower part you need to disconnect the high voltage power for the ion pump and turn on the heater from the main distribution panel that is attached to the ion pump system controller. On the main controller panel press the bake key twice, and you will notice the red LED turn on for bakeout.
7. For the upper part use the heater tapes or IR lamps around the chamber parts.

8. After bakeout the various filaments and the sample will need to be degassed.
9. The ion gauge can be degassed before turning off the backout. Press degass key on the ion gauge controller.
10. Re-connect the cables to the ion gun, electron gun.

Degas the Argon ion gun:

Ensure the emission control is turned down fully. Set beam energy to 0.5 kV. Turn on the unit and allow 1-2 minutes for the unit to warm up. Gradually increase the emission control current to 20 mA. Switch on the beam energy toggle switch. Leave to degas at this value for 5 minutes.

Degas the electron gun:

Ensure that the applied voltage is fully wound down and off. Turn on the unit. Wait 2 minutes for the unit to warm up. Slowly increase the potentiometer to 4 kV. If there is any sign of breakdown (needle flickers or arcing) immediately turn off the unit.

Degas the TSP:

On the control panel turn the mode knob to cycle mode. Keep the cycle length at 2 minutes. Set the filament current to 30 A.

Bakeout procedure on ion pump.

Repeat all the above steps while the ion pump is on and the turbo is off.

The UHV chamber contains:

1. Argon ion gun.
2. Reflection photo-activated electron gun
3. Heating stage.
4. Microcahnnel plate (chevron type).

Argon ion bombardment:

1. Be sure you backout the chamber before you use the argon ion bombardment, and the pressure reached 10^{-10} torr.
2. Degas the sample by heating it before ion bombardment.
3. Position the sample in front of the sputter gun around 80 degree where the ion beam is perpendicular to the surface of the sample.
4. Flash the STP at 55 A for 2 minutes and then turn off the ion pump.
5. Carefully open the Ar leak valve to leak in the Ar gas until the pressure reaches 10^{-5} torr.
6. Set the ion gauge emission to 20 mA. With the beam energy switch in the off position and the emission control at its minimum setting, turn on the unit and allow 1-2 minutes for it to warm up. Gradually increase the emission control to 20 mA. Switch on the beam energy toggle switch.
7. The bombardment time varies with the sample, the ion energy, and the current you used.
8. The sample can be kept at high temperature or at room temperature during bombardment.

Reflection photo-activated electron gun

Inside the chamber, the type of photoactivated electron gun works in reflection mode. The idea is shining the UV light by 30° incident angle normal to the photocathode. A zinc sheet of 0.2 mm thickness and 1 inch in diameter was used as a photocathode. A 20 kV is applied to the photocathode. The schematic diagram for the electron gun is shown in Fig A.4.

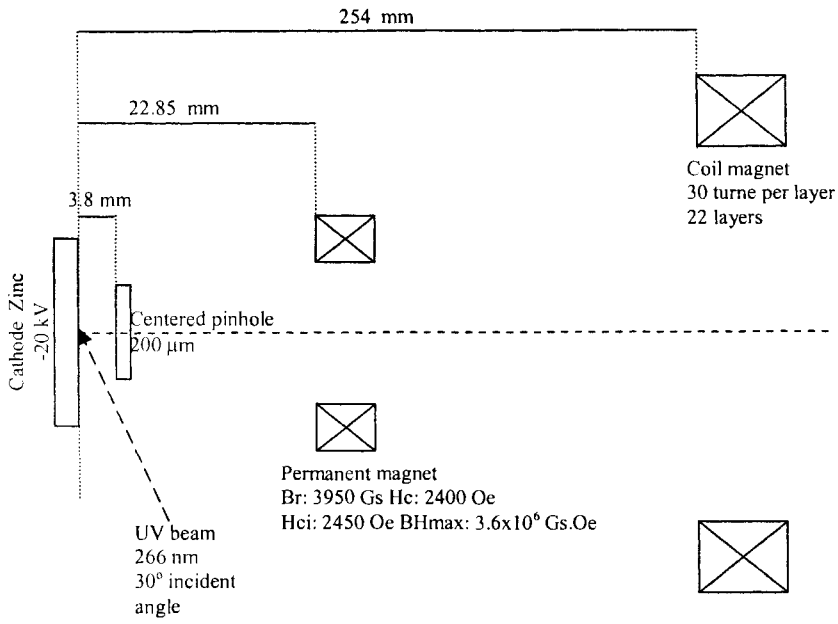

FIG. A.4. Configuration of reflection photo-activated electron gun.

Operation:

1. Slowly apply the voltage to the cathode, do not exceed 20 kV.
2. Align the UV beam through the optical window until you see the strongest beam spot on the MCP.
3. Use the deflection coil to pull the electron beam to the center of the screen.

4. Apply the current to the focusing magnetic coil until you get the focused spot.
5. Slightly align the coil until you get back the spot into the center of the screen.
6. Change the deflection coils current to move the electron beam to the sample, scan the sample to get the RHEED pattern.

Microchannel plates:

Microchannel plates (MCP) are high gain, fast response, and spatially resolved signal amplifiers for particle collisions. They can be triggered by UV, X-ray photons, positive and negative ions, electrons, and fast neutral particles. The amplification can reach as high as 10^6 depending on the applied voltage. Before you work with the MCP you need to read the entire start-up procedures before applying any voltages, refer to diagram in Fig. A.5 for typical wiring for different detection mode.

Caution:

1. Do not exceed 1000 V per MCP for 40:1 asped ratio; in chevron type (2 MCPs) do not exceed 1800 V in total.
2. When installing flange mounted gradually tighten the bolt in star pattern.
3. For optimal lifetime, operate the detector at the minimum voltage necessary.
4. Do not exceed 3000 V on the phosphor screen for the single MCP, and 5000 V for the chevron type.
5. Do not run the MCP at pressure higher than 10^{-5} torr.

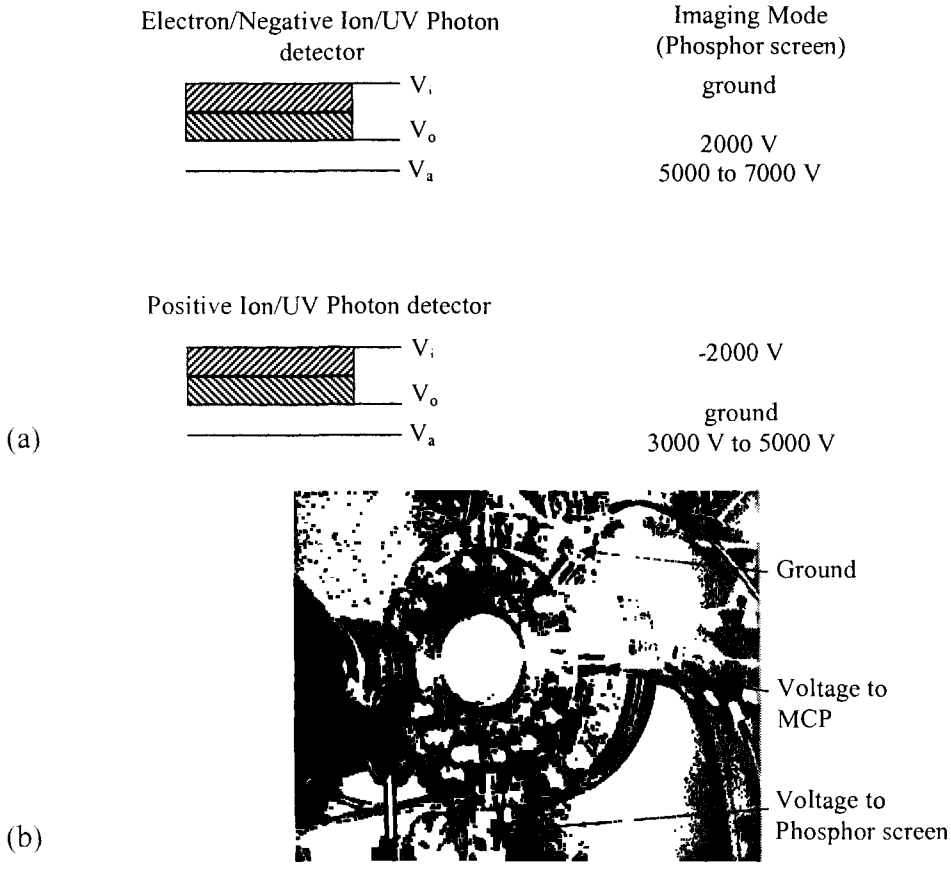

FIG. A.5. MCP wiring diagram (a) for different modes, (b) voltage-apply configuration for electron capture detector.

Contact information:

Burle industries, Inc.

1000 New Holland Avenue, Lancaster,

PA-17601

Phone: (800)366-2875, (717)295-6888

Fax: (717)295-6096

Email: burlecs@burle.com

A.3. Time-resolved RHEED camera detector

Specifications:

Model PIXI 1024,

Image array: 1024 x 1024, 13 μm x 13 μm pixels

Imaging area: 13.3 x 13.3 mm

Mount: adjustable c-mount with integral 25mm shutter.

Cooling: Air-cooled system with cooling temperature (-80 °C typical; -70 °C, +20 °C ambient).

Connectors:

- USB 2.0: control signals and data are transmitted between the camera and the host PC via the USB port.
- Shutter: LEMO connector provides the shutter drive pulses for driving and external shutter.
- LOGIC OUT: 0 to 3.3 V logic output (TTL-compatitable)
- EXT SYNC: 0 to 3.3 V logic output (TTL-compatitable) that has a 10 kΩ pullup resistor.
- Fan: Air-cooled camera contains an internal fan.

Operation / acquiring data:

1. Once the camera has been installed, turn on the power supply then run the winview/32 program.
2. Setup the detector temperature. The default temperature setting is reading from the camera.

3. When the array temperature reaches the set temperature, the dialog box will report that the temperature is locked.
4. Select focus from the acquisition menu.
5. Adjust the lens aperture, intensity scaling, and focus for the best image as viewed on the monitor.
6. To get the best clear images do the following:
    - Begin with the lens blocked off and then the lens at the smallest possible aperture (large f-number) and use a suitable target for test.
    - Adjust the intensity scaling (use 5%-95% button) and adjust the lens aperture until suitable setting.
    - Set the focus adjustment of the lens for maximum sharpness in the viewed image.
7. After adjusting the focus, switch to acquire mode and start saving the data.

Contact information:

Princeton Instruments-Acton

3660 Quakerbridge Road,

Trenton, NJ-08619

Phone: (609)587-9797

Fax: (609)587-1970

Web: www.piacton.com

e-mail: moreinfo@piacton.com

Appendix B: A brief description of the photo-activated electron gun in pico and femtosecond time resolution

A photo-activated electron gun is designed, assembled, and tested in the surface science laboratory at the Physical Electronic Research Institute (PERI) at Old Dominion University. This electron gun is capable of generating and accelerating an electron beam with pulse duration as short as 2.5 ps and electron beam diameter 400 μm at the screen. Replacing the focusing electro-static lens to an electro-magnet one shows an improvement in the beam's intensity and focus. A computer simulation trajectory (SIMION code) has been performed.

The improvements on mode-locked lasers, that lead to the generation of ultra short pulses of few femtosecond duration[1] and the Attosecond temporal resolution streak cameras,[2] lead to an improvement in most surface science techniques, such as RHEED. The increasing dependence is related to the development of new techniques for measuring in sub-picosecond and femtosecond time domain. These techniques are based on recording the images over extremely short exposure times to be able to study the fast developing effects. To meet our goal in getting a high-speed photography system, we have designed and built a fast photo-activated electron gun.

Through our literature review for femtosecond electron guns design, we found that any proposed design will need to account for certain requirements; namely,

- Reducing the initial energy distribution of the photoelectrons to be 0.1 eV or less by choosing a proper combination of photocathode and laser wavelength.
- Enhancing the electric field near the photocathode to be higher than 7 kV/mm.

- Designing a suitable electron focusing lens with temporal dispersion as small as possible.
- Using a traveling wave deflector which reduces the fringe field to the minimum.

The space charge effect plays an important role in both temporal resolution and dynamic range for femtosecond streak image tubes. In order to reduce the temporal dispersion, that is limited mainly by the electric field near the photocathode Degtyareva *et al.*[3] introduced a temporal dispersion compensating element so that the total temporal dispersion can reach 50 femtosecond or less.

The design of a cylindrically symmetric lens with a temporal compensating element, a traveling wave deflector, and a phosphor screen is shown in Fig. B.1. The temporal resolution was evaluated in terms of temporal spread function. In this calculation[3] the electric field of 8 kV/mm at the photocathode, and streak speed of $3x10^5$ cm/sec were used, as shown in Fig. B.2.

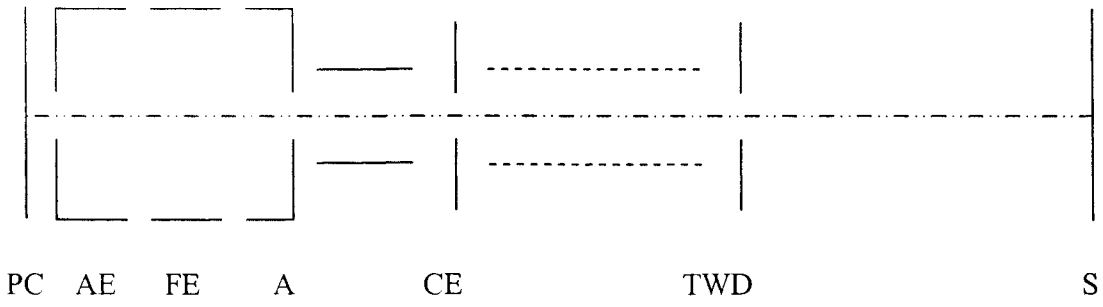

PC: Photo-cathode AE: Accelerator electrode FE: Focusing electrode A: Anode
CE: Compensating element TWD: Traveling wave delector S: Screen

FIG. B.1. The diagram of femtosecond streak image tube after ref. [3].

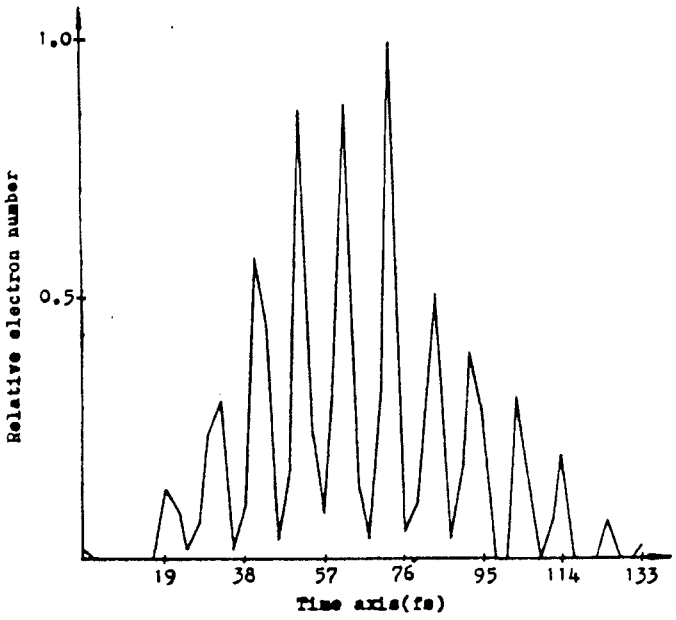

FIG. B.2. Temporal spread function of femtosecond streak image tube.[3]

SIMION code

The basic configuration of the electron gun for simulation using SIMION code is shown in Fig. B.3. The voltages of the photocathode and pinhole (200 μm) electrode are -25 keV and 0 keV, respectively. We also used a permanent magnet with a magnetic field of about 800 Gauss and a magnetic coil with a magnetic field of about 500 Gauss to confine and focus the electron beam to be along the axial direction. The diameter of the system is about 50 mm. The energy spread of the electron on the surface of the photocathode is assumed to be 0 ~ 0.5 eV, and the electrons are emitted over a range from 0 to 40 degrees from the normal. In the procedure of simulation, the number of

electrons emitted from the surface of the photocathode are 101, and the incident laser pulse on the surface of the photocathode has a duration of about 2.5 ps.

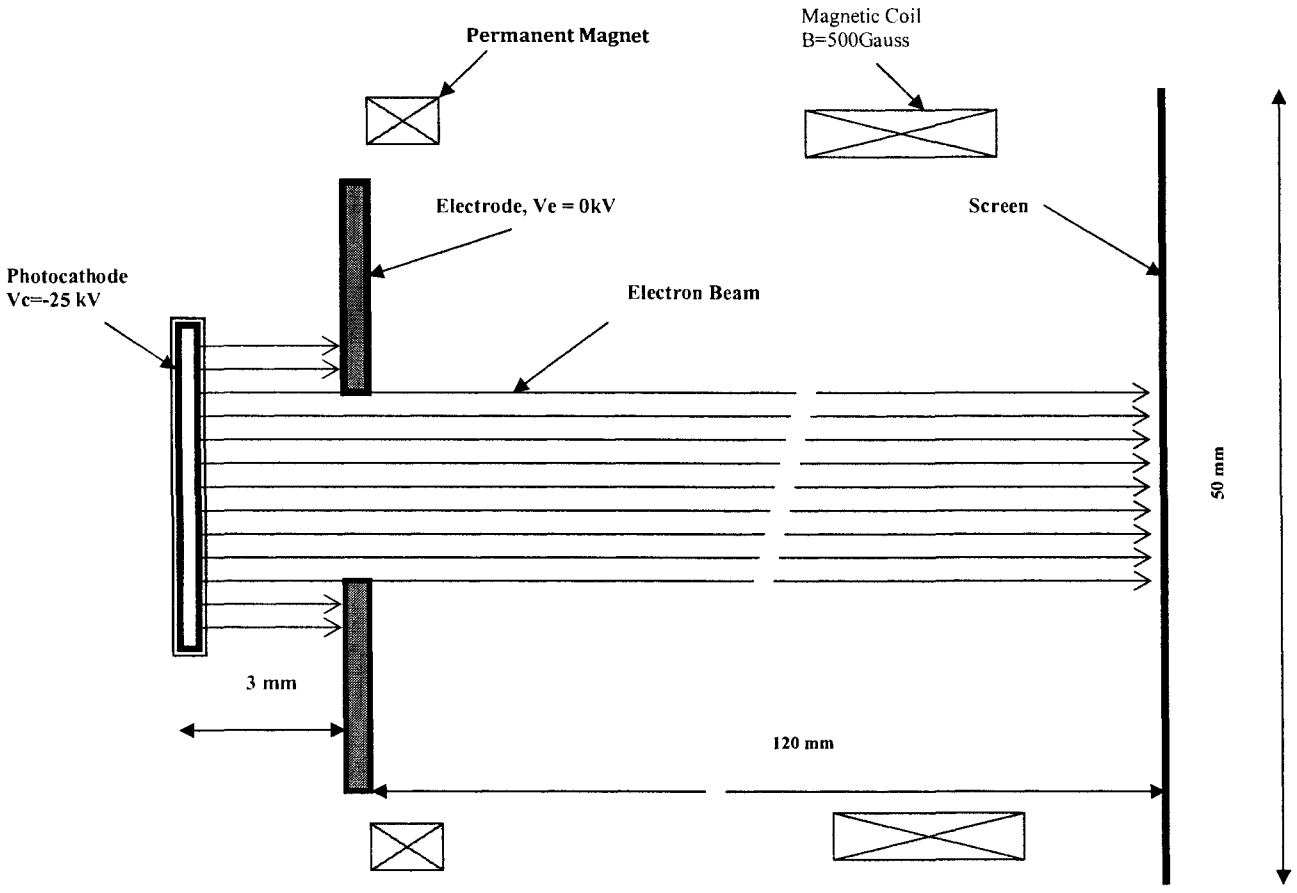

FIG. B.3. Electron trajectory of the photo-activated electron gun.

The simulation results are as follows, the flying time from the photocathode to the screen is about 1351 ps, the final kinetic energy of the electrons is 24998 eV, and the axial velocity of the electrons is about 7.37×10^9 cm/s. In addition, the simulation results of the electron trajectories indicate that the electron pulse duration is about 2.5 + 0.3 = 2.8 ps. The diameter of the electron beam is about 400 μm.

Instrumentation

Four primary requirements should be covered in the design of a femtosecond electron gun. These requirements are:

1. Fast photocathode from which the electrons are emerged with narrow energy distribution.
2. An electron-optical lens arrangement that provides optimized temporal and spatial characteristics.
3. High sensitivity wave-traveling deflector geometry.
4. Phosphor screen that has optimum quantum efficiency.

To generate the required electron beam, two types of photocathodes have been chosen, metal photocathode and semiconductor photocathode. Although semiconductor photocathodes have higher quantum efficiency, they have disadvantages which are: their lifetime is relatively short, they need a good vacuum (about 10^{-10} torr) and they will not survive with a high power laser. The metal photocathode has been tried because it has a long lifetime and can endure hostile environments, but the work function is high,[4] which leads to low quantum efficiency that required UV photons for linear photoemission.

Searching for a metal photocathode element led us to choose from three elements, Gold, Silver and Aluminum. Although, Al has a low work function (~ 4.06 eV) compared to Ag, and Au, it is easy to cover with an Al_2O_3 layer which has a work function higher than that for the UV source. The previous work for photoelectron gun with Ag has been studied,[5] and this work shows that the optimum thickness with electron yield occurs with 250 ′ thin film thickness.

In an attempt to increase the electric field near the photocathode, we have modified the photocathode preparation technique and the way the photocathode is mounted. Two new evaporation methods were tested. The first is using 1" diameter sapphire window, a difference that eliminated the arcing problem due to the increase in the uniformity of the applied electric field between the cathode and the anode. The second modification involves attaching the window to the base in such a way as to allow for the continuity of the evaporated film between the base and the window.

The basic problem with the electron gun is the space charge broadening in the low energy region near the photocathode. The obvious solution to this problem is to accelerate the electrons up to a high energy as quickly as possible and not accelerate them during the focusing procedure. This was the technique that Kinoshita *et al* used in order to record their very short electron pulse.[6] However, in order to accomplish this, they relied on magnetic lenses to provide the focusing of the high energy.

The dynamics of electron bunches in sub-picosecond streak tubes have been studied numerically, taking into account space-charge effects and various initial photoelectron energy distributions. Three computing and analytical models (aberra-tional-Lorentz model, the model describing the limiting case of zero initial energy and simple analytical model) were used.[7]

The spread of photoelectron energies and trajectory displacements due to Coulomb repulsion effects are the main factors limiting spatial/temporal resolution in sub-picosecond and femtosecond streak image tube. However, using the combined aberrational-Lorentz method decreases requirements on the accuracy of the integration of the trajectory equations and increases the number of trajectories.[8]

The electron gun construction, as shown in Fig. B.4, is mounted on 4.5″ CF stainless steel flange, with an outer diameter of about 1″ and the length of 2.5″. All of the parts are made from aluminum cylindrical tubes. Ceramic balls are used as spacers between the photocathode and the anode. Two magnetic lenses are used. The first focus magnetic lens (permanent magnet with 800 Gauss to collimate the electron beam) has a focal length of about 19 mm, and the second magnetic focusing coil has 500 Gauss. The photocathode, a 250Å silver thin film evaporated on Sapphire window, is prepared by thermal evaporation in another chamber and is exposed to 10 min of UV light before it is installed in the electron gun. The distance between the plane anode and the photocathode is 3 mm and the voltage of 25 kV is applied between them according to accelerating electric field 8.3 kV/mm.

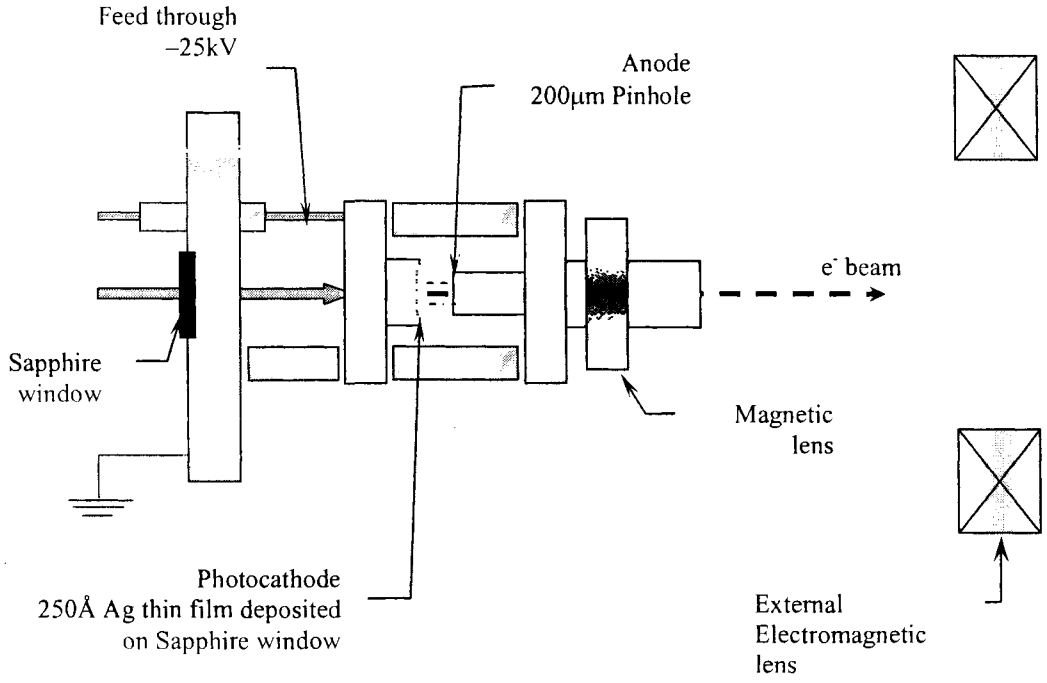

FIG. B.4. Schematic diagram for transmission photo-activated electron gun.

Dynamical operation

The electron gun test was done in an UHV chamber using a mode-loked Nd:YAG laser (λ = 1.06 μm). The frequency quadrupled output from nonlinear crystal at λ = 0.266 μm is used to irradiate the Ag photocathode to generate photoelectrons. Applying electric field between the cathode and the anode accelerates these electrons. Two magnetic lenses are used to collimate and focus the electron beam. The beam spot was detected using Micro-channel plates with phosphor screen, and measured by a CCD camera. The beam spot size was 0.37 mm full width at half maximum (FWHM). The 3-D plot for electron beam spot and the line profile are shown in Fig. B.5.

New ideas could be applied to a photocathode to enhance its properties such that the quantum efficiency can be increased and the lifetime can be extended.

These ideas are:

1. Ion-implanted photocathode: this is done by implanting Cs ions to a certain depth of metal, for example, 30 nm, which is about the mean free path of visible light in metal. It has the advantages of both a metal photocathode and a semiconductor photocathode, such as high quantum efficiency, long life, low work function, and high damage threshold. The photoelectrons can be generated by the green laser in this case.
2. Using alkali material with a high response time and a low work function such as magnesium (~ 3.66 eV). The photocathode can be coated with a thin layer of gold for protection (less than 50 Å).

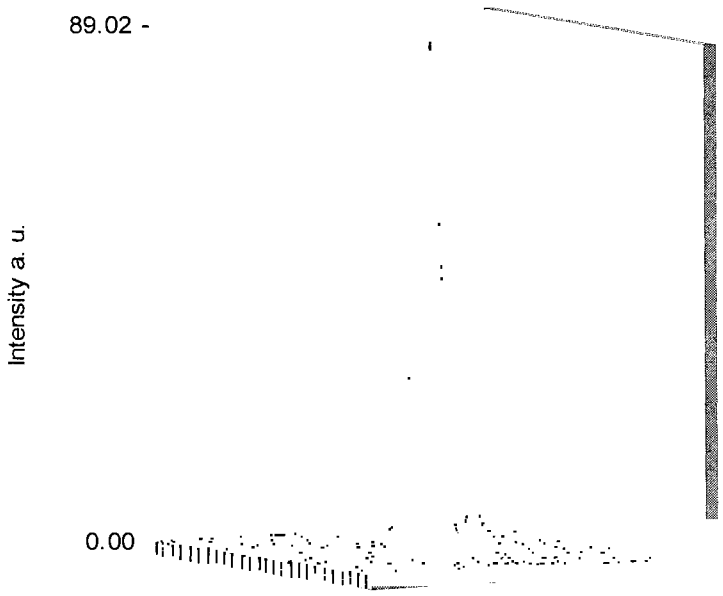

a)

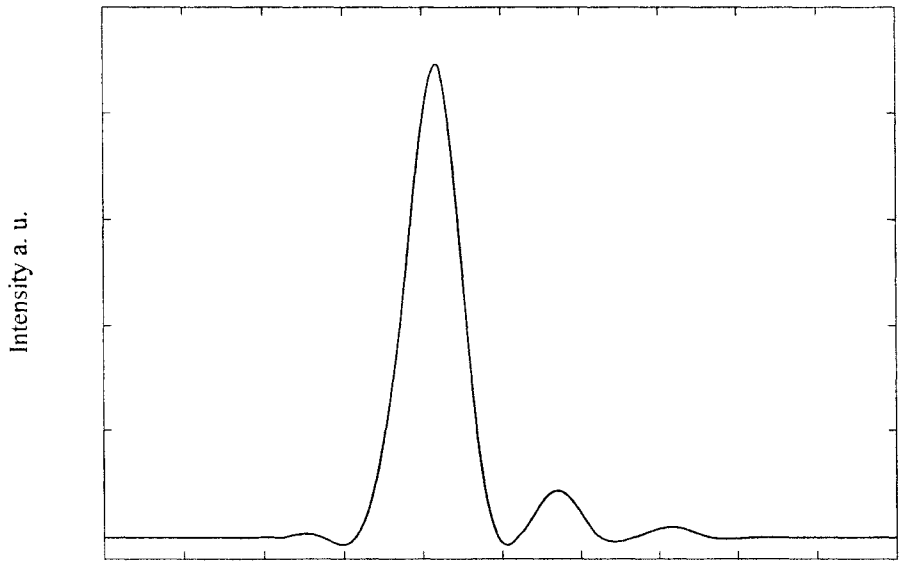

b)

FIG. B.5.Electron beam spot at 20 keV where FWHM is 0.37 mm a) 3-D electron beam spot. b) Line profile for the beam spot.

Conclusion

In order to design a femtoscecond electron gun, a few requirements should be taken into account; namely,

- use a proper kind of photocathode with an initial energy spread of 0.1 eV and a response time of 10 fs or less.
- apply an electric field of 8 keV/mm or higher to the photocathode.
- use a suitable electron optical focusing lens that is capable of dealing with strong discrete space charge effect
- use a suitable temporal dispersion compensating element
- use a traveling wave deflector with a wide bandwidth and phase velocity that is matched with the electron beam.

References:

1. M. Kovalsky, A. Hnilo, A. Libertun, and M. Marconi, M., "Bistability in Kerr lens mode-locked Ti:sapphire lasers," *Opt. Commun.* **192**, 333-339 (2001).
2. J. Itatani, F. Quéré, G. Yudin, M. Ivanov, F. Krausz, and P. Corkum," Attosecond Streak Camera," *Phys. Rev. Lett.* **88**, 173903 1-4 (2002).
3. H. Niu, V. Degtyareva, V. N. Platonov, A. M. Prokhorov, and M. Schelev, *SPIE* **1032**, 79 (1988).
4. A. Finch, Y. Liu, H. Niu, W. Sleat, D. Walker, Q. Yang, and H. Zhang, *SPIE* **1032**, 622 (1988).
5. M. Aeschlimann, E. Hull, H. E. Elsayed-Ali, and M. Scheinfein, "A picosecond electron gun for surface analysis," *Rev. Sci. Instrum.* **66**, 1000-1009 (1995).

6. K. Kinoshita and Y. Suzuki, "High Speed Photo and Potonics," *Proc. of the 13th Int. Cong.*, Tokyo, (1987).

7. M. A. Monastyrski, "Some dynamic problems in streak image tubes theory," *Nucl. Instr. and Meth. A* **363**, 354-357 (1995).

8. M. A. Monastyrski, V.P. Degtyareva, M.Ya. Schelev, and V.A. Tarasov, "Dynamics of electron bunches in subpicosecond streak tubes." *Nucl. Instr. and Meth. A* **427**, 225-229 (1999).

APPENDIX C

SAMPLE PREPARATION

In this work the removal of the native oxides from the Si(111) and Ge(111) surfaces by hydrofluoric (HF) acid based etch treatments was used. A cyclic of HF and water rinse procedure was repeated at least two times before loading the samples into the UHV chamber. This method is an effective surface oxide removal treatment. In this part, effective recipes for cleaning the silicon and the germanium were demonstrated. It is well known that the chemical procedures by HF used on silicon or germanium resulted in the formation of hydrogen terminated surfaces.

Caution: HF is extremely dangerous and must be handled with great care. All work with HF must be done under a chemical fume hood all the time. Please, refer to hazards of HF in Material Safety Data Sheet (MSDS).

C.1. Wet-chemical etching and preparing of Si(111)-7x7

Wet chemical etching is normally used for defect delineation and oxide removal. The cleaning procedures pass through three steps. The first step is a general cleaning by using sulfuric acid and hydrogen peroxide to remove organic and inorganic contamination, and a strong rinse in DI water is required after this step. The second step is the passively-oxide removal. A dip in a diluted solution of HF and DI water is

sufficient to remove the native oxide layer; strong rinse in DI is also required. The third step is a rinse dry step; the sample is blown dry with Ar gas.

The Si(111) single crystal was cut to 5x4 mm^2 from ~ 400 μm thick wafer p-type with resistivity of 20-50 Ωcm. The miscut angle was 0.9° off (111). For the wet-chemical etching, do the following:

1. Cut Si wafer into 5mm x 4 mm using diamond cutter.
2. Clean the sample using modified Shiraki method as follows: immerse the sample in a solution of H_2SO_4 and H_2O_2 (4:1) for 10 minutes, rinsed with ultra pure water for 10 min, then dipped into a solution of 49% HF: H_2O = 1:10 for 1 minute. Repeat for another cycle. This treatment is known to remove native oxide and terminate the surface silicon dangling bonds with hydrogen.
3. Unused clean samples are stored under ethanol and are etched by HF just before being loaded into the chamber.
4. Load the sample inside the UHV chamber with the sample holder manipulator.
5. Apply a direct heating current and monitor the sample's temperature by using the thermocouple pressed between the sample surface and the sample holder.
6. During the back-out process, keep the sample temperature above 300 °C.
7. At UHV, flash the sample to a temperature of 1200 °C for 2 minutes.
8. Cool the sample slowly between 1000 °C and 800 °C to ensure a good and clear (7x7) reconstruction. You may repeat the flashing process until you get a clear pattern.
9. Calibrate and use Pt/PtRh(10%) thermocouple.

C.2. Cleaning and preparing Ge(111)-c(2x8)-(1x1)

Two methods of cleaning were used, wet-chemical etching and Ar^+ ion bombardment. Both methods are known to prepare the sample for epitaxy. The choice of method depends upon availability, applications, and simplicity; you may prefer one method over the other.

The Ge(111) single crystal was cut to 6x5 mm^2 from a 340 μm thick wafer n doped with antimony with resistivity of 1.4-2.2 Ωcm. The surface has a vicinal angle of 0.5^o off (111).

C.2.1. Ar^+ ion bombardment

1. Cut Ge wafer into 6mm x 5 mm using a diamond cutter.
2. Clean the examined sample with ethanol in ultrasonic cleaner for 10 minutes.
3. Load the sample inside the UHV chamber through the sample holder manipulator.
4. Apply a direct heating current and monitor the sample's temperature by using the thermocouple pressed between the sample surface and the sample holder.
5. During the back-out process, keep the sample temperature above 300 °C.
6. At UHV, prepare to use the Ar^+ ion gun, refer to appendix A.2.
7. Carefully open the Ar leak valve to leak in the Ar gas until the pressure reaches 10-5 torr.
8. Set the ion gauge emission to 5 mA and switch beam energy to 500 eV.
9. Allow 1-2 minutes for it to warm up.

10. Gradually increase the emission control to 20 mA. Keep the beam energy at 500 eV normal incidence. Allow a few hours before pumping up the system back to UHV.
11. Carefully start up the ion pump, wait until get UHV.
12. Anneal the sample at 700 °C for 20 minutes.

C.2.2. Wet-chemical etching of Ge(111)

In this step, the oxide removal from Ge(111) surface via HF solution is followed by vacuum annealing. The procedure described as follows:

1. Cut Ge wafer into 6mm x 5 mm using a diamond cutter.
2. Clean the sample as follows: immerse the sample in DI water for 30 seconds to dissolve the native oxide. Dip the sample into 10% of H_2O_2 for 30 seconds to grow a fresh chemical oxide. Then immerse into 49% HF: H_2O = 1:5, solution for 10 minutes. Repeat for another cycle. Finally, the sample is blown dry with Ar gas before loading it into the chamber. This treatment is known to remove native oxide and terminate the surface Ge dangling bonds with hydrogen.
3. Unused clean samples are stored under ethanol and are etched by HF just before being loaded into the chamber.
4. Load the sample into the UHV chamber with the sample holder manipulator.
5. Apply a direct heating current and monitor the sample's temperature by using the thermocouple pressed between the sample surface and the sample holder.
6. During the back-out process, keep the sample temperature above 300 °C.
7. At UHV, anneal the sample at 700 °C for 20 minutes.